Multiscale Simulation of Breaking Wave Impacts

Lindberg, Ole

Publication date:
2013

Document Version
Publisher's PDF, also known as Version of record

Multiscale Simulation of Breaking Wave Impacts

Ole Lindberg

TECHNICAL UNIVERSITY OF DENMARK
DEPARTMENT OF MECHANICAL ENGINEERING
SECTION FOR FLUID MECHANICS, COASTAL AND MARITIME ENGINEERING
MARCH 2012

Preface

This thesis is submitted as partial fulfillment for the degree of Doctor of Philosophy at the Technical University of Denmark (DTU), Lyngby, Denmark.

This work has been performed over the time period August 2008 to March 2012. The project was carried out at the Section of Coastal, Maritime and Structural Engineering (SKK) and Section for Fluid Mechanics, Coastal and Maritime Engineering (FCM) at the Department of Mechanical Engineering (MEK) in cooperation with the Department of Informatics and Mathematical Modelling (IMM). The study has been supervised by Harry B. Bingham (MEK), Jens Honore Walther (MEK) and Allan P. Engsig-Karup (IMM).

The project has been financed by Technical University of Denmark and the Statkraft Ocean Energy Research Program (SOERP).

Ole Lindberg

Lyngby, Denmark.
March 26, 2012.

Acknowledgements

I would like to thank Technical University of Denmark and the Statkraft Ocean Energy Research Program for financing this project.

I would like to thank my supervisors Harry B. Bingham, Jens Honore Walter and Allan Peter Engsig-Karup.

Thanks to Henrik Bredmose for sharing data and knowledge about breaking wave impacts.

A special thanks goes to my office colleagues Sopheak, Torben, Robert and Mostafa.

Abstract

The purpose of this project is to make an accurate, robust, geometric flexible and efficient model for calculation of forces on structures from nonlinear ocean waves and breaking wave impacts. Accurate prediction of the extreme forces on wind turbine foundations, breakwaters and tidal or wave power devises are important for enhancement structural designs.

The proposed model is based on an incompressible and inviscid flow approximation and the governing equations are applied in an arbitrary Lagrangian-Eulerian moving frame of reference (ALE). The Runge-Kutta method (RK) is used for time integration and mass conservation is satisfied through a pressure-corrector type calculation of the pressure. The weighted least squares method (WLS) is combined with approximate Riemann solvers to introduce numerical smoothing of the solution around steep gradients in the velocity and pressure fields. The Poisson equation is solved and the pressure boundary conditions are satisfied by a generalized finite pointset method (GFPM); This provides a geometrically flexible and stable solution for the fluid pressure. The numerical approximations of these equations are performed on unstructured point distributions and the solutions for velocity and pressure are represented by WLS approximation of multivariate polynomials. The stencils for the ALE-WLS and GFPM methods are found through a breadth first search (BFS) in a modified Delaunay graph. This graph is the discrete representation of the fluid domain and the connectivity between the calculation points. The graph is updated according to the evolving topology of the fluid domain caused by the fluid reaching or leaving a solid boundary or the free surface colliding with itself or another free-surface. After each time step the fluid domain is checked for any of these intersections and the topology is updated accordingly in its graph representation. The calculation points move in a Lagrangian way and this can cause ill-conditioning of the generalized Vandermonde matrix in the WLS and GFPM methods. To prevent this the point set is refined and coarsened by a fill-distance based adaptivity method and redistributed via a point position filtering method. The incompressible and inviscid ALE-WLS model is applied to the following standard validation test cases: deforming elliptical drop, small amplitude standing waves and the dam break problem. The deforming elliptical drop test show that the model can calculate the kinematics and dynamics of this free surface flow accurately and robustly. The small amplitude standing wave gives the same conclusions. Long time integration of this small amplitude periodic motion is possible due to accurate free surface evolution and small errors in the fluid volume. The dam break test case shows that the incompressible and inviscid ALE-WLS model can calculate nonlinear fluid motion, fluid structure impacts and overturning waves. The propagation speed of the wetting front and impact pressures are compared to experiments and the results compare reasonably well. The incompressible and inviscid ALE-WLS model is coupled with

the potential flow model of Engsig-Karup et al. [2009], to perform multiscale calculation of breaking wave impacts on a vertical breakwater. The potential flow model provides accurate calculation of the wave transformation from offshore to the vicinity of the breakwater. The wave breaking close to the breakwater and the wave impact are calculated by the incompressible ALE-WLS model. The forces calculated with the incompressible and inviscid ALE-WLS model are $\approx 1-2$ times the corresponding compressible calculations in Bredmose et al. [2009] for the calculations without trapped air.

Among the contributions of this project are the ALE-WLS method combined with approximate Riemann solvers and the generalization of the FPM method to arbitrary order of accuracy. The WLS and GFPM stencils found using the BFS data structure, which is updated due to topology changes of the evolving fluid domain. This extension combined with ALE-WLS and approximate Riemann solvers gives a numerical model capable of calculation of forces due to breaking wave impacts. The incompressible and inviscid ALE-WLS model has been coupled with a potential flow model to provide multiscale calculation of forces from breaking wave impacts on structures.

Resume

Formålet med dette projekt er at lave en nøjagtig, robust, geometrisk fleksibel og effektiv beregningsmodel til beregning af kræfter påstrukturer fra ikke-lineære brydende bølger. Et bedre estimat af tryk og laster påhavvindøller, tidevand - og bølgeenergi-anlæg kan bruges til forbedring af det strukturelle design.

En strømningsmodel uden kompressibilitet/sammentrykkelighed og viskositet med fri overflade er præsenteret, og de styrende ligninger er formuleret i et arbitrært Lagransk-Eulersk bevægeligt koordinatsystem (ALE). Runge-Kutta-metoden er anvendt til tidsintegration, og massebevarelse er tilfredsstillet med en prædiktion-korrektionsberegning af trykket. Weighted least squares metoden (WLS) er kombineret med approksimative Riemann-løsere for at udglatte løsningen tæt ved stejle gradienter i hastigheds- og trykfelterne. Poissons ligning er løst sammen med tryk-randbetingelser ved hjælp af en generaliseret finite-pointset metode (GFPM). Dette giver en geometrisk fleksibel- og stabil løsning af væsketrykket. Den numeriske approksimation af ligningerne er udført pået ustruktureret punktsæt, og løsningerne for hastigheder og tryk er repræsenteret med multivariable polynomier. De lokale punktsæt til anvendelse i WLS- og GFPM-metoderne er fundet ved hjælp af brede først søgning i en modifiseret Delaunay graf. Grafen er opdateret i forhold til udviklingen af væskedomænet. Efter hvert Runge-Kutta skridt bliver væskedomænet tjekket for ændringer i topologi, forårsaget af væskens interaktion med en struktur eller hvis en fri overflade interagerer med andre frie overflader. Væske domænets rande bliver opdateret i forhold til topologi ændringerne i væsken. Beregningspunkternes bevægelse er næsten Lagrangsk, og det forørsager en dårlig konditionering af den generaliserede Vandermonde matrix i WLS- og GFPM-metoderne. For at undgådette gøres punktsættet finere eller grovere med en afstand til en nabo baseret på adaptivitets-metode og gendistribution med en punkt position filtrerings metode.

ALE-WLS-modellen uden kompressibilitet/sammentrykkelighed og viskositet er anvendt påstandard tests: Deformation af en ellipseformet draa be, stående bålger med lille amplitude og dæmningsbrudv. Testen med deformation af en ellipseformet dråbe viser, at modellen er i stand til at beregne kinematikken og dynamikken af en strømning med fri overflade både nøjagtigt og robust. Testen med en bålgen med lille amplitude giver en lignende konklusion. En lang tidsintegration af bølger med lav amplitude er mulig, fordi bevægelsen af den fri overflade er beregnet nøjagtigt, og fordi fejlen i volumenberegningen er lille. Testen med dæmningsbrud viser, at modellen kan beregne ikke-lineære væskebevægelser, væske-struktur interaktion og brydende bølger. Udbredelseshastigheden af væskefronten og trykket påvæggen er sammenlignet med eksperimenter. Sammenligningen er rimelig god.

ALE-WLS-modellen uden kompressibilitet/sammentrykkelighed og viskositet er koblet med en potential strømningsmodel, Engsig-Karup et al. [2009], for at lave multiskala

beregning af brydene bœlger påen lodret mole. Potential strømningsmodellen giver en nøjagtig beregning af bølgeudbredelsen fra åbent hav til tæt påmolen. Bølgebrydningen tæt ved molen, og når bølgen rammer molen, er beregnet med ALE-WLS-modellen. De største bølgelaster påden lodrette mole er $\approx 1-2$ gange størrelsen af bølgelasterne beregnet ved hjælp af en kompressibel model, Bredmose et al. [2009].

De vigtigste dele af dette projekt er ALE-WLS-modellen kombineret med approksimative Riemann-løsere og generaliseringen af finite-pointset-metoden til højere ordens nøjagtighed. De lokale punkt sæt til WLS-og GFPM-beregningerne er fundet med en BFS-datastruktur, som opdateres under hensyntagen til topologiændringer i væskedomænet. Denne model giver mulighed for nøjagtig multiskala-beregning af laster fra ikke-lineære brydende bølger påkonstruktioner ved hjælp af koblingen med en potential strømnings model.

Contents

List of Symbols

Abbreviations

ALE	Arbitrary Lagrangian-Eulerian.
BEM	Boundary Element Method.
BFS	Breadth first search.
FEM	Finite Element Method.
FPM	Finite Pointset Method.
FV	Finite Volume Method.
GFPM	Generalized Finite Pointset Method.
RBFDQ	Radial Basis Function Differential Quadrature.
RK	Runge-Kutta.
SPH	Smoothed Particle Hydrodynamics.
TVD	Total Variation Diminishing.
VOF	Volume of Fluid Method.
WLS	Weighted Least Squares.

Greek Symbols

$\boldsymbol{\alpha}$	Matrix of Runge-Kutta coefficients or vector of indices.
$\boldsymbol{\beta}$	Matrix of Runge-Kutta coefficients.
η	Free surface elevation.
γ	Surface tension.
$\partial\Omega, \Gamma$	Boundary of the physical domain.
Γ_{fs}	Free surface boundary.
Γ_{wl}	Wall boundary.

μ	Dynamic viscosity.
∇	Gradient operator.
ν	Kinematic viscosity.
Ω	Physical domain.
Ω_h	Numerical approximation of the physical domain.
ϕ	Velocity potential or a scalar function.
ρ	Density.
τ	Time coordinate in the parameter space.
$\boldsymbol{\xi}$	Vector of Cartesian coordinates in the parameter space.
Ξ	Parameter space.

Roman Symbols

$\boldsymbol{a}_\alpha$	Vector of polynomial coefficients.
$\boldsymbol{b}$	Vector of accelerations from body forces.
c_s	Speed of sound.
$\boldsymbol{D}$	Deformation strain tensor.
d	Number of physical dimensions.
D^α	Differential operator.
Δt	Time step size.
$\boldsymbol{e}$	Orthogonal Cartesian basis.
E	Edge or error estimator.
$\boldsymbol{F}$	Flux tensor.
$\boldsymbol{f}$	Flux or forcing vector.
Fr	Froude number.
g	Gravitational acceleration, 9.81m/s.
$\boldsymbol{g}$	Vector of gravitational accelerations.
$\boldsymbol{I}$	Identity matrix.
J	Determinant of the Jacobian matrix.
J_h	Numerical approximation of the Jacobian.

$\mathcal{J}$	Jacobian matrix.
L	Length scale, wave length.
M	Mach number.
$\boldsymbol{n}$	Normal vector of the physical domain boundary.
N	Number of points.
n	Time step.
N_p	Number of terms in the polynomial basis.
$N_{\mathcal{S}}$	Number of points in stencil.
p	Pressure or order of polynomial basis.
p_0	Pressure on the free surface boundary.
$\mathcal{P}_\Gamma$	The set of points on the boundary of the physical domain.
$\mathcal{P}_{\Gamma_{fs}}$	The set of points on the free surface of the boundary.
$\mathcal{P}_{\Gamma_{wl}}$	The set of points on the wall boundary.
p_h	Numerical approximation of the pressure.
$\mathcal{P}_\Omega$	The set of points in the physical domain.
$\boldsymbol{q}$	Vector of unknowns.
Re	Reynolds number.
$\boldsymbol{S}$	Stress tensor.
$\mathcal{S}$	Stencil.
s	Number of Runge-Kutta stages.
$\boldsymbol{T}$	Viscous stress tensor.
$\mathcal{T}$	Triangular mesh.
T	Time scale, wave period or triangle.
t	Time.
$\boldsymbol{u}$	Fluid velocity vector.
U	Velocity scale.
$\boldsymbol{u}_0$	Frame of reference velocity vector.
$\boldsymbol{u}_h$	Numerical approximation of the velocity.

V	Flow velocity or volume.
We	Weber number.
$\boldsymbol{x}$	Vector of Cartesian coordinates in the physical space.
x, y, z	Cartesian coordinates.

Chapter 1

Introduction

The purpose of this project is to make an accurate, robust, geometric flexible and efficient numerical model for calculation of nonlinear forces from breaking ocean waves on structures in the marine environment. The model is intended for application in connection with design of offshore wind turbines, tidal and wave power extraction devices. Optimal structural designs require an accurate prediction of the maximum nonlinear wave forces to be expected over a working lifetime. The state of the art for prediction of forces on fixed near-shore structures such as wind turbines is to apply a Morison-type formula with wave kinematics from an accurate nonlinear potential flow model, Sumer and Fredsøe [1997]. Navier-Stokes solvers are sometimes used to obtain estimates of peak forces for violent episodes of short duration, Bredmose and Jacobsen [2010]. Despite these well established methods, the estimation of maximum forces on structures is still an area of intensive research and a great challenge for researchers and engineers, Peregrine [2003]. The focus of this project is accurate numerical calculation of nonlinear free surface flow, in particular breaking waves and breaking wave impacts.

The maximum wave forces occur when a steep and slightly overturning wave impacts on a structure and the actual wave impact phenomenon is very local both in time and space Sumer and Fredsøe [1997]. However a wave has traveled a relatively long distance before it impacts on a structure. Accurate simulation of wave impacts requires the waves to be propagated and evolved from the far field to the near field of a structure as demonstrated in Bredmose et al. [2009]. An accurate model for the propagation of smooth and non-overturning nonlinear ocean waves is presented in Bingham and Zhang [2007] and Engsig-Karup et al. [2009] and the present work can be viewed as an attempt to extend this model to handle overturning waves and wave impacts. The sketch in figure 1.1 shows the idea of smooth waves in the far field and overturning waves in the near field of a wind turbine.

An efficient nonlinear ocean wave model can be based on an accurate higher-order finite difference approximation of the free surface elevation, see Engsig-Karup et al. [2009] and Engsig-Karup et al. [2011], which is governed by the kinematic equation

$$\frac{\partial \eta}{\partial t} + \boldsymbol{u} \cdot \nabla \eta = \frac{d\eta}{dt} = w, \tag{1.1}$$

where $\eta = \eta(t, x, y) \in \mathbb{R}$ is the free surface elevation, $\boldsymbol{u} = \boldsymbol{u}(t, x, y)$ is the velocity vector and w is the vertical velocity. The vertical velocity is obtained via the Laplace equation

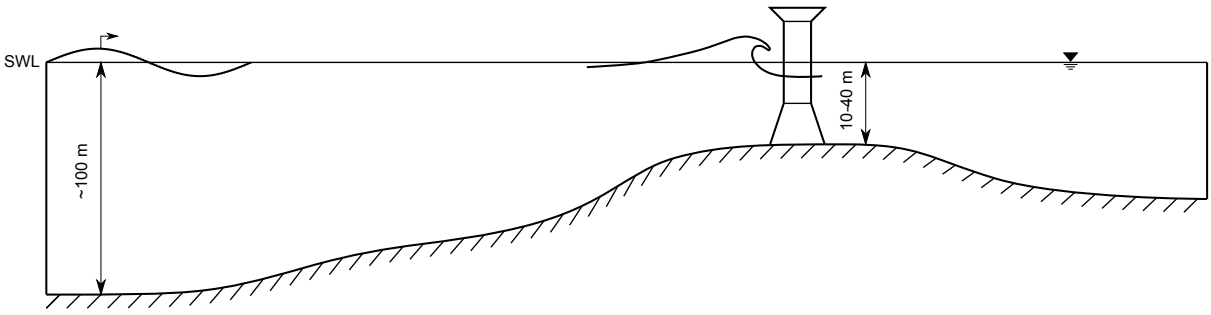

Figure 1.1: A sketch showing a smooth wave in the far field and an overturning wave in the near field of a windturbine foundation.

for the velocity potential $\phi = \phi(x, y, z) \in \mathbb{R}$. The horizontal and vertical velocities are accurately and effectively calculated on a curvilinear structured mesh fitted to the seabed and free surface via a transfinite interpolation. Another practical approximation is neglecting the air phase. With the physical domain restricted to the water volume, problematic steep gradients in the density, viscosity and/or volume fraction functions, complicated level-set functions and smoothing of the air-water interface are avoided, Ferziger and Peric [2002]. The equation for the free surface evolution (1.1) is Eulerian (fixed in space) in the horizontal direction and Lagrangian (moving with material velocity) in the vertical direction. The accuracy of the free surface evolution depends, among other things, on the Lagrangian movement in the vertical direction. The single valued description of the free surface limits the application of this model to non-overturning waves. The basic idea in this project is simulate overturning waves by a Lagrangian description of the free surface

$$\frac{d\boldsymbol{x}}{dt} = \boldsymbol{u}, \quad \boldsymbol{x} \in \Gamma_{fs}, \tag{1.2}$$

where Γ_{fs} is the free surface boundary of the water volume. The evolution of the free surface should be based on an accurate and robust calculation of the free surface velocity. The velocity of the free surface and the force calculation on the structures requires an accurate description of kinematics and the dynamics on both the free surface and close to the bodies.

A good starting point for the understanding of breaking wave impact on structures is the small chapter on forces resulting from breaking wave impact in Sumer and Fredsøe [1997]. They discuss two breaking wave impact cases: A vertical wall and a vertical cylinder, and give an introduction to the most prominent physical features of the breaking-wave impacts. The impingement of a wave on a wall gives an impulsive pressure at the location of the impact. As the wave impact progresses, the wall becomes exposed to a larger area with high pressure. The impact characteristics depend on the location of the wave breaking relative to the wall. A very steep and slightly overturning wave gives the largest impact forces. If the wave breaks too early or too late the forces will be smaller. The pressure is highest at the point where the overturning part of the wave hits wall. The typical maximum pressure $p_{\max}/(\rho c^2)$, $c = L/T$ is in the range $3 - 10$ and the duration of the impulsive pressure increase (the rise time) is in the range

$0.0005T - 0.002T$ where L is wave length and T is wave period. The uncertainties of these measures are very high, because it is difficult to reproduce breaking wave impacts in experiments. These uncertainties are related to the presence of air, either in the form of tiny air droplets or as pockets of trapped air between the overturning wave and the structure. The above mentioned chapter also gives an overview of the experiments related to breaking-wave impact conducted from late 1970's to late 1980's, with the latest and most important being Chan and Melville [1988]. They describe breaking waves as an strongly nonlinear transient two-phase turbulent process, which is not amenable to rigorous theoretical or numerical treatment and the prediction of breaking-wave forces dependent on the availability of reliable experimental data. But the same difficulties that make the problem theoretically intractable also makes it difficult to conduct well-controlled repeatable experiments. These statements have been challenged by investigations of violent breaking-wave impacts both experimentally and numerically by Bullock et al. [2007] and Bredmose et al. [2009]. The experiments confirm that the wave conditions, the so called flip through impact, entrained air and/or trapped air are very important characteristics of violent breaking wave impacts. In the numerical studies, with a compressible model, all the main characteristics of breaking wave impact are reproduced. The flip through type impact is further investigated by Lugni et al. [2006] and Bredmose et al. [2010]. The later paper investigate an ideal flip-through breaking-wave impact: An impact where no air is entrained nor trapped. They compare an irrotational, incompressible and inviscid model with experiments and find that model reproduces the main features of the ideal flip-through impact. A simple pressure-impulse model is presented in the review paper on water-wave impacts on vertical walls Peregrine [2003]. This model can provide insight into the basic features of the breaking-wave impact.

The numerical approximation of free surface flow is an active area of research and it is challenging due to the presence of air-water interfaces in two phase models or moving free surface boundaries in single phase models. The potential flow models with nonlinear free surface boundary conditions can be approximated using conformal mappings and boundary element method, Bredmose et al. [2009], Bredmose et al. [2010], to calculations of over-turning waves and wave impacts. Breaking waves and breaking wave impacts has been more accurately calculated by an inviscid and compressible model with the numerical approximations based on finite volume, VOF and exact, Riemann solvers Bredmose et al. [2009]. The particle finite element method (PFEM), Idelsohn et al. [2004], is a free surface flow model based on Lagrangian particles, finite element (linear solution representation and weighting function) and alpha-shape representation of the free surface. Another method used for approximation of free surface flow and based on Lagrangian particles is the smoothed particle hydrodynamics method (SPH). The SPH method has been improved with the introduction of approximate Riemann solvers, Vila [1999], and later its combination with the advective upwind splitting method, Ferrari et al. [2009]. The SPH method has been applied to marine hydrodynamics relevant problems like dam break and breaking wave impacts by Dalrymple and Rogers [2006], Colagrossi and Landrini [2003] and Antuono et al. [2011]. A very important contribution in the area of free surface flow is the introduction of the marker and cell method Harlow and Welch [1965]. This is a method for free surface tracking which is often applied when solving the Navier-Stokes equations. In the original form it is combined with explicit first order time integration and second order finite difference approximation. A method for free surface tracking in

a two-phase flows is the finite volume based volume of fluid (VOF) method Hirt and Nichols [1981]. The method is today a standard in many academic and industrial codes. A state-of-art VOF model have been used to calculate green water on deck by Nielsen and Mayer [2004]. A more resent application to breaking wave forces on windturbine foundations is Bredmose and Jacobsen [2010] where comparison with Morison formula is also given. The level set method, Sussman et al. [1994], is similar the VOF method and also used for simulation of two-phase flow. But where the free surface is tracked by a discontinuous volume fraction function in VOF, the free surface is tracked by a signed distance function in the level set method. The space-time finite volume method has been applied to calculation of plunging wave-breaking in deep water in two spatial dimensions by Zwart et al. [1999]. The air phase is neglected and the solution domain is evolved using Lagrangian points in a triangular mesh. The method is applied to overturning wave calculation, but stopped just before the overturning wave front impinges the free surface.

In this project, the air phase is neglected and the fluid domain is restricted to the water-phase as in Engsig-Karup et al. [2009]. The isothermal, incompressible and inviscid equations are solved in an arbitrary Lagrangian-Eulerian frame of reference (ALE), Donea et al. [1982], to facilitate the Riemann solution between collocation points, Ferrari et al. [2009], Shu et al. [2004]. The divergence of the flux is calculated using a weighted least squares (WLS) method based on interaction with the neighboring calculation points. The Poisson equation for the pressure is solved using a generalization of the finite pointset method (FPM) Tiwari and Kuhnert [2007].

In chapter 2 the governing equations for fluid motion are presented and the isothermal, incompressible and inviscid flow approximation is justified. In chapter 3, a numerical methods for solution of the governing equations using the WLS and a generalization of the finite pointset method (GFPM) is proposed. The combination of the weighted least squares method with approximate Riemann solvers are presented in chapter 4. Chapter 5 describes the singularity at the wet-dry contract points and how it can be removed by relaxation of the dynamic free surface boundary condition. The fluid domain approximation, its representation and data structures are described in chapter 6, together with the breadth first search (BFS) which is used to find stencils for the WLS and GFPM calculations. Model validation and application examples are given in chapter 7. These are deforming liquid drop, small amplitude standing waves and dam break. A one-way coupling of the presented model with a potential flow model, Engsig-Karup et al. [2009], is presented in chapter 9 together with an application to breaking wave impacts on a vertical break water. A more efficient Lagrangian model based on a time independent parameter space is proposed in chapter 10.

Chapter 2

Governing Equation for Fluid Motion

The governing equations of isothermal fluid motion with a free surface are the equations for conservation of mass and momentum, with the physical boundary conditions imposed by the free surfaces and walls. The equations are presented in an ALE form Donea et al. [1982]. This choice is motivated by Ferrari et al. [2009], where the nonlinear flux of mass and momentum are split into the physical flux and the flux related to the movement of the frame of reference. The conservation laws have nonlinear hyperbolic terms and the solutions for pressure and velocity can have steep gradients, either due to the initial conditions or the non-linearity of the equations, Toro [1999]. Around these steep gradients polynomial approximations can develop spurious oscillations. The ALE formulation enables a numerical approximation where the spurious oscillations can be avoided: If the multi-dimensional problem is transformed into uni-directional plane wave problems the physical flux can be obtained via a solution to the Riemann problem, Toro [1999]. This introduces intrinsic numerical viscosity, which can smooth the solution and prevent spurious oscillations from appearing.

The target application is free surface flow, specifically breaking water waves. The air phase is neglected based on the ratio $\rho_{air}/\rho_{water} \approx 10^{-3}$ and on the experience with water phase calculations of nonlinear water waves, Engsig-Karup et al. [2009]. Hence the physical domain $\Omega(t)$ is the water phase and it evolves in time due to the motion of the free surface Γ_{fs}.

Time Dependent Transformations

In the ALE method the governing equations are based on time-dependent coordinate transforms. The time dependent transform is expressed as a vector-valued time-dependent function, as in e.g. Liseikin [1999],

$$\boldsymbol{x}(t, \boldsymbol{\xi}) : \ \Xi \to \Omega, \quad \boldsymbol{\xi} = (\xi_1, \ldots, \xi_d), \quad \boldsymbol{x} = (x_1, \ldots, x_d). \tag{2.1}$$

where $\boldsymbol{\xi} \in \Xi$ is the reference domain and $\boldsymbol{x} \in \Omega$ is the physical domain. This is a smooth invertible coordinate transformation of the physical domain $\Omega(t) \subset \mathbb{R}^d$ from the parametric domain $\Xi \subset \mathbb{R}^d$, where $\mathbb{R}^d$ presents the Euclidean space with the Cartesian basis spanned by the orthogonal system of vectors $\boldsymbol{e}_1, \ldots, \boldsymbol{e}_d$. In this basis the positions

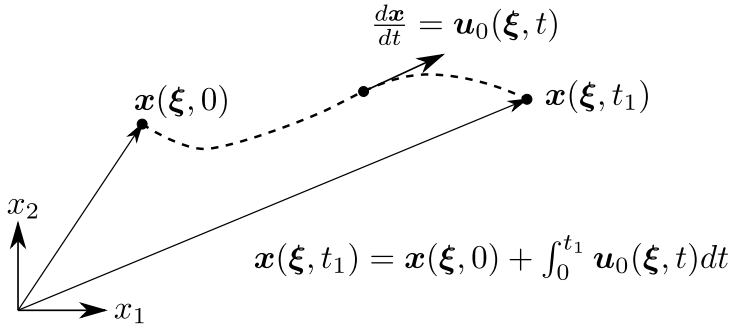

Figure 2.1: The path and velocity of a point in the physical domain $\boldsymbol{x}(\boldsymbol{\xi}, t) \in \Omega$ at a fixed position in the parametric reference domain $\boldsymbol{\xi} \in \Xi$.

in the physical and the parametric domains are

$$\boldsymbol{x} = x_1\boldsymbol{e}_1 + \cdots + x_d\boldsymbol{e}_d, \tag{2.2}$$
$$\boldsymbol{\xi} = \xi_1\boldsymbol{e}_1 + \cdots + \xi_d\boldsymbol{e}_d. \tag{2.3}$$

A point with at a fixed position in Ξ moves with the velocity $\boldsymbol{u}_0 = \boldsymbol{u}_0(\tau, \boldsymbol{\xi}) \in \mathbb{R}^d$ in the physical domain Ω. The path of a point with is seen in figure 2.1.

The relation between changes in the coordinates is expressed by the Jacobian matrix

$$\mathcal{J} = \left(\frac{\partial x_i}{\partial \xi_j}\right), \quad i, j = 1, \ldots, d, \tag{2.4}$$

and the Jacobian, which is the determinant of this matrix,

$$J = \det\left(\frac{\partial x_i}{\partial \xi_j}\right), \quad i, j = 1, \ldots, d. \tag{2.5}$$

To avoid confusion between temporal derivatives in the physical domain and the moving parametric domain, the time coordinate τ is associated to the moving parametric domain and time coordinate t is designated to the physical domain Ω.

The basic identity of the coordinate transformation, Liseikin [1999], gives the equation for the temporal evolution of the Jacobian in the parametric coordinates

$$\frac{\partial J}{\partial \tau} = J\nabla \cdot \boldsymbol{u}_0, \tag{2.6}$$

where $\boldsymbol{u}_0 = \frac{\partial \boldsymbol{x}}{\partial \tau}$ is the velocity of the moving parametric coordinates and τ is the time coordinate in the parametric coordinates. This is used to relate the time derivative in the fixed physical coordinate of a scalar function $f(t, \boldsymbol{x}) \in \mathbb{R}$ with the time derivative in the moving parametric coordinate

$$\frac{\partial f}{\partial t} = \frac{1}{J}\frac{\partial}{\partial \tau}(Jf) - \nabla \cdot (f\boldsymbol{u}_0). \tag{2.7}$$

This relation is used to transform the conservation laws of mass and momentum to the moving frame of reference.

2.1 Conservation of Mass

The differential form of the equation for mass conservation in a fixed frame of reference is, Ferziger and Peric [2002],

$$\frac{\partial \rho}{\partial t} + \nabla \cdot (\rho \boldsymbol{u}) = 0, \tag{2.8}$$

where $\rho = \rho(t, \boldsymbol{x}) \in \mathbb{R} \geq 0$ is the density of the fluid. This equation is transformed to a moving frame of reference using (2.7)

$$\frac{\partial}{\partial \tau}(J\rho) + J\nabla \cdot (\rho(\boldsymbol{u} - \boldsymbol{u}_0)) = 0. \tag{2.9}$$

For an incompressible fluid ($\rho = \text{const.}$) the equation for conservation of mass reduces to

$$\nabla \cdot \boldsymbol{u} = 0, \tag{2.10}$$

which applies to both the fixed and moving frame of reference.

2.2 Conservation of Momentum

The differential form of the equation for conservation of momentum in a fixed frame of reference is, Ferziger and Peric [2002],,

$$\frac{\partial}{\partial t}(\rho \boldsymbol{u}) + \nabla \cdot (\rho \boldsymbol{u}\boldsymbol{u}^T) = \nabla \cdot \boldsymbol{S} + \rho \boldsymbol{b}. \tag{2.11}$$

where $\boldsymbol{b}$ is the acceleration due to body forces (e.g. the gravitational force) and $\boldsymbol{S} \in \mathbb{R}^d \times \mathbb{R}^d$ is the stress tensor

$$\boldsymbol{S} = -p\boldsymbol{I} + \boldsymbol{T}, \tag{2.12}$$

where $p \in \mathbb{R}$ is the pressure, $\boldsymbol{I}$ is the identity matrix and the viscous stress tensor is

$$\boldsymbol{T} = 2\mu \boldsymbol{D} - \frac{2}{3}\mu(\nabla \cdot \boldsymbol{u})\boldsymbol{I}, \tag{2.13}$$

in which the deformation strain tensor is

$$\boldsymbol{D} = \frac{1}{2}(\nabla \boldsymbol{u} + (\nabla \boldsymbol{u})^T). \tag{2.14}$$

The momentum equation is transformed into a moving frame of reference using (2.7)

$$\frac{\partial}{\partial \tau}(J\rho \boldsymbol{u}) + J\nabla \cdot (\rho \boldsymbol{u}(\boldsymbol{u} - \boldsymbol{u}_0)^T) = J(\nabla \cdot \boldsymbol{S} + \rho \boldsymbol{b}), \tag{2.15}$$

in which the rate of change momentum is along a path given by the velocity $\boldsymbol{u}_0$ of the moving frame of reference. For an incompressible fluid ($\rho = \text{const.}$) the equation for conservation of momentum in a moving frame of reference is

$$\frac{\partial}{\partial \tau}(J\boldsymbol{u}) + J\nabla \cdot \left(\boldsymbol{u}(\boldsymbol{u} - \boldsymbol{u}_0)^T\right) = J\left(\frac{1}{\rho}\nabla p + \nu \nabla^2 \boldsymbol{u} + \boldsymbol{b}\right). \tag{2.16}$$

2.3 Isothermal, Incompressible and Inviscid Fluid Approximation

Free surface flow is characterized by the Reynold number Re, the Mach number M, the Froude number Fr, the Weber number We and the relative density between the fluids under consideration:

$$Re = \frac{UL}{\nu}, \quad M = \frac{U}{c_s}, \quad Fr = \frac{U}{\sqrt{Lg}}, \quad We = \frac{\gamma}{\rho L U^2}, \tag{2.17}$$

where L is the length scale and U is the velocity scale of the flow, c_s is the speed of sound in the fluid, g is the gravitational acceleration and γ is the surface tension.

For marine applications the Reynolds number is often extremely large $\approx Re > 10^6$, hence the viscous effects are very small. In most cases the propagation speed of sound waves is much higher than the flow speed, the Mach number is therefore small $M \ll 1$ and compressible effects are negligible. When a wave becomes overturning and breaking the fluid in the upper part of the wave becomes a mixture between water and air. In this mixed medium the speed of sound can become surprisingly small, Bredmose et al. [2009], and the propagation of pressure waves resulting from wave impacts on structures can be important for accurate prediction of the maximum pressure, force and impulse. In the context of oceanographic free surface flow the inertia forces and the gravitational forces are of comparable magnitude, hence the Froude number is $Fr \approx 1$. Compared to the inertia forces the surface tension forces are small for ocean waves and when compared to the bulk motion of a typical wave structure impact in marine engineering. Hence the Weber number is large $We \gg 1$.

In summary the important dimensionless numbers in the dynamics of ocean waves and wave structure impacts are presented in table 2.1. The mathematical model is simplified due to these dimensional considerations by assuming

- Viscous effects: Negligible.
- Compressible effects: Negligible for ocean waves, but important for some types of wave structure impacts.
- Gravitational forces: Very important.
- Surface tension effects: Negligible.
- Relative density difference: For a water-air interface the relative density is $\approx 10^3$, which is assumed large enough to neglect the air phase. For some types of breaking waves and wave impacts the air entrainment and entrapment are important, Chan and Melville [1988], Bredmose et al. [2009], but these effects will not be considered.

The resultant fluid approximation is isothermal, incompressible and inviscid and the governing equations are conservation of space (2.6), mass (2.10) and momentum (2.16)

	Re	M	Fr	We
Ocean wave	$\gg 1$	$\ll 1$	≈ 1	$\gg 1$
Wave impacts	$\gg 1$	≈ 1	≈ 1	$\gg 1$

Table 2.1: The most important dimensionless numbers in ocean wave fluid dynamics and wave structure impacts.

which, in a frame of reference moving with velocity $\boldsymbol{u}_0$, are

$$\frac{d\boldsymbol{x}}{dt} = \boldsymbol{u}_0, \tag{2.18}$$

$$\frac{\partial J}{\partial t} = J\nabla \cdot \boldsymbol{u}_0, \tag{2.19}$$

$$\nabla \cdot \boldsymbol{u} = 0, \tag{2.20}$$

$$\frac{\partial}{\partial t}(J\boldsymbol{u}) + J\nabla \cdot \left(\boldsymbol{u}(\boldsymbol{u} - \boldsymbol{u}_0)^T\right) = J\left(\frac{1}{\rho}\nabla p + \boldsymbol{g}\right). \tag{2.21}$$

Note that the time coordinate in the moving frame of reference has been set to $\tau = t$ in the equations above. The fluid is subject to the physical boundary conditions of a frictionless, impermeable and stationary wall and a free surface without surface tension. The mass conservation over the free surface is expressed by a kinematic free surface condition

$$\boldsymbol{n} \cdot (\boldsymbol{u} - \boldsymbol{u}_0) = 0, \quad \boldsymbol{x} \in \Gamma_{fs}, \tag{2.22}$$

where $\boldsymbol{n}$ is the outward normal vector of the free surface, $\boldsymbol{u}_0$ is the velocity of the free surface and $\Gamma_{fs} \subset \partial\Omega$ is the free surface part of the fluid domain boundary. The force balance at the free surface of an incompressible fluid is expressed by a dynamic boundary condition

$$p = p_0, \quad \boldsymbol{x} \in \Gamma_{fs}, \tag{2.23}$$

where p_0 is the constant pressure at the free surface. The boundary condition for the frictionless, impermeable and stationary wall is

$$\boldsymbol{n} \cdot \boldsymbol{u} = 0, \quad \boldsymbol{x} \in \Gamma_{wl}, \tag{2.24}$$

where $\boldsymbol{n}$ is the outward normal to the wall and $\Gamma_{wl} \subset \partial\Omega$ is the wall part of the fluid domain boundary.

Chapter 3

Time Integration and Mass Conservation

The numerical approximation of the governing equations is based on the method of lines, hence the temporal and spatial terms are treated separately. The temporal approximation is presented in this chapter along with the approximation of mass conservation. A classical Runge-Kutta method is used for the approximation of the temporal terms and it is coupled to the mass conservation through a pressure-corrector type method.

3.1 Runge-Kutta Methods for Time Integration

The governing equations are viewed as a system of ordinary differential equations and for the purpose of Runge-Kutta integration they are rearranged in the form

$$\frac{d\boldsymbol{x}}{dt} = \boldsymbol{u}_0, \tag{3.1}$$

$$\frac{\partial J}{\partial t} = J\nabla \cdot \boldsymbol{u}_0 \tag{3.2}$$

$$\frac{\partial (J\boldsymbol{u})}{\partial t} = J\left(\nabla \cdot \left(-\boldsymbol{u}(\boldsymbol{u}-\boldsymbol{u}_0)^T - \frac{1}{\rho}\mathbf{I}p\right) + \boldsymbol{g}\right). \tag{3.3}$$

This system of ODE's can be written in compact form as

$$\frac{d\boldsymbol{q}}{dt} = \boldsymbol{f}(t,\boldsymbol{q}), \tag{3.4}$$

$$\boldsymbol{q} = \begin{bmatrix} \boldsymbol{x} \\ J \\ J\boldsymbol{u} \end{bmatrix}, \quad \boldsymbol{f}(t,\boldsymbol{q}) = \begin{bmatrix} \boldsymbol{u}_0 \\ J\nabla\cdot\boldsymbol{u}_0 \\ J(\nabla\cdot(-\boldsymbol{u}(\boldsymbol{u}-\boldsymbol{u}_0)^T - \frac{1}{\rho}\mathbf{I}p) + \boldsymbol{g}) \end{bmatrix}. \tag{3.5}$$

The s-stage Runge-Kutta method for time-integration of (3.4) has the general form

$$\begin{aligned} \boldsymbol{q}^{(0)} &= \boldsymbol{q}^n, \\ \boldsymbol{q}^{(k)} &= \sum_{l=1}^{k} \left(\alpha_{kl}\boldsymbol{q}^{(l-1)} + \beta_{kl}\Delta t \boldsymbol{f}(\boldsymbol{q}^{(l-1)}, t^n + \gamma_l \Delta t)\right), \quad k = 1,\ldots,s, \\ \boldsymbol{q}^{n+1} &= \boldsymbol{q}^{(s)}, \end{aligned} \tag{3.6}$$

where $\boldsymbol{q}^n$ solution at time step n, $\boldsymbol{q}^{(k)}$ is the solution at Runge-Kutta stage k, $\alpha_{kl},\ \beta_{kl},\ k,l = 1,\ldots,r$, are the coefficients defining the Runge-Kutta method, Δt is the time step and $t^{(k)}$ the time of the Runge-Kutta stage k. This form is presented in Shu and Osher [1988], where the coefficients for the total variation diminishing explicit 3-stage 3rd order method (TVDRK3) are

$$\boldsymbol{\alpha} = \begin{bmatrix} 1 & 0 & 0 \\ 3/4 & 1/4 & 0 \\ 1/3 & 0 & 2/3 \end{bmatrix}, \quad \boldsymbol{\beta} = \begin{bmatrix} 1 & 0 & 0 \\ 0 & 1/4 & 0 \\ 0 & 0 & 2/3 \end{bmatrix}. \tag{3.7}$$

and the classical explicit 4-stage 4th order method (RK4) has the coefficients

$$\boldsymbol{\alpha} = \begin{bmatrix} 1 & 0 & 0 & 0 \\ 1 & 0 & 0 & 0 \\ 1 & 0 & 0 & 0 \\ 1 & 0 & 0 & 0 \end{bmatrix}, \quad \boldsymbol{\beta} = \begin{bmatrix} 1/2 & 0 & 0 & 0 \\ 0 & 1/2 & 0 & 0 \\ 0 & 0 & 1 & 0 \\ 1/6 & 2/6 & 2/6 & 1/6 \end{bmatrix}. \tag{3.8}$$

The equation for conservation of mass (2.10) has to be satisfied at each new time step t^{n+1}. This is achieved by calculation of the pressure at each stage $p^{(k)}$ such that the velocity at the new stage $\boldsymbol{u}^{(k+1)}$ is divergence free. This procedure is explained in the next section.

3.2 Enforcing Mass Conservation

The velocity at the new stage $\boldsymbol{u}^{(k)}$ must satisfy the equation for mass conservation (2.10). The Jacobian and the momentum at the stage k are

$$J^{(k)} = \sum_{l=1}^{k} \Big(\alpha_{kl} J^{(l-1)} + \beta_{kl} \Delta t \boldsymbol{f}_2(\boldsymbol{q}^{(l-1)}) \Big), \tag{3.9}$$

$$(J\boldsymbol{u})^{(k)} = \sum_{l=1}^{k} \Big(\alpha_{kl} (J\boldsymbol{u})^{(l-1)} + \beta_{kl} \Delta t \boldsymbol{f}_3(\boldsymbol{q}^{(l-1)}) \Big), \tag{3.10}$$
$$k = 1,\ldots,s,$$

and the divergence of the momentum equation gives

$$\nabla \cdot (J\boldsymbol{u})^{(k)} = \nabla \cdot \sum_{l=1}^{k} \Big(\alpha_{kl} (J\boldsymbol{u})^{(l-1)} + \beta_{kl} \Delta t \boldsymbol{f}_3(\boldsymbol{q}^{(l-1)}) \Big), \quad k = 1,\ldots,s. \tag{3.11}$$

The product rule is applied to the left hand side and the divergence of the velocity is eliminated by the equation for conservation of mass

$$\boldsymbol{u}^{(k)} \cdot \nabla J^{(k)} = \nabla \cdot \sum_{l=1}^{k} \Big(\alpha_{kl} (J\boldsymbol{u})^{(l-1)} + \beta_{kl} \Delta t \boldsymbol{f}_3(\boldsymbol{q}^{(l-1)}) \Big), \tag{3.12}$$

and the right hand side for the stage $k-1$ is split in

$$\boldsymbol{f}_3(t, \boldsymbol{q}^{(k-1)}) = \boldsymbol{f}_3^*(t, \boldsymbol{q}^{(k-1)}) - \frac{J^{(k-1)}}{\rho} \nabla p^{(k-1)}, \tag{3.13}$$

where the non-pressure related terms are included in the intermediate right hand side

$$\boldsymbol{f}_3^*(t,\boldsymbol{q}^{(k-1)}) = J^{(k-1)}(\nabla\cdot(-\boldsymbol{u}^{(k-1)}(\boldsymbol{u}^{(k-1)}-\boldsymbol{u}_0^{(k-1)})^T)+\boldsymbol{g}), \tag{3.14}$$

and inserted

$$\begin{aligned}\nabla\cdot(J^{(k-1)}\nabla p^{(k-1)}) = \frac{\rho}{\beta_{kk}\Delta t}\Big(\nabla\cdot\Big(\sum_{l=1}^{k-1}\Big(\alpha_{kl}(J\boldsymbol{u})^{(l-1)}+\beta_{kl}\Delta t\boldsymbol{f}_3(\boldsymbol{q}^{(l-1)})\Big)\\ +\alpha_{kk}(J\boldsymbol{u})^{(k-1)}+\beta_{kk}\Delta t\boldsymbol{f}_3^*(t,\boldsymbol{q}^{(k-1)})\Big)\\ -\boldsymbol{u}^{(k)}\cdot\nabla J^{(k)}\Big),\quad k=1,\ldots,s..\end{aligned} \tag{3.15}$$

To simplify the notation the following intermediate velocity is introduced

$$\begin{aligned}(J\boldsymbol{u})^{(k)*} = \sum_{l=1}^{k-1}\Big(\alpha_{kl}(J\boldsymbol{u})^{(l-1)}+\beta_{kl}\Delta t\boldsymbol{f}_3(\boldsymbol{q}^{(l-1)})\Big)\\ +\alpha_{kk}(J\boldsymbol{u})^{(k-1)}+\beta_{kk}\Delta t\boldsymbol{f}_3^*(t,\boldsymbol{q}^{(k-1)}),\\ k=1,\ldots,s,\end{aligned} \tag{3.16}$$

and (3.15) reduces to

$$\nabla\cdot(J^{(k-1)}\nabla p^{(k-1)}) = \frac{\rho}{\beta_{kk}\Delta t}\Big(\nabla\cdot(J\boldsymbol{u})^{(k)*}-\boldsymbol{u}^{(k)}\cdot\nabla J^{(k)}\Big),\quad k=1,\ldots,s. \tag{3.17}$$

The equation above is an anisotropic pressure equation (similar to the anisotropic heat equation) and it is nonlinear due to the implicit velocity $\boldsymbol{u}^{(k)}$ on the right hand side. Making a stable numerical approximation for the anisotropic pressure equation $\nabla\cdot(J^{(k-1)}\nabla p^{(k-1)})$ is not trivial task. At least not with a point based solution and satisfaction of equations like the WLS method. Instead the derivation of the pressure equation is repeated, but now the momentum equation is divided by the Jacobian $J^{(k-1)}$ from the previous stage

$$\frac{(J\boldsymbol{u})^{(k)}}{J^{(k-1)}} = \frac{1}{J^{(k-1)}}\sum_{l=1}^{k}\Big(\alpha_{kl}(J\boldsymbol{u})^{(l-1)}+\beta_{kl}\Delta t\boldsymbol{f}_3(\boldsymbol{q}^{(l-1)})\Big), \tag{3.18}$$

and the divergence is applied to both sides of this equation

$$\nabla\cdot\left(\frac{(J\boldsymbol{u})^{(k)}}{J^{(k-1)}}\right) = \nabla\cdot\left(\frac{1}{J^{(k-1)}}\sum_{l=1}^{k}\Big(\alpha_{kl}(J\boldsymbol{u})^{(l-1)}+\beta_{kl}\Delta t\boldsymbol{f}_3(\boldsymbol{q}^{(l-1)})\Big)\right). \tag{3.19}$$

Now the product rule is applied to the left hand side and divergence of the velocity is eliminated by the equation for conservation of mass

$$\boldsymbol{u}^{(k)}\nabla\cdot\left(\frac{J^{(k)}}{J^{(k-1)}}\right) = \nabla\cdot\left(\frac{1}{J^{(k-1)}}\sum_{l=1}^{k}\Big(\alpha_{kl}(J\boldsymbol{u})^{(l-1)}+\beta_{kl}\Delta t\boldsymbol{f}_3(\boldsymbol{q}^{(l-1)})\Big)\right), \tag{3.20}$$

and the right hand side for the stage $k-1$ is split, as in the previous derivation of the pressure equation, (3.13) and the intermediate velocity (3.16) is used again. The resultant equation for the pressure is

$$\nabla\cdot\nabla p^{(k-1)} = \frac{\rho}{\beta_{kk}\Delta t}\Big(\nabla\cdot\Big(\frac{(J\boldsymbol{u})^{(k)*}}{J^{(k-1)}}\Big)\Big)-\boldsymbol{u}^{(k)}\cdot\nabla\Big(\frac{J^{(k)}}{J^{(k-1)}}\Big)\Big),\quad k=1,\ldots,s. \tag{3.21}$$

The equation for the pressure is approximated by the Poisson equation at the expense of exact mass conservation

$$\nabla^2 p^{(k-1)} = \frac{\rho}{\beta_{kk}\Delta t}\Big(\nabla\cdot\Big(\frac{(J\boldsymbol{u})^{(k)*}}{J^{(k-1)}}\Big)\Big) - \boldsymbol{u}^{(k)}\cdot\nabla\Big(\frac{J^{(k)}}{J^{(k-1)}}\Big)\Big). \quad k=1,\ldots,s. \tag{3.22}$$

This equation is nonlinear due to the presence of the implicit velocity $\boldsymbol{u}^{(k)}$ on the right hand side. If the rate of change of the Jacobian is small, i.e. the transport velocity is almost divergence free, then the nonlinear implicit term is small and can be neglected

$$\nabla^2 p^{(k-1)} = \frac{\rho}{\beta_{kk}\Delta t}\nabla\cdot\Big(\frac{(J\boldsymbol{u})^{(k)*}}{J^{(k-1)}}\Big), \quad k=1,\ldots,s. \tag{3.23}$$

This equation is linear and simple to approximate numerically. The exact conservation is sacrificed, but stability and ease of approximation are gained as seen chapter 4.

To complete the numerical solution approximation, we need an approximation of the gradient of the pressure ∇p and the divergence $\nabla\cdot\boldsymbol{u}_h^{(m)*}$ and the left hand side of the Poisson equation $\nabla^2 p^{(m-1)}$. The gradient and divergence are approximated using the WLS method and the Laplace operator in the Poisson equation is approximated using a generalization of the FPM method by Tiwari and Kuhnert [2007]. These methods are described in the following chapters 4 and 5.

3.3 The Pressure Boundary Conditions

The two physical boundary conditions for the Poisson equation are the constant or zero pressure on the free surface

$$p = 0, \quad \boldsymbol{x}\in\Gamma_{fs}, \tag{3.24}$$

and the no-flux boundary condition on the solid walls

$$\boldsymbol{u}\cdot\boldsymbol{n} = 0, \quad \boldsymbol{x}\in\Gamma_{wl}. \tag{3.25}$$

The no-flux boundary condition is coupled to the pressure by taking the inner product between the normal to the wall and the momentum equation (3.10)

$$\begin{aligned}
\boldsymbol{n}\cdot(J\boldsymbol{u})^{(k)} &= \boldsymbol{n}\cdot\sum_{l=1}^{k}\Big(\alpha_{kl}(J\boldsymbol{u})^{(l-1)} + \beta_{kl}\Delta t\boldsymbol{f}_3(\boldsymbol{q}^{(l-1)})\Big),\\
&= \boldsymbol{n}\cdot\Big(\sum_{l=1}^{k-1}(\alpha_{kl}(J\boldsymbol{u})^{(l-1)} + \beta_{kl}\Delta t\boldsymbol{f}_3(\boldsymbol{q}^{(l-1)}))\\
&\quad +\alpha_{kk}(J\boldsymbol{u})^{(k-1)} + \beta_{kk}\Delta t(\boldsymbol{f}_3^*(t,\boldsymbol{q}^{(k-1)})\\
&\quad -\frac{J^{(k-1)}}{\rho}\nabla p^{(k-1)})\Big)\\
&= \boldsymbol{n}\cdot\Big((J\boldsymbol{u})^{(k)*} - \frac{J^{(k-1)}\beta_{kk}\Delta t}{\rho}\nabla p^{(k-1)}\Big)\\
&= 0 \quad k=1,\ldots,s,
\end{aligned} \tag{3.26}$$

which results in an inhomogeneous Neumann boundary condition for the pressure in the direction of the normal vector to the wall

$$\boldsymbol{n} \cdot \nabla p^{(k-1)} = \frac{\rho}{J^{(k-1)} \beta_{kk} \Delta t} \boldsymbol{n} \cdot (J\boldsymbol{u})^{(k)*}, \quad k = 1, \ldots, s. \tag{3.27}$$

Note that the derivation of the pressure wall boundary condition resembles the derivation of the Poisson equation for the pressure. The Poisson equation with the above described boundary conditions is to be approximated and solved in each Runge-Kutta stage.

3.4 Summary

The temporal terms of the incompressible and inviscid ALE equations in a moving frame of reference have been approximated numerically by the classical multi stage Runge-Kutta method and the equation for mass conservation can be enforced using a pressure-corrector type velocity-pressure coupling, with a Poisson equation for the pressure.

In summary the equations to be solved in each Runge Kutta stage k are

$$\boldsymbol{x}^{(k)} = \sum_{l=1}^{k} \Big(\alpha_{kl} \boldsymbol{x}^{(l-1)} + \beta_{kl} \Delta t \boldsymbol{u}_0^{(l-1)} \Big), \tag{3.28a}$$

$$J^{(k)} = \sum_{l=1}^{k} \Big(\alpha_{kl} J^{(l-1)} + \beta_{kl} \Delta t (\nabla \cdot \boldsymbol{u}_0)^{(l-1)} \Big), \tag{3.28b}$$

$$\begin{aligned} (J\boldsymbol{u})^{(k)*} = &\sum_{l=1}^{k-1} \Big(\alpha_{kl} (J\boldsymbol{u})^{(l-1)} + \beta_{kl} \Delta t \boldsymbol{f}_3(\boldsymbol{q}^{(l-1)}) \Big) \\ &+ \alpha_{kk} (J\boldsymbol{u})^{(k-1)} + \beta_{kk} \Delta t \boldsymbol{f}_3^*(t, \boldsymbol{q}^{(k-1)}), \end{aligned} \tag{3.28c}$$

$$\nabla^2 p^{(k-1)} = \frac{\rho}{\beta_{kk} \Delta t} \nabla \cdot \Big(\frac{(J\boldsymbol{u})^{(k)*}}{J^{(k-1)}} \Big), \tag{3.28d}$$

$$(J\boldsymbol{u})^{(k)} = \sum_{l=1}^{k} \Big(\alpha_{kl} (J\boldsymbol{u})^{(l-1)} + \beta_{kl} \Delta t \boldsymbol{f}_3(\boldsymbol{q}^{(l-1)}) \Big), \tag{3.28e}$$

where the right hand side of the incompressible Euler equations is

$$\boldsymbol{f}_3(t, \boldsymbol{q}) = J(\nabla \cdot (-\boldsymbol{u}(\boldsymbol{u} - \boldsymbol{u}_0)^T - \frac{1}{\rho} \mathbf{I} p) + \boldsymbol{g}). \tag{3.29}$$

Chapter 4

Weighted Least Squares and the Generalized Finite Pointset Method

The free-surface flow to be calculated on a moving unstructured point set. The classical finite difference method, as used in Engsig-Karup et al. [2009] is not applicable on an unstructured point set. A generalization of the finite difference method by Iliev and Tiwari [2003] is an extension of the finite difference method, which can be applied to an unstructured point set. It is essentially a least squares approximation of Taylor series and it can be improved by an uneven weighting Zienkiewicz et al. [2005]. The WLS method and a generalization of the original FPM method, Tiwari and Kuhnert [2007], are presented in this chapter. The FPM method is a WLS method with boundary conditions approximated in a least squares sense. The WLS method is applied to the approximation of gradients and divergences in the incompressible and inviscid ALE equations and the GFPM method to the approximation of the Poisson equation for the pressure.

This chapter is organized as follows: First the approximation of the physical domain, solutions and equations are described. Then the WLS method is presented, followed by the GFPM method. Finally higher-order convergence of the GFPM method is demonstrated using solutions to the Poisson equation: One with Dirichlet boundary conditions only and one with both Dirichlet and Neumann boundary conditions. The latter is relevant for free surface flow.

4.1 Numerical Approximation and Solution

The time integration, i.e. the Runge-Kutta method and mass conservation through pressure correction was presented in the previous chapter. The remaining spatial approximations are presented in this chapter. They consists of the approximation of the physical domain Ω and its boundary $\Gamma = \partial\Omega$. The solutions for the volume deformations due to the ALE velocity $\boldsymbol{u}_0$, represented by the Jacobian, $J = J(\boldsymbol{x}, t)$, the velocity $\boldsymbol{u} = \boldsymbol{u}(\boldsymbol{x}, t)$ and the pressure $p = p(\boldsymbol{x}, t)$. The spatial approximations of the equations for conservation of space (2.19), mass (2.20) and momentum (2.21), along with the boundary conditions for free surface (2.22) and (2.23) and wall (2.24).

The physical domain Ω is approximated by a set of N points

$$\mathcal{P}_\Omega = \{\boldsymbol{x}_i : i = 1, \ldots, N \wedge \boldsymbol{x}_i \in \Omega\}, \tag{4.1}$$

where a subset of these points are located directly on the boundary of the physical domain and used for the approximation of the domain boundary

$$\mathcal{P}_\Gamma \subset \mathcal{P}_\Omega = \{\boldsymbol{x}_i : \boldsymbol{x}_i \in \mathcal{P}_\Omega \wedge \boldsymbol{x}_i \in \Gamma\}. \tag{4.2}$$

The boundary points are either located at a wall boundary

$$\mathcal{P}_{\Gamma_{wl}} \subset \mathcal{P}_\Gamma = \{\boldsymbol{x}_i : \boldsymbol{x}_i \in \mathcal{P}_\Gamma \wedge \boldsymbol{x}_i \in \Gamma_{wl}\}, \tag{4.3}$$

or located on a free surface boundary

$$\mathcal{P}_{\Gamma_{fs}} \subset \mathcal{P}_\Gamma = \{\boldsymbol{x}_i : \boldsymbol{x}_i \in \mathcal{P}_\Gamma \wedge \boldsymbol{x}_i \in \Gamma_{fs}\}. \tag{4.4}$$

or as contact points between boundaries, which are the points that are located at the intersection between two boundaries, e.g. the point where a wall boundary meets a free surface boundary. Boundaries are further subdivided into segments of Γ which are C^1 continuous, to facilitate a meaningful approximation of the boundary normal vectors and satisfaction of the wall boundary condition.

The solution for the velocity is approximated by the following local polynomial in a neighbourhood $\Omega(\boldsymbol{x}_i) \subset \Omega$ of each point in $\mathcal{P}_\Omega$

$$\boldsymbol{u}_h(\boldsymbol{x}, t) = \sum_{|\boldsymbol{\alpha}|=0}^{\boldsymbol{\alpha}_{\max}} \boldsymbol{a}_{\boldsymbol{\alpha}}(t)(\boldsymbol{x} - \boldsymbol{x}_i)^{\boldsymbol{\alpha}}, \quad \boldsymbol{x} \in \Omega(\boldsymbol{x}_i), \tag{4.5}$$

where multi-index notation is used and $\boldsymbol{a}_{\boldsymbol{\alpha}}(t)$ is vector of coefficients to the $\boldsymbol{\alpha}$ term in the polynomial. The pressure is also approximated by a local polynomial

$$p_h(\boldsymbol{x}, t) = \sum_{|\boldsymbol{\alpha}|=0}^{\boldsymbol{\alpha}_{\max}} a_{\boldsymbol{\alpha}}(t)(\boldsymbol{x} - \boldsymbol{x}_i)^{\boldsymbol{\alpha}}, \quad \boldsymbol{x} \in \Omega(\boldsymbol{x}_i), \tag{4.6}$$

where $a_{\boldsymbol{\alpha}}(t)$ is the scalar coefficient to the $\boldsymbol{\alpha}$ term in the polynomial. The same local approximation method is used for the Jacobian

$$J_h(\boldsymbol{x}, t) = \sum_{|\boldsymbol{\alpha}|=0}^{\boldsymbol{\alpha}_{\max}} a_{\boldsymbol{\alpha}}(t)(\boldsymbol{x} - \boldsymbol{x}_i)^{\boldsymbol{\alpha}}, \quad \boldsymbol{x} \in \Omega(\boldsymbol{x}_i). \tag{4.7}$$

These solution approximations are inserted in the equations (2.18), (2.19) and (2.21)

$$\frac{d\boldsymbol{x}}{dt} = \boldsymbol{u}_{0,h}, \tag{4.8}$$

$$\frac{\partial J_h}{\partial t} = J_h \nabla \cdot \boldsymbol{u}_{0,h}, \tag{4.9}$$

$$\frac{\partial (J\boldsymbol{u})_h}{\partial t} = J_h(\nabla \cdot (\boldsymbol{u}_h(\boldsymbol{u}_h - \boldsymbol{u}_{0,h})^T - \frac{1}{\rho}\mathbf{I}p_h) + \boldsymbol{g}), \quad \boldsymbol{x} \in \Omega(\boldsymbol{x}_i). \tag{4.10}$$

where the $(J\boldsymbol{u})_h = J_h\boldsymbol{u}_h$. The equations are approximated at the N points in $\mathcal{P}_\Omega$

$$\frac{d\boldsymbol{x}_i}{dt} = \boldsymbol{u}_{0,i}, \tag{4.11}$$

$$\frac{\partial J_i}{\partial t} = J_i(\nabla \cdot \boldsymbol{u}_0)_i, \tag{4.12}$$

$$\frac{\partial (J\boldsymbol{u})_i}{\partial t} = J_i(\nabla \cdot (\boldsymbol{u}_h(\boldsymbol{u}_h - \boldsymbol{u}_{0,h})^T - \frac{1}{\rho}\mathbf{I}p_h) + \boldsymbol{g})_i, \tag{4.13}$$

$$i \in [1, N].$$

where $\boldsymbol{u}_{0,i} = \boldsymbol{u}_{0,h}(\boldsymbol{x}_i, t)$, $J_i = J_h(\boldsymbol{x}_i, t)$ and $p_i = p_h(\boldsymbol{x}_i, t)$. Eventually we have a numerical approximation of N sets of unknowns and N sets of equations which are to be solved in be solved in $\Omega(t) \times [0, t_{\max}]$.

The divergence operators in (4.11), (4.12) and (4.13) are approximated by a WLS approximation of the Taylor series based on an unstructured stencil in a neighbourhood of each point in $\mathcal{P}_\Omega$.

4.2 Weighted Least Squares Approximations via Taylor Series

The WLS method is presented using multi-index notation, see appendix A. In this notation gradient of a scalar function $f = f(\boldsymbol{x}) \in \mathbb{R},\ \boldsymbol{x} \in \mathbb{R}^2$ is

$$\nabla f = \begin{bmatrix} D^{(1,0)} f \\ D^{(0,1)} f \end{bmatrix}, \tag{4.14}$$

the divergence of a vector function $\boldsymbol{f} = \boldsymbol{f}(\boldsymbol{x}) \in \mathbb{R}^2,\ \boldsymbol{x} \in \mathbb{R}^2$ is

$$\nabla \cdot \boldsymbol{f} = D^{(1,0)} f_1 + D^{(0,1)} f_2. \tag{4.15}$$

and the Taylor series approximation of a function $f(\boldsymbol{y})$ in a neighbourhood of $\boldsymbol{x}$, based on the derivatives of the function $D^{\boldsymbol{\alpha}} f(\boldsymbol{x})$, is

$$f(\boldsymbol{y}) = \sum_{|\boldsymbol{\alpha}|=0}^{\infty} \frac{(\boldsymbol{y} - \boldsymbol{x})^{\boldsymbol{\alpha}}}{\boldsymbol{\alpha}!} D^{\boldsymbol{\alpha}} f(\boldsymbol{x}). \tag{4.16}$$

To each of the points in $\mathcal{P}_\Omega$ we associate a stencil

$$\mathcal{S}_i = \bigcup_{k=1}^{N_{\mathcal{S}}} \boldsymbol{x}_{j(k)}, \tag{4.17}$$

where $N_{\mathcal{S}}$ is the size of the stencil and $j(k)$ is a mapping from the local index k to the global index j. The first point in the stencil is always $j(1) = i$. The Taylor series approximation of a function at all of the points in the stencil $\mathcal{S}_i$ based on the derivatives at $\boldsymbol{x}_i$ are

$$f(\boldsymbol{x}_j) = \sum_{|\boldsymbol{\alpha}|=0}^{\infty} \frac{(\boldsymbol{x}_j - \boldsymbol{x}_i)^{\boldsymbol{\alpha}}}{\boldsymbol{\alpha}!} (D^{\boldsymbol{\alpha}} f(\boldsymbol{x}))_i, \quad \forall \boldsymbol{x}_j \in \mathcal{S}_i. \tag{4.18}$$

Assuming the polynomial approximation of the function $f(\boldsymbol{x})$

$$f(\boldsymbol{x}) \approx f_h(\boldsymbol{x}) = \sum_{|\boldsymbol{\alpha}|=0}^{\boldsymbol{\alpha}_{\max}} a_{\boldsymbol{\alpha}} (\boldsymbol{x} - \boldsymbol{x}_i)^{\boldsymbol{\alpha}}, \quad \boldsymbol{x} \in \Omega(\boldsymbol{x}_i), \tag{4.19}$$

and truncating the Taylor series at $\boldsymbol{\alpha}_{\max}$ gives the following approximation of the Taylor series

$$f_j \approx \sum_{|\boldsymbol{\alpha}|=0}^{\boldsymbol{\alpha}_{max}} \frac{(\boldsymbol{x}_j - \boldsymbol{x}_i)^{\boldsymbol{\alpha}}}{\boldsymbol{\alpha}!} (D^{\boldsymbol{\alpha}} f_h)_i, \quad \forall \boldsymbol{x}_j \in \mathcal{S}_i, \tag{4.20}$$

where $(D^{\boldsymbol{\alpha}} f_h)_i$ is the numerical approximation of the $\boldsymbol{\alpha}$ derivative at the point $\boldsymbol{x}_i$. By collecting Taylor series expansions into an overdetermined system of $N_{\mathcal{S}}$ equations and $N_p = \frac{1}{2}(p+1)(p+2)$ unknowns, where $p = |\boldsymbol{\alpha}_{\max}|$, assuming that the number of points in the stencil is greater than the number of terms in the Taylor series. The Taylor series are arranged in a linear system of equations

$$\begin{bmatrix} \sum_{|\boldsymbol{\alpha}|=0}^{\boldsymbol{\alpha}_{\max}} \frac{(\boldsymbol{x}_{j_1} - \boldsymbol{x}_i)^{\boldsymbol{\alpha}}}{\boldsymbol{\alpha}!} (D^{\boldsymbol{\alpha}} f_h)_i \\ \vdots \\ \sum_{|\boldsymbol{\alpha}|=0}^{\boldsymbol{\alpha}_{\max}} \frac{(\boldsymbol{x}_{j_{N_{\mathcal{S}}}} - \boldsymbol{x}_i)^{\boldsymbol{\alpha}}}{\boldsymbol{\alpha}!} (D^{\boldsymbol{\alpha}} f_h)_i \end{bmatrix} = \begin{bmatrix} f_{j_1} \\ \vdots \\ f_{j_{N_{\mathcal{S}}}} \end{bmatrix}, \tag{4.21}$$

which on matrix form is

$$\boldsymbol{A}\boldsymbol{d} = \boldsymbol{b} \tag{4.22}$$

where $\boldsymbol{d}$ contains the derivative approximations

$$\boldsymbol{d} = \begin{bmatrix} (D^{\boldsymbol{0}} f_h)_i \\ \vdots \\ (D^{\boldsymbol{\alpha}_{max}} f_h)_i \end{bmatrix}, \tag{4.23}$$

and the right hand side $\boldsymbol{b}$ contains the function values in the stencil

$$\boldsymbol{b} = \begin{bmatrix} f_{j_1} \\ \vdots \\ f_{j_{N_{\mathcal{S}}}} \end{bmatrix}, \tag{4.24}$$

This linear system of equations is overdetermined and the best possible solution to $\boldsymbol{d}$ is found by solving the weighted quadratic minimization problem

$$\boldsymbol{d} = \arg\min_{\boldsymbol{d}} J(\boldsymbol{d}), \tag{4.25}$$

where the objective function is given by

$$J(\boldsymbol{d}) = \boldsymbol{r}^T \boldsymbol{W} \boldsymbol{r}, \quad \boldsymbol{r} = \boldsymbol{b} - \boldsymbol{A}\boldsymbol{d}, \tag{4.26}$$

in which $\boldsymbol{r}$ is the residual of the linear system of equations and $\boldsymbol{W}$ is a matrix with the weights on the diagonal

$$\boldsymbol{W} = \begin{bmatrix} w_1 & & \\ & \ddots & \\ & & w_{N_{\mathcal{S}}} \end{bmatrix}. \tag{4.27}$$

The minimization gives the weighted normal equations

$$\boldsymbol{A}^T \boldsymbol{W} \boldsymbol{A} \boldsymbol{d} = \boldsymbol{A}^T \boldsymbol{W} \boldsymbol{b}, \tag{4.28}$$

which has an unique solution provided that the matrix $\boldsymbol{A}^T \boldsymbol{W} \boldsymbol{A}$ is non-singular. The vector containing the derivative approximations is

$$\boldsymbol{d} = [\boldsymbol{A}^T \boldsymbol{W} \boldsymbol{A}]^{-1} \boldsymbol{A}^T \boldsymbol{W} \boldsymbol{b}. \tag{4.29}$$

Hence the coefficients for the numerical approximation of the $\boldsymbol{\alpha} = (0,0), \ldots, \boldsymbol{\alpha}_{max}$ derivative is contained in the matrix

$$\boldsymbol{C} = [\boldsymbol{A}^T \boldsymbol{W} \boldsymbol{A}]^{-1} \boldsymbol{A}^T \boldsymbol{W}. \tag{4.30}$$

The coefficients for the $D^{(1,0)}$ derivative are in the second row of $\boldsymbol{C}$ and the coefficients for the $D^{(0,1)}$ are in the $p+2$ row of $\boldsymbol{C}$. This has similarities to the way the coefficients are identified in the finite difference method and therefore this method is also presented as the finite difference method for arbitrary irregular grids by Liszka and Orkisz [1980].

Choice of Weighting Function

There is much freedom in the choice of the weights $\boldsymbol{W}$. The identity matrix $\boldsymbol{W} = \boldsymbol{I}$ gives the least squares method, but this choice is not optimal, Zienkiewicz et al. [2005]. The least squares approximation can be improved by choosing the weights as a monotone decreasing function of the distance from the center point $r = \sqrt{(\boldsymbol{x}_j - \boldsymbol{x}_i)^2}$. There are many different weighting functions and, based on the vast variety used in approximations on scattered data points, the choice of weighting function seem more like art than science. The exponential Gauss function is suggested in Zienkiewicz et al. [2005] and it is applied in the form

$$w(r) = \exp\left(\frac{-(r-\mu)^2}{2\sigma^2}\right), \tag{4.31}$$

where μ is the mean distance from the center point $\boldsymbol{x}_i$ to its stencil points $\boldsymbol{x}_j \in \mathcal{S}_i$ and σ is the variance of the distance to the stencil points.

Choice of Stencil

The stencil for each of the the points are the $N_{\mathcal{S}}$ nearest neighbours in a modified Delaunay graph, see de Berg et al. [2008]. The nearest neighbours are found using a breadth first search (BFS) in the graph, see Cormen et al. [2009]. The number of neighbours is based on the order of the approximation. The number of terms in the complete polynomial basis is $N_p = \frac{1}{2}(p+1)(p+2)$ and the number of neighbours are $N_{\mathcal{S}} = 3N_p$.

4.3 A Generalized Finite Pointset Method

The method presented in Tiwari and Kuhnert [2007] is of second order accuracy and the present method is a generalization of this method to arbitrary order accuracy. Mass conservation is ensure by a pressure field that satisfies the Poisson equation (3.28d) which is approximated at each point in $\mathcal{P}_\Omega$

$$(\nabla^2 p_h^{(k-1)})_i = \frac{\rho}{\beta_{kk}\Delta t}\left(\nabla \cdot \left(\frac{(J\boldsymbol{u})_h^{(k)*}}{J_h^{(k-1)}}\right)\right)_i, \quad i \in [1, N], \tag{4.32}$$

with the inhomogeneous Neumann boundary condition (3.27)

$$\boldsymbol{n} \cdot (\nabla p_h^{(k-1)})_i = \frac{\rho}{J_i^{(k-1)}\beta_{kk}\Delta t} \boldsymbol{n} \cdot (J\boldsymbol{u})_i^{(k)*}, \quad i \in \mathcal{P}_{\Gamma_{wl}}, \tag{4.33}$$

and the homogeneous Dirichlet boundary condition at the free surface

$$p_i^{(k-1)} = 0, \quad i \in \mathcal{P}_{\Gamma_{fs}}. \tag{4.34}$$

The Poisson equation and the boundary conditions above are approximated by a generalized version of the finite pointset method. The FPM method, proposed by Tiwari and Kuhnert [2007], is similar to the WLS approximation presented in the previous section. In the FPM method, the Taylor series are approximated together with an elliptic partial differential equation and a set of boundary conditions. The multi index notation is also used in the presentation of the GFPM.

If L is an elliptic partial differential operator, its discrete approximation in the neighbourhood of a point $\boldsymbol{x}_i$ is

$$Lf(\boldsymbol{x}) \approx Lf_h(\boldsymbol{x}) = \sum_{|\boldsymbol{\alpha}|=0}^{\boldsymbol{\alpha}_{max}} a_{\boldsymbol{\alpha}} D^{\boldsymbol{\alpha}} f_h(\boldsymbol{x}) = g_{PDE}(\boldsymbol{x}), \tag{4.35}$$

where the function f is approximated by the polynomial (4.19). Similarly, the discrete approximation of the boundary condition B at a point $\boldsymbol{x}_i$ on the boundary is

$$Bf(\boldsymbol{x}) \approx Bf_h(\boldsymbol{x}) = \sum_{|\boldsymbol{\alpha}|=0}^{\boldsymbol{\alpha}_{max}} b_{\boldsymbol{\alpha}} D^{\boldsymbol{\alpha}} f_h(\boldsymbol{x}) = g_{BC}(\boldsymbol{x}). \tag{4.36}$$

These equations are to be approximated along with standard derivative approximations in the Taylor series expansions (4.20). Recall that the Taylor series are truncated at $\boldsymbol{\alpha} = \boldsymbol{\alpha}_{max}$, therefore this is also the maximum possible order of the partial differential equations and the boundary conditions. Consider a point $\boldsymbol{x}_i \in \mathcal{P}_\Omega$ and the points in its stencil $\boldsymbol{x}_j \in \mathcal{S}_i$. Do the Taylor series expansion from $\boldsymbol{x}_i$ to all the points in its stencil, arrange them in a linear system of equations together with the partial differential equation and the boundary conditions (if $\boldsymbol{x}_i$ is a boundary point)

$$\begin{bmatrix} \sum_{|\boldsymbol{\alpha}|=0}^{\boldsymbol{\alpha}_{\max}} \frac{(\boldsymbol{x}_i - \boldsymbol{x}_{j_1})^{\boldsymbol{\alpha}}}{\boldsymbol{\alpha}!} (D^{\boldsymbol{\alpha}} f_h)_i \\ \vdots \\ \sum_{|\boldsymbol{\alpha}|=0}^{\boldsymbol{\alpha}_{\max}} \frac{(\boldsymbol{x}_i - \boldsymbol{x}_{j_{N_S}})^{\boldsymbol{\alpha}}}{\boldsymbol{\alpha}!} (D^{\boldsymbol{\alpha}} f_h)_i \\ \sum_{|\boldsymbol{\alpha}|=0}^{\boldsymbol{\alpha}_{\max}} a_{\boldsymbol{\alpha}} (D^{\boldsymbol{\alpha}} f_h)_i \\ \sum_{|\boldsymbol{\alpha}|=0}^{\boldsymbol{\alpha}_{\max}} b_{\boldsymbol{\alpha}} (D^{\boldsymbol{\alpha}} f_h)_i \end{bmatrix} = \begin{bmatrix} f_{j_1} \\ \vdots \\ f_{j_{N_S}} \\ g_{PDE} \\ g_{BC} \end{bmatrix}, \tag{4.37}$$

As in the derivation of the WLS method the equations are written in the form

$$\boldsymbol{A}\boldsymbol{d} = \boldsymbol{b}, \tag{4.38}$$

where the matrix $\boldsymbol{A}$ holds all the coefficients of the Taylor series, partial differential equation and the boundary conditions, the vector $\boldsymbol{d}$ is the same as for the weighted least squares method (4.23), but the right hand side has both the function values at the points in the stencil for $\boldsymbol{x}_i$, and the right hand sides of the partial differential equation and the boundary conditions. This linear system of equations is overdetermined and solved by the weighted quadratic minimization (4.25) and with the objective function (4.26). The

weights for the partial differential equation and the boundary conditions are unity and the weights for the Taylor series are again given by (4.31)

$$\boldsymbol{W} = \begin{bmatrix} w_1 & & & & & \\ & \ddots & & & & \\ & & w_{N_S} & & & \\ & & & 1 & & \\ & & & & 1 & \end{bmatrix}. \tag{4.39}$$

The solution to the weighted quadratic minimization problem is (4.29), where the $\boldsymbol{A}$, $\boldsymbol{W}$, and $\boldsymbol{b}$ are given according to the GFPM method. Once the linear system of equations has been solved the derivative approximations are

$$\boldsymbol{d} = [\boldsymbol{A}^T\boldsymbol{W}\boldsymbol{A}]^{-1}\boldsymbol{A}^T\boldsymbol{W}\boldsymbol{b}. \tag{4.40}$$

We denote the first row of the inverted matrix as $[\boldsymbol{A}^T\boldsymbol{W}\boldsymbol{A}]_1^{-1}$, and the approximation of the zeroth derivative (the function value) is

$$f_i = [\boldsymbol{A}^T\boldsymbol{W}\boldsymbol{A}]_1^{-1}\boldsymbol{A}^T\boldsymbol{W}\boldsymbol{b}. \tag{4.41}$$

Now split $\boldsymbol{A}$ and $\boldsymbol{W}\boldsymbol{b}$ in the parts with the Taylor series, the partial differential equation and the boundary condition

$$\boldsymbol{A} = \begin{bmatrix} \boldsymbol{A}_{TAY} \\ \boldsymbol{A}_{PDE} \\ \boldsymbol{A}_{BC} \end{bmatrix}, \quad \boldsymbol{W}\boldsymbol{b} = \begin{bmatrix} (\boldsymbol{W}\boldsymbol{b})_{TAY} \\ (\boldsymbol{W}\boldsymbol{b})_{PDE} \\ (\boldsymbol{W}\boldsymbol{b})_{BC} \end{bmatrix} = \begin{bmatrix} (\boldsymbol{W}\boldsymbol{b})_{TAY} \\ g_{PDE} \\ g_{BC} \end{bmatrix}, \tag{4.42}$$

and write the implicit equation for all the points in the domain

$$\begin{aligned} f_i - [\boldsymbol{A}^T\boldsymbol{W}\boldsymbol{A}]_1^{-1}(\boldsymbol{A}^T\boldsymbol{W}\boldsymbol{b})_{TAY} &= [\boldsymbol{A}^T\boldsymbol{W}\boldsymbol{A}]_1^{-1}\boldsymbol{A}_{PDE}^T g_{PDE} \\ &\quad + [\boldsymbol{A}^T\boldsymbol{W}\boldsymbol{A}]_1^{-1}\boldsymbol{A}_{BC}^T g_{BC}, \quad \forall i \in \mathcal{P}_\Omega. \end{aligned} \tag{4.43}$$

The resultant linear system of equations, with the size $N_p \times N_p$, is solved and the solution approximates the derivatives, the partial differential equation and the boundary conditions.

4.4 Improvement of Conditioning

Consider a GFPM approximation of the Poisson equation with Dirichlet boundary conditions on an even grid in one dimension. The condition number of the matrix $\boldsymbol{A}\boldsymbol{W}\boldsymbol{A}^T$ for different uniform mesh with the distance between the points given by Δx and orders of the Taylor series p are seen in figure 4.1. Clearly the matrix i poorly conditioned for smaller grid sizes and higher order. The conditioning can be improved by scaling of the argument in the Taylor series, partial differential equations and the boundary conditions. Scaling of the Taylor series with a length scale h gives

$$f_j = \sum_{|\boldsymbol{\alpha}|=0}^{\boldsymbol{\alpha}_{max}} \frac{h^{|\boldsymbol{\alpha}|}}{\boldsymbol{\alpha}!}\left(\frac{\boldsymbol{x}_j - \boldsymbol{x}_i}{h}\right)^{\boldsymbol{\alpha}} \mathcal{D}^{\boldsymbol{\alpha}} f_i, \quad \boldsymbol{x}_j \in \mathcal{S}(\boldsymbol{x}_i). \tag{4.44}$$

The maximum condition number as a function of point spacing and order of approximation is seen in figure 4.1. The scaling of the Taylor series made the condition number independent of Δx, but still growing as the order increases. All GFPM calculations to be presented are with the scaling of the Taylor series. In more complex situations, than this simple one dimensional problem, the scaling factor is the fill distance, see Wendland [2005].

4.5 Truncation Error Analysis

The theoretical truncation errors of the GFPM method in one dimension are given for 2nd and 8th order approximations and 3 to 11 points in the stencils. The points are uniformly distributed in the analysis. One specific example is presented in more details for 2nd order and 5 points in the stencil and the rest are presented in a tabulated form.

Consider the Poisson equation in one dimension

$$\frac{\partial^2 \phi}{\partial x^2} = f(x), \tag{4.45}$$

and the 2nd order centered GFPM approximation on a 5 point uniform stencil with uniform weighting

$$\left(\frac{\partial^2 \phi}{\partial x^2}\right)_i \approx \frac{1}{10\Delta x^2} \begin{bmatrix} 2-3dx^4 \\ 2+12dx^4 \\ -8-18dx^4 \\ 2+12dx^4 \\ 2-3dx^4 \end{bmatrix}^T \begin{bmatrix} \phi_{i-2} \\ \phi_{i-1} \\ \phi_i \\ \phi_{i+1} \\ \phi_{i+2} \end{bmatrix}. \tag{4.46}$$

Insertion of the Taylor expansions of $\phi(x)$ around x_i gives the error

$$e = \frac{17\Delta x^2}{60}\left(\frac{\partial^4 \phi}{\partial x^4}\right)_i + \ldots, \tag{4.47}$$

hence leading term is proportional to Δx^2 and the truncation error is of 2nd order. The table 4.1 shows the leading error terms for approximations with order of Taylor series $p = 2, \ldots, 8$ and number of points in the stencil $N_{\mathcal{S}} = 3, 5, 7, 9, 11$. From the table it is seen at there is an odd-even pattern in the truncation errors: Truncation of the Taylor series at $p = 2$ and $p = 3$ gives a 2nd order truncation error, $p = 4$ and $p = 5$ gives 4th order, $p = 6$ and $p = 7$ gives 6th order and finally $p = 8$ gives 8th order.

4.6 Verification

Numerical test of increasing difficulty are carried out to verify the convergence rates of the GFPM.

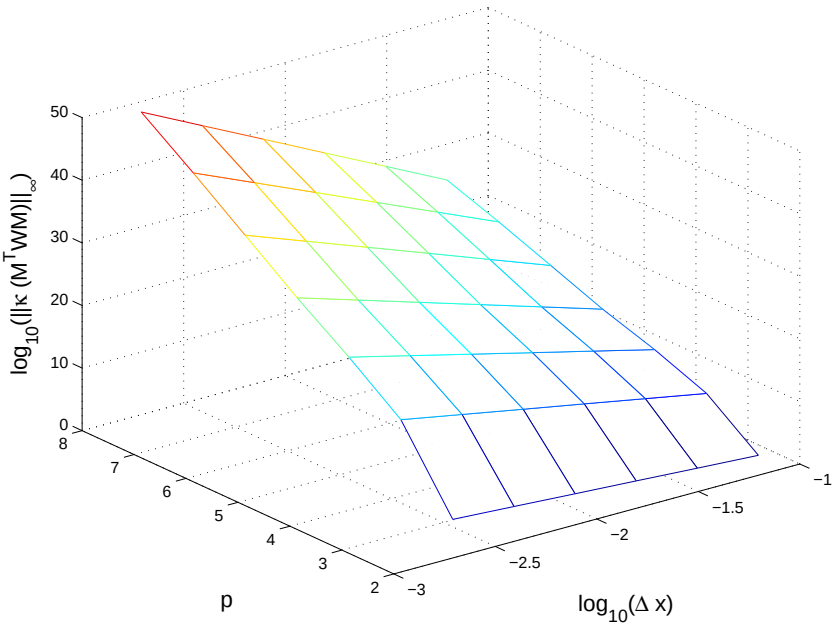

(a) Without scaling.

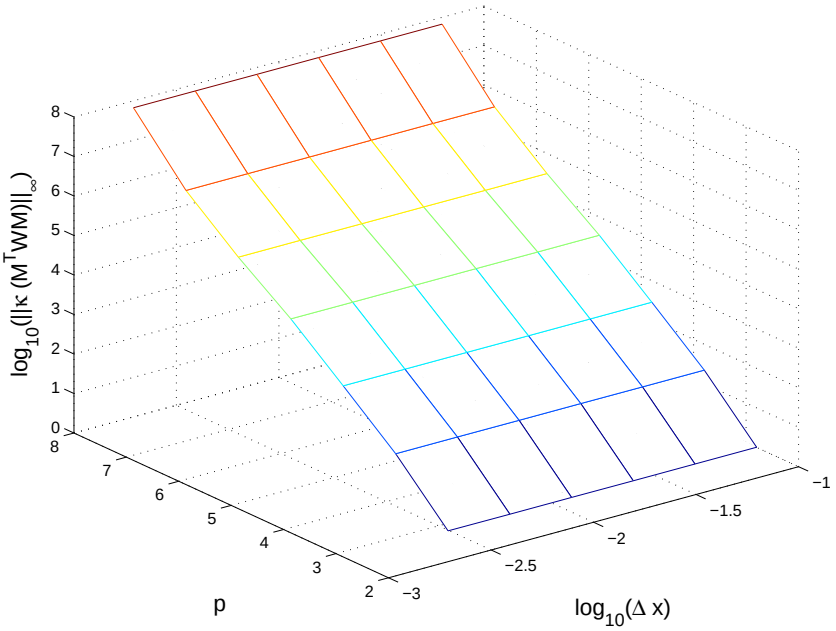

(b) With scaling.

Figure 4.1: The maximum condition numbers as a function of Δx and p with and without scaling of the Taylor series.

p / $N_{\mathcal{S}}$	3	5	7	9	11
2	$\frac{1}{12}\Delta x^2\phi_i^{(4)}$	$\frac{17}{60}\Delta x^2\phi_i^{(4)}$	$\frac{7}{12}\Delta x^2\phi_i^{(4)}$	$\frac{59}{60}\Delta x^2\phi_i^{(4)}$	$\frac{89}{60}\Delta x^2\phi_i^{(4)}$
3		$\frac{17}{60}\Delta x^2\phi_i^{(4)}$	$\frac{7}{12}\Delta x^2\phi_i^{(4)}$	$\frac{59}{60}\Delta x^2\phi_i^{(4)}$	$\frac{89}{60}\Delta x^2\phi_i^{(4)}$
4		$-\frac{1}{90}\Delta x^4\phi_i^{(6)}$	$-\frac{47}{630}\Delta x^4\phi_i^{(6)}$	$-\frac{8947}{36630}\Delta x^4\phi_i^{(6)}$	$-\frac{11141}{18810}\Delta x^4\phi_i^{(6)}$
5			$-\frac{47}{630}\Delta x^4\phi_i^{(6)}$	$-\frac{8947}{36630}\Delta x^4\phi_i^{(6)}$	$-\frac{11141}{18810}\Delta x^4\phi_i^{(6)}$
6			$\frac{1}{560}\Delta x^6\phi_i^{(8)}$	$\frac{8601}{448112}\Delta x^6\phi_i^{(8)}$	$\frac{191497}{2173808}\Delta x^6\phi_i^{(8)}$
7				$\frac{8601}{448112}\Delta x^6\phi_i^{(8)}$	$\frac{191497}{2173808}\Delta x^6\phi_i^{(8)}$
8				$-\frac{1}{3150}\Delta x^8\phi_i^{(10)}$	$-\frac{1644701}{336501900}\Delta x^8\phi_i^{(10)}$

Table 4.1: Truncation errors of the GFPM method in one dimension for Taylor series $p = 2, \ldots, 8$ and number of points in the stencil $N_{\mathcal{S}} = 3, 5, 7, 9, 11$.

Poisson's equation in one-dimension with Dirichlet boundary conditions

In the following section numerical tests are presented to verify the convergence of the GFPM method in one spatial dimension. The equation used in the test is the one dimensional Poisson equation

$$\frac{\partial^2\phi}{\partial x^2} = f(x), \quad x \in [0,1], \tag{4.48}$$

where the right hand side is calculated according to the solution

$$\phi(x) = \exp\left(\sin\left(2\pi x\right)\right), \quad x \in [0,1], \tag{4.49}$$

and Dirichlet boundary conditions in both ends of the domain

$$\phi(0) = 1, \quad \phi(1) = 1. \tag{4.50}$$

The test function, equation 4.49, is seen in figure 4.2 together with a convergence analysis of the GFPM method for different Δx and p are seen in figure 4.2. We find that the $p = 2$ and $p = 3$ gives $\mathcal{O}(h^2)$ convergence, and $p = 3$ and $p = 4$ gives $\mathcal{O}(h^4)$ convergence. The error for $p = 6, 7, 8$ are at machine precision for small Δx, but the inspection of the curves shows that $\mathcal{O}(h^6)$ and $\mathcal{O}(h^8)$ has been obtained for the errors above the machine precision level. In this analysis the number of points in the support of the are $p + 1$ for p even and $p + 2$ for p odd. This gives symmetric supports (or in the finite difference terminology: centered stencils) for all the points not close to a boundary. For the points close to or at the boundaries the supports (or stencils) are one-sided.

Poisson's equation in two-dimension with Dirichlet boundary conditions

Consider the Poisson equation in two-dimensions

$$\frac{\partial^2\phi}{\partial x^2} + \frac{\partial^2\phi}{\partial y^2} = f(x,y), \quad (x,y) = [0,1] \times [0,1], \tag{4.51}$$

with inhomogeneous Dirichlet boundary conditions according to the exact solution

$$\phi(x,y) = \exp\left(\sin\left(2\pi x\right) + \sin\left(2\pi y\right)\right), \quad (x,y) \in [0,1] \times [0,1]. \tag{4.52}$$

The test function is seen en figure 4.3.

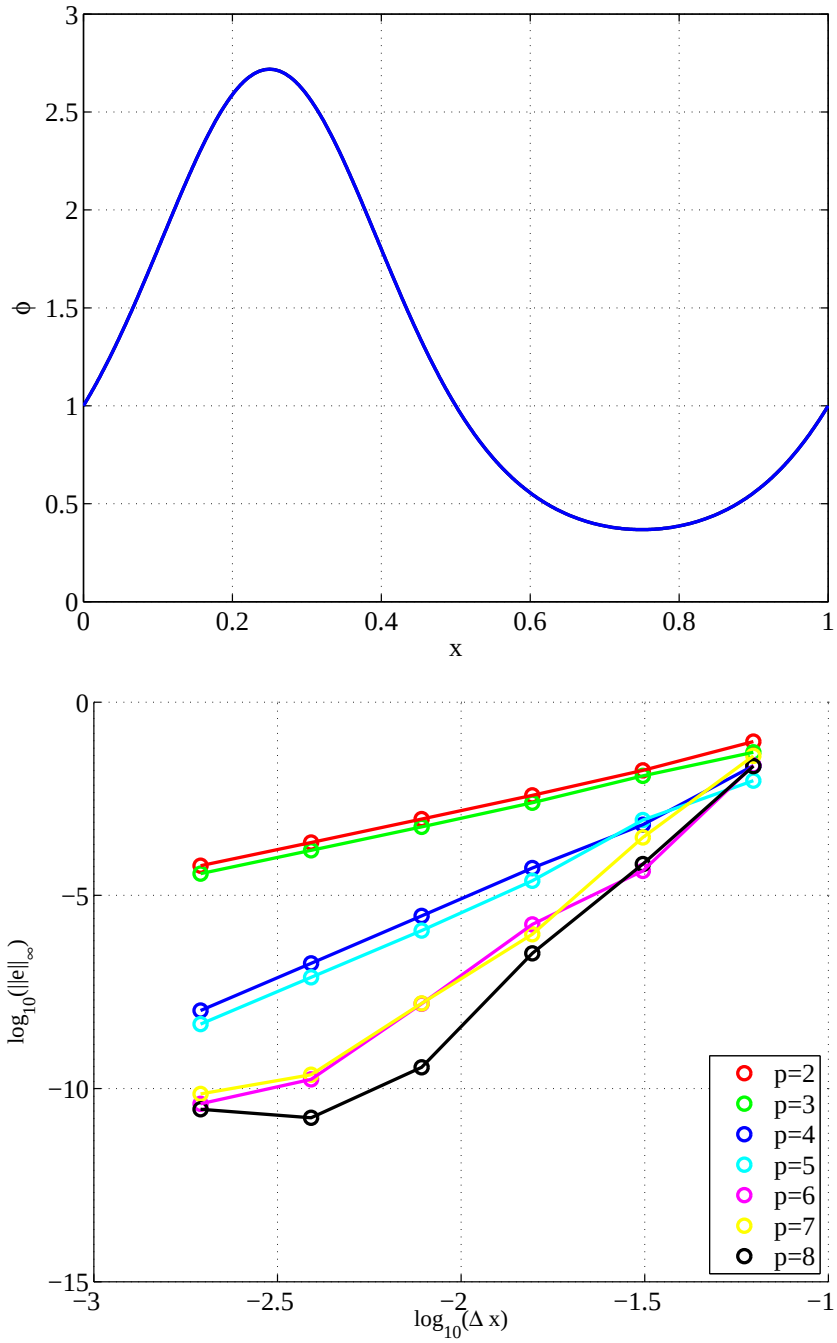

Figure 4.2: The one dimensional test function, (4.49), and the convergence analysis of the GFPM method on an equidistant grid and with Dirichlet boundary conditions.

Poisson's equation in two-dimension with Dirichlet and Neumann boundary conditions

The Poisson equation in two-dimensions is used again

$$\frac{\partial^2 \phi}{\partial x^2} + \frac{\partial^2 \phi}{\partial y^2} = f(x, y), \quad (x, y) = [0, 1] \times [0, 1], \tag{4.53}$$

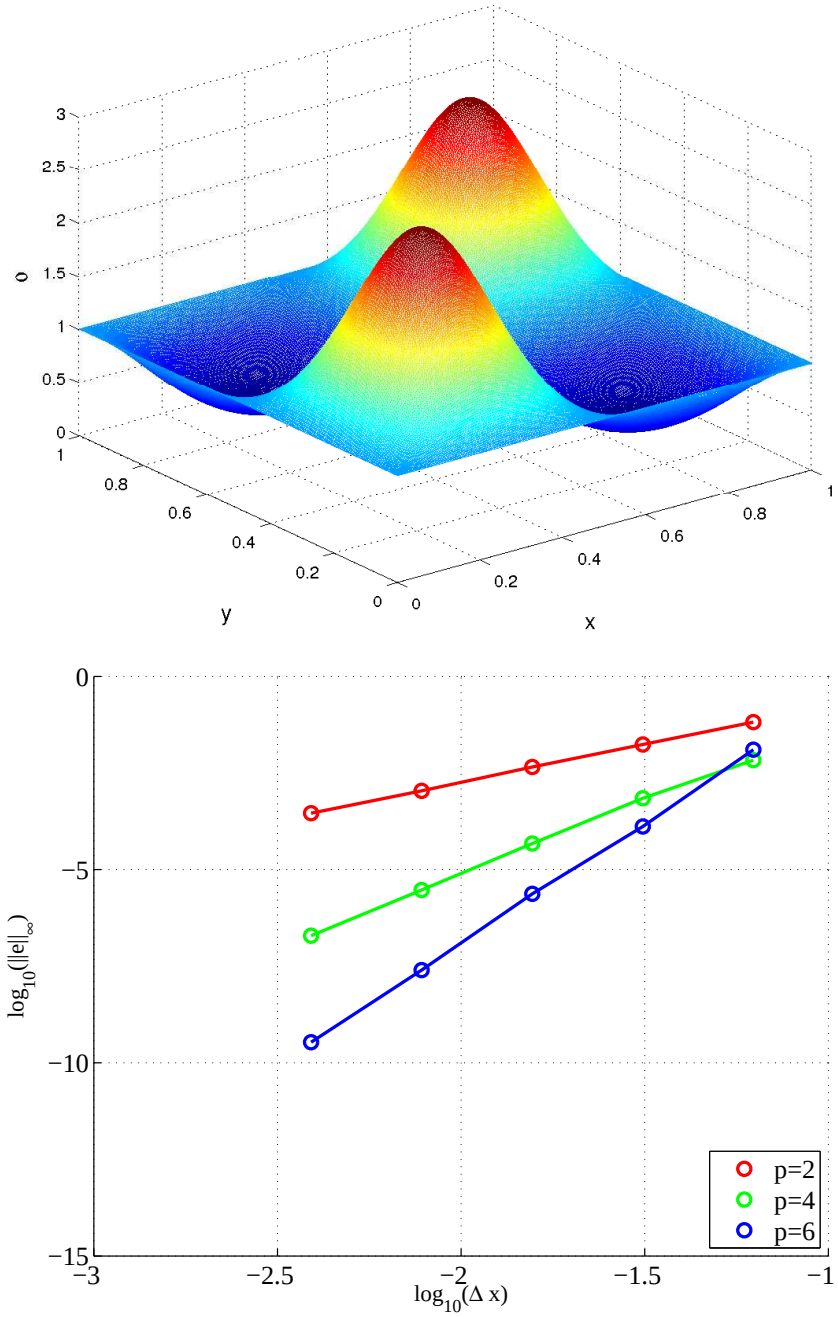

Figure 4.3: The two dimensional test function, (4.52), and the convergence analysis of the GFPM method on an uniform point distribution (similar to a uniform structured grid) and with Dirichlet boundary conditions.

with inhomogeneous Dirichlet boundary conditions according to the exact solution on the lower and left boundaries and homogeneous Neumann boundary conditions on the right and upper boundaries. The test function for the convergence analysis is

$$\phi(x, y) = \exp\left(\sin\left(\pi x/2\right) + \sin\left(\pi y/2\right)\right), \quad (x, y) \in [0, 1] \times [0, 1]. \tag{4.54}$$

The test function and convergence results are seen in figure 4.4.

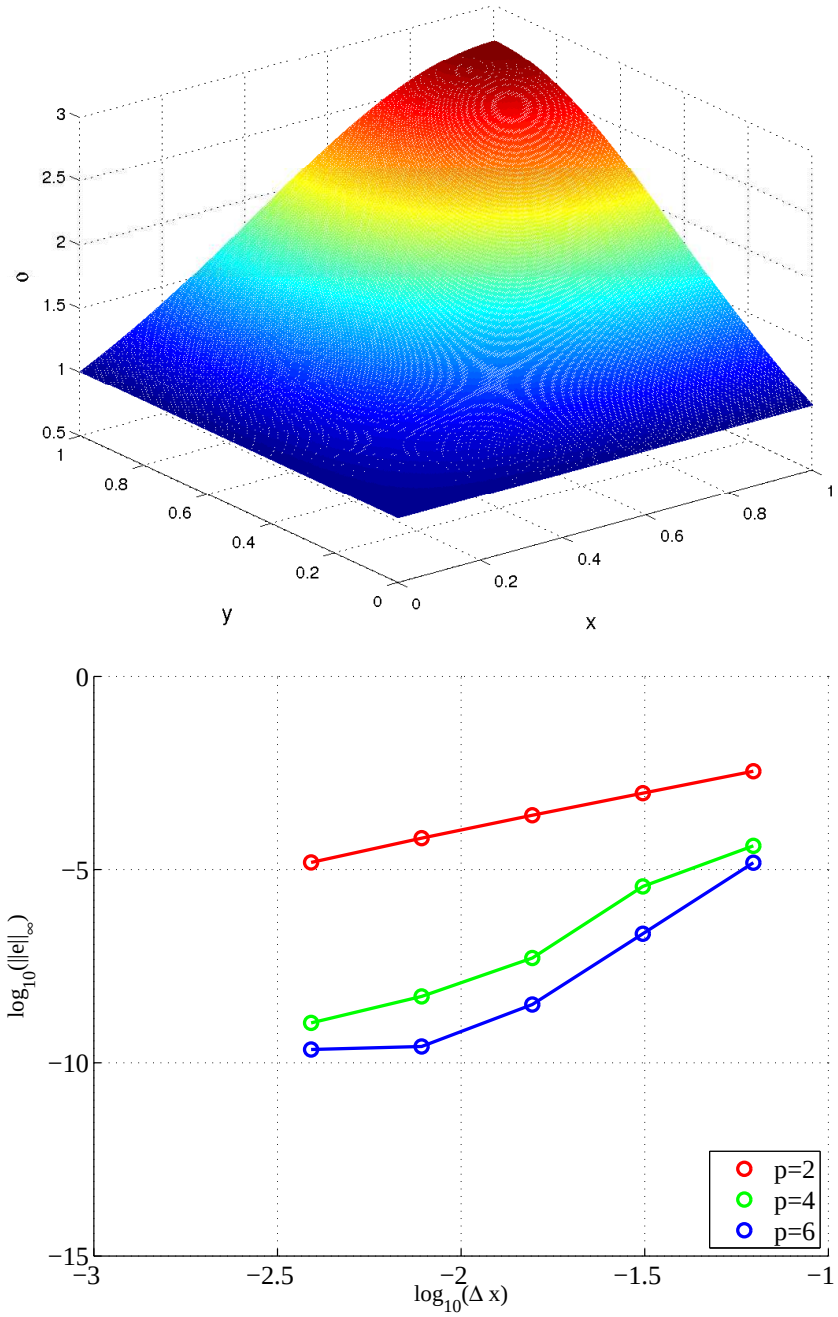

Figure 4.4: The two dimensional test function (4.54), and the convergence analysis of the GFPM method on an uniform point distribution $\Delta x = \Delta y$ and with Dirichlet and Neumann boundary conditions.

Chapter 5

Weighted Least Squares Approximate Riemann Solver

The divergence term in the momentum equation (4.13) is hyperbolic and it can cause the solution for the momentum to develop steep gradients. In the vicinity of the steep gradients the polynomial solution approximation can develop spurious oscillations. Special attention has to be given to the hyperbolic term in order to avoid oscillations, see Toro [1999].

A combination of the WLS method and approximate Riemann solutions, Toro [1999], is a possible method for dealing with the hyperbolic term. The Riemann problem on the unstructured point set appears between the solution at a point $\boldsymbol{x}_i \in \mathcal{P}_\Omega$ and the solution at a point in its stencil $\boldsymbol{x}_j \in \mathcal{S}_i$. The method based on WLS is described in this chapter.

5.1 Weighted Least Squares Differential Quadrature

An approximate Riemann solver method called "Radial Basis Function Differential Quadrature" (RBFDQ) was introduced by Shu et al. [2004]. Like in the WLS method, the radial basis functions can be applied to derivative approximation on an unstructured set of points. The radial basis function method can suffer from poor convergence Shu et al. [2004]. The WLS method on the other hand has convergence properties that are comparable to the finite difference method as seen in chapter 4. The radial basis function is therefore replaced by the WLS method in the RBFDQ method and the procedure is described below.

The conservation equations for space and momentum written in the form of a system of hyperbolic equations (with a non-reactive source term) in a ALE frame of reference moving with the velocity $\boldsymbol{u}_0$

$$\frac{\partial(J\boldsymbol{q})}{\partial t} + J\nabla \cdot (\mathbf{F}(\boldsymbol{q}) - \boldsymbol{q}\boldsymbol{u}_0^T) = J\boldsymbol{s}, \tag{5.1}$$

where the solution vector, flux tensor and right hand side vector are

$$\boldsymbol{q} = \begin{bmatrix} 1 \\ \boldsymbol{u} \end{bmatrix}, \quad \mathbf{F}(\boldsymbol{q}) = \begin{bmatrix} \mathbf{0}^T \\ \boldsymbol{u}\boldsymbol{u}^T + \frac{1}{\rho}\mathbf{I}p \end{bmatrix}, \quad \boldsymbol{s} = \begin{bmatrix} 0 \\ \boldsymbol{g} \end{bmatrix}, \tag{5.2}$$

The numerical approximation of the hyperbolic system equations is

$$\frac{\partial(J_i \boldsymbol{q}_i)}{\partial t} + J_i(\nabla \cdot (\mathbf{F}(\boldsymbol{q}_h) - \boldsymbol{q}_h \boldsymbol{u}_{0,h}^T))_i = J_i \boldsymbol{s}. \tag{5.3}$$

and the numerical approximation of the divergence of the flux tensor is

$$\begin{aligned}(\nabla \cdot \mathbf{F}(\boldsymbol{q}_h))_i &= (D^{(1,0)}\mathbf{F}_1(\boldsymbol{q}_h) + D^{(0,1)}\mathbf{F}_2(\boldsymbol{q}_h))_i &(5.4)\\ &\approx \sum_{j \in \mathcal{S}_i} (w_{ij}^{(1,0)}\mathbf{F}_1(\boldsymbol{q}_j) + w_{ij}^{(0,1)}\mathbf{F}_2(\boldsymbol{q}_j)) &(5.5)\end{aligned}$$

where $w_{ij}^{\boldsymbol{\alpha}}$ is the weight associated the function value at point the $\boldsymbol{x}_j$ to approximate the with the $\boldsymbol{\alpha}$ derivative at the point $\boldsymbol{x}_i$. The objective is to formulate the equation in the form of an one dimensional Riemann problem as defined in Ferrari et al. [2009] and the following scaling of the coefficients is introduced for this purpose

$$\begin{aligned}W_{ij} &= \sqrt{(w_{ij}^{(1,0)})^2 + (w_{ij}^{(0,1)})^2}, &(5.6)\\ \tilde{w}_{ij}^{(1,0)} &= \frac{w_{ij}^{(1,0)}}{W_{ij}}, &(5.7)\\ \tilde{w}_{ij}^{(0,1)} &= \frac{w_{ij}^{(0,1)}}{W_{ij}}. &(5.8)\end{aligned}$$

The approximation of the divergence of the flux tensor is then

$$\begin{aligned}(\nabla \cdot \mathbf{F}(\boldsymbol{q}_h))_i &\approx \sum_{j \in \mathcal{S}_i} W_{ij}(\tilde{w}_{ij}^{(1,0)}\mathbf{F}_1(\boldsymbol{q}_j) + \tilde{w}_{ij}^{(0,1)}\mathbf{F}_2(\boldsymbol{q}_j)) &(5.9)\\ &\approx \sum_{j \in \mathcal{S}_i} W_{ij}\boldsymbol{f}_{ij}, &(5.10)\end{aligned}$$

where the one-dimensional flux in the $\tilde{\boldsymbol{w}} = [\tilde{w}_{ij}^{(1,0)}, \tilde{w}_{ij}^{(0,1)}]^T$ "direction" is

$$\boldsymbol{f}_{ij} = \tilde{w}_{ij}^{(1,0)}\mathbf{F}_1(\boldsymbol{q}_j) + \tilde{w}_{ij}^{(0,1)}\mathbf{F}_2(\boldsymbol{q}_j). \tag{5.11}$$

Instead of evaluating the flux tensor at the point neighbouring point $\boldsymbol{x}_j$, the flux is evaluated at the midpoint between the center point $\boldsymbol{x}_i$ and the neighbouring point $\boldsymbol{x}_j$, i.e.

$$\boldsymbol{x}_{ij} = \frac{1}{2}(\boldsymbol{x}_i + \boldsymbol{x}_j), \tag{5.12}$$

and the numerical flux is calculated based on reconstructed solutions Toro [1999] at the midpoint

$$\boldsymbol{f}_{ij} \approx \boldsymbol{f}(\boldsymbol{q}^-, \boldsymbol{q}^+) \tag{5.13}$$

where the $\boldsymbol{q}^-$ is reconstructed solution at the midpoint from the solution $\boldsymbol{q}_i$ and $\boldsymbol{q}^+$ is reconstructed solution at the midpoint from the solution $\boldsymbol{q}_j$. The reconstructed solutions are calculated using WLS approximation of local polynomial representations of the solutions. The flux at the midpoint is approximated by a numerical flux. The average of the reconstructed values gives the central flux

$$\boldsymbol{f}_{ij} \approx \frac{1}{2}(\boldsymbol{f}(\boldsymbol{q}^-) + \boldsymbol{f}(\boldsymbol{q}^+)). \tag{5.14}$$

The Rusanov flux, see Toro [1999], introduces numerical viscosity through the jump in the reconstructed values

$$\boldsymbol{f}_{ij} \approx \frac{1}{2}(\boldsymbol{f}(\boldsymbol{q}^-) + \boldsymbol{f}(\boldsymbol{q}^+)) + \frac{C}{2}(\boldsymbol{q}^- - \boldsymbol{q}^+), \tag{5.15}$$

where C is the local maximum propagation speed of the waves in the solution. The maximum propagation speed is found from the eigenvalues of the Jacobian of the plane-wave problem in the direction of the vector $\boldsymbol{w}$, see Leveque [2002]. The two Jacobian matrices are

$$\frac{\partial \boldsymbol{F}_1(\boldsymbol{q})}{\partial \boldsymbol{q}} = \begin{bmatrix} 2u_1 & 0 \\ u_2 & u_1 \end{bmatrix}, \quad \frac{\partial \boldsymbol{F}_2(\boldsymbol{q})}{\partial \boldsymbol{q}} = \begin{bmatrix} u_2 & u_1 \\ 0 & 2u_2 \end{bmatrix}, \tag{5.16}$$

and the Jacobian matrices in the direction of $\tilde{\boldsymbol{w}}$ is

$$\frac{\partial \boldsymbol{f}(\boldsymbol{q})}{\partial \boldsymbol{q}} = \tilde{w}_{ij}^{(1,0)} \frac{\partial \boldsymbol{F}_1(\boldsymbol{q})}{\partial \boldsymbol{q}} + \tilde{w}_{ij}^{(0,1)} \frac{\partial \boldsymbol{F}_2(\boldsymbol{q})}{\partial \boldsymbol{q}} \tag{5.17}$$

$$= \begin{bmatrix} \boldsymbol{u} \cdot \tilde{\boldsymbol{w}} + \tilde{w}_{ij}^{(1,0)} u_1 & \tilde{w}_{ij}^{(0,1)} u_1 \\ \tilde{w}_{ij}^{(1,0)} u_2 & \boldsymbol{u} \cdot \tilde{\boldsymbol{w}} + \tilde{w}_{ij}^{(0,1)} u_2 \end{bmatrix}, \tag{5.18}$$

who's two eigenvalues two eigenvalues are

$$\lambda_1 = \boldsymbol{u} \cdot \tilde{\boldsymbol{w}} - V, \quad \lambda_2 = \boldsymbol{u} \cdot \tilde{\boldsymbol{w}} + V, \tag{5.19}$$

where $V = \sqrt{\boldsymbol{u} \cdot \boldsymbol{u}}$ the flow velocity. In summary the method involves the following approximations:

1) Reconstruct solution of the solutions at the midpoint $\boldsymbol{x}_{ij}$.

2) Approximation of the numerical flux between the two points.

3) Approximation of the derivative at the point $\boldsymbol{x}_i$.

The following two examples gives the coefficients for simple one and two dimensional point distributions.

Example 5.1. *The 1D weighted least squares derivative operator for two points $x_{i-1/2}$ and $x_{i+1/2}$ in the distance $\Delta x/2$ to the left and right of x_i, with a first order Taylor expansions. In stencil notation the coefficients for the fist derivative are*

$$(D^1)_i = \left[-\frac{1}{\Delta x}, \ \frac{1}{\Delta x} \right], \tag{5.20}$$

and the corresponding coefficients for the approximate Riemann problem are

$$W_{i-1/2} = \frac{1}{\Delta x}, \quad W_{i+1/2} = \frac{1}{\Delta x}, \quad \tilde{w}^1_{i-1/2} = -1, \quad \tilde{w}^1_{i+1/2} = 1, \tag{5.21}$$

and the 1D derivative approximation is

$$(D^1 f_h)_i \approx \frac{1}{\Delta x}(f_{i+1/2} - f_{i-1/2}). \tag{5.22}$$

Example 5.2. *Consider a standard five point stencil in two dimensions, with* $\boldsymbol{x}_{i-1/2,j}$ *and* $\boldsymbol{x}_{i+1/2,j}$ *at a distance* $\Delta x/2$ *to the left and right of* $\boldsymbol{x}_{i,j}$ *and* $\boldsymbol{x}_{i,j-1/2}$ *and* $\boldsymbol{x}_{i,j+1/2}$ *at a distance* $\Delta y/2$ *to the below and above* $\boldsymbol{x}_{i,j}$*. The coefficients of the two first derivative approximations are*

$$(D^{(1,0)})_{i,j} = \left[-\frac{1}{\Delta x},\ 0,\ 0,\ \frac{1}{\Delta x}\right]. \tag{5.23}$$

and

$$(D^{(0,1)})_{i,j} = \left[0, -\frac{1}{\Delta y},\ \frac{1}{\Delta y}, 0\right]. \tag{5.24}$$

The weights for the 2D WLS-DQ divergence operation are

$$\begin{array}{cccc} W_{i-1/2,j} = \frac{1}{\Delta x}, & W_{i+1/2,j} = \frac{1}{\Delta x}, & W_{i,j-1/2} = \frac{1}{\Delta y}, & W_{i,j+1/2} = \frac{1}{\Delta y}, \\ \tilde{w}^{(1,0)}_{i-1/2,j} = -1, & \tilde{w}^{(1,0)}_{i+1/2,j} = 1, & \tilde{w}^{(1,0)}_{i,j-1/2} = 0, & \tilde{w}^{(1,0)}_{i,j+1/2} = 0, \\ \tilde{w}^{(0,1)}_{i-1/2,j} = 0, & \tilde{w}^{(0,1)}_{i+1/2,j} = 0, & \tilde{w}^{(0,1)}_{i,j-1/2} = -1, & \tilde{w}^{(0,1)}_{i,j+1/2} = 1, \end{array} \tag{5.25}$$

and the two derivative operations are

$$(D^{(1,0)} f_h)_{i,j} = \frac{1}{\Delta x}\left(f_{i+1/2,j} - f_{i-1/2,j}\right), \tag{5.26}$$

$$(D^{(0,1)} f_h)_{i,j} = \frac{1}{\Delta y}\left(f_{i,j+1/2} - f_{i,j-1/2}\right). \tag{5.27}$$

Chapter 6

Relaxation of the Dynamic Free Surface Boundary Condition Along Contact Lines

Modeling of free surface flow involves dynamic wetting and drying, the process by which a fluid spreads over the surface of a solid. The flow model can become singular at the contact point between the free surface and the solid. In the case of a creeping flow model it is singular due to the no-slip boundary condition on the wall, Huh and Scriven [1971]. The wall boundary condition is often replaced by a Navier-slip boundary condition to overcome this problem, Sprittles and Shikhmurzaev [2011]. The main difficulty in solving for the flow in the vicinity of a free surface and wall contact line is resolving the small physical scales and satisfying the free surface and the wall boundary conditions at the contact point simultaneously Sprittles and Shikhmurzaev [2011].

A problem in the mathematical formulation of the incompressible and inviscid ALE model has also been identified at the contact line. On the free surface the pressure is constant according to the dynamic boundary condition and there is no-flow through an impermeable wall. The problem arises when solving the Poisson equation for the pressure. The no-flow boundary condition is applied to the velocity at a Runge-Kutta stage

$$\boldsymbol{u} \cdot \boldsymbol{n} = 0, \quad \boldsymbol{x} \in \Gamma_{wl}. \tag{6.1}$$

which results in the inhomogeneous Neumann boundary condition for the pressure

$$\boldsymbol{n}_i \cdot (\nabla p_h^{(k-1)})_i = \frac{\rho}{J_i^{(k-1)} \beta_{kk} \Delta t} \boldsymbol{n}_i \cdot (J\boldsymbol{u})_i^{(k)*}, \quad \boldsymbol{x}_i \in \mathcal{P}_{\Gamma_{wl}}, \quad k = 1, \ldots, s. \tag{6.2}$$

But in the case where the free surface is normal to the wall, the zero pressure boundary condition corresponds to a homogeneous Neumann condition on the wall at the contact point

$$p = 0, \ \boldsymbol{x} \in \Gamma_{fs} \quad \Leftrightarrow \quad \boldsymbol{n} \cdot \nabla p = 0, \ \boldsymbol{x} \in \Gamma_{fs} \cap \Gamma_{wl}. \tag{6.3}$$

The physical model may become singular in the contact point. One possibility for resolving this problem is to replace this model with another model in the neighbourhood of the contact point. This approach has been applied in e.g. Chanson [2008] and Sprittles and Shikhmurzaev [2011]. Another approach is to relax the dynamic free surface boundary

condition along the contact line towards the contact point, where it matches the inhomogeneous Neumann condition for the pressure. This is carried out by substitution of the dynamic free surface boundary condition with the polynomial

$$p = p(s) = \sum_{\alpha=0}^{\alpha_{\max}} a_\alpha s^\alpha, \quad s \in \Gamma_{fs}, \tag{6.4}$$

where s is a parameter along the free surface. The coefficients of the polynomial are determined such that continuity is enforced, and the pressure satisfies the dynamic free surface condition at one end and the inhomogeneous Neumann boundary condition at the contact point

$$\left(\frac{\partial p}{\partial s}\right)_i = \boldsymbol{n}_i \cdot (\nabla p_h^{(k-1)})_i = \frac{\rho}{J_i^{(k-1)} \beta_{kk} \Delta t} \boldsymbol{n}_i \cdot (J\boldsymbol{u})_i^{(k)*},$$
$$\boldsymbol{x}_i \in \mathcal{P}_{\Gamma_{wl}} \cap \mathcal{P}_{\Gamma_{fs}}, \quad k = 1, \ldots, r. \tag{6.5}$$

where it is assumed that the parameter tangent to the free surface is parallel to the normal of the wall at the contact point. Specifically the relaxation polynomial is applied over a distance corresponding to 5 to 10 points on the free surface from the contact point.

Chapter 7

Representation and Approximation of the Fluid Domain

The fluid domain is $\Omega \in \mathbb{R}^d$ and its boundary is $\Gamma = \partial\Omega \in \mathbb{R}^{d-1}$. The boundary is divided into N_{bnd} segments

$$\Gamma = \bigcup_{i=1}^{N_{bnd}} \Gamma_i, \tag{7.1}$$

for which $\boldsymbol{x} \in C^1(\Gamma_i),\ i \in [1, \ldots, N_{bnd}]$. An example of a fluid domain is seen in figure 7.1

Fluid Boundary

Each fluid boundary segment has a data structure with information about its geometrical and physical properties and they are connected in a doubly-connected linked list as described in de Berg et al. [2008]. The most important fields in the data structure are the boundary type and information about the outward normal vector to the boundary. The basic data structure is

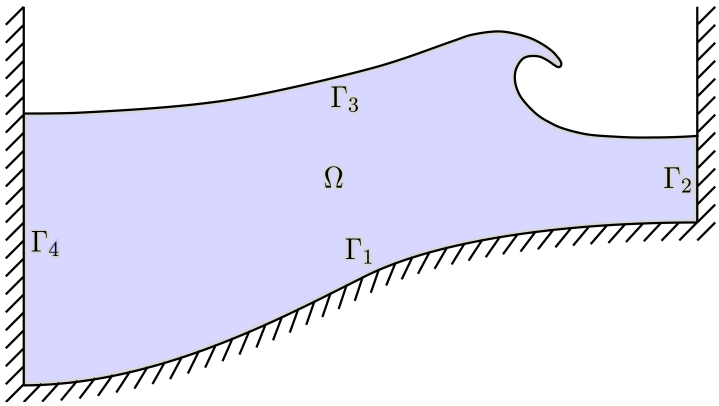

Figure 7.1: An example of a fluid domain embedded in a solid boundary.

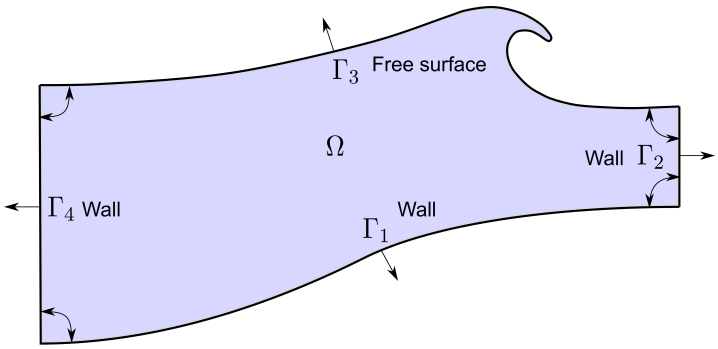

Figure 7.2: An example of the fields in the boundary data structure. The type of boundary is either "wall" or "free surface", the outward pointing arrows are the normal boundary normal vectors and pointer in the doubly connected linked list is the bi-directed arrows in the corner between the boundary segments.

`type`	The boundary segment type: 1) Wall boundary, 2) Free surface boundary.
`normal`	The normal vector to the boundary.
`next`	The index of the next boundary in the doubly connected linked list.
`prev`	The index of the previous boundary in the doubly connected linked list.

Due the arbritrary geometry of the indivitual boundary segment the data structure also needs additional fields with information about the normal vector of the boundary. These field are for example center and radius of a circular boundary segment and the function to evaluate the normal from these parameteres. In particular this boundary data structure is used to implement the boundary conditions in the GFPM method. An example of a fluid domain is seen in figure 7.2.

Solid Boundary

The fluid domain is surrounded by a solid boundary, but the boundary of the fluid is not nessesarily the same as the boundary of the solid. If the fluid has a free surface then the solid boundary will reach beyond the fluid boundary as seen in figure 7.1. The solid boundary is $\Gamma_{solid} \in \mathbb{R}^{d-1}$ and an example is seen in figure 7.3. The solid boundary doesn't need to be a closed boundary.

7.1 Numerical Approximation of the Fluid Domain

A set of N points are distributed over the physical domain Ω

$$\mathcal{P} = \{\boldsymbol{x}_i : i = 1, \ldots, N \wedge \boldsymbol{x}_i \in \Omega\}. \tag{7.2}$$

The points are distributed in the interior of the fluid domain $\Omega \setminus \Gamma$, on the boundary Γ, and one point at each singular point on the fluid boundary, i.e. at the intersections

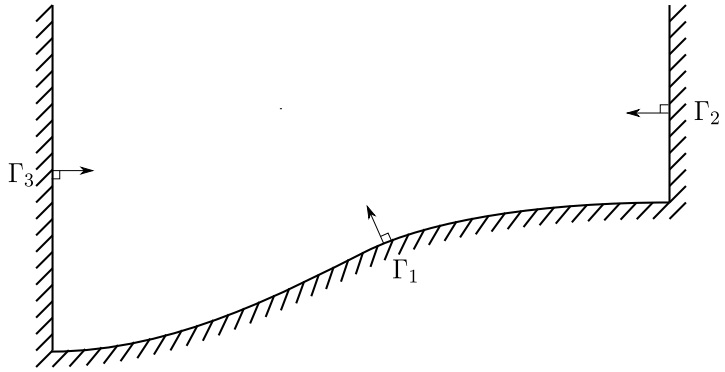

Figure 7.3: The solid boundary with the normal vectors pointing outward from the solid.

between the boundary segments $\Gamma_i,\ i = 1, \ldots, N_{bnd}$. The points are used as vertices in a triangular mesh which serves as an approximation of the physical domain

$$\Omega \approx \Omega_h = \mathcal{T}(\mathcal{P}) = \bigcup_{i=1}^{N_T} T_i. \tag{7.3}$$

where T_i is a triangle, with straight or curved boundaries. A straight sided triangle gives a first order (linear) approximation of the fluid domain and curved boundaries are required for second or higher order approximation of the fluid domain. The purpose of the triangular mesh is two fold: First it serves as an approximation of the fluid domain, secondly it is a data structure for the connectivity between the points in the fluid domain. When the triangular mesh is used as a data structure then the linear approximation is sufficient and it is convenient to represent the mesh as a graph $G = G(\mathcal{P}, E)$ where E are edges that connect the points/vertices.

The triangular mesh $\mathcal{T}$ and its corresonding graph G is constructed from the point set $\mathcal{P}$. The main complications in this procedure are that the fluid domain Ω can be non-convex, it can have holes, it evolves in time and it can change topology. In other words it has a complicated evolving geometry. The triangular mesh is constructed in the following way: First a Delaunay triangulation is made from the points $\mathcal{P}$. Due to the definition of a triangulation, see de Berg et al. [2008], this is a convex hull and all the triangles that are outside the fluid domain are to be removed. Before these triangles can be removed, we need to make sure that the edges of the triangulation do not intersect the boundary of the fluid domain Γ. Therefore the second step is to find all the edges that intersect the fluid boundary and make an edge flip operation, see de Berg et al. [2008], on these edges. The resultant triangulation with respect to the boundary of the fluid domain, hence the intersection between the fluid boundary and the edges in the graph G is empty $\Gamma \cap E = \emptyset$. The third step is to remove all the edges outside the fluid domain from the graph G. The total operation of making the triangular mesh from the Delaunay triangulation is summarized in the algorithm 1. The input to the algorithm are the vertices vtx, i.e. the points in the fluid domain $\mathcal{P}$, and the boundary data structure bnd and it returns the triangular mesh tri_to_vtx and the corresponding graph as a vertex to vertex list vtx_to_vtx.

An example of the construction of the triangular mesh is seen in the plots in figure 7.4. The fluid domain in this example consists of two separated subdomains: The lower

Algorithm 1 Triangular mesh approximation of the fluid domain.

Require: *vtx* and *bnd*
  tri_to_vtx ← Triangulation(*vtx*)
  Make edge to vertex list *edge_to_vtx* from *tri_to_vtx*
  Make edge to triangle list *edge_to_tri* from *edge_to_vtx* and *tri_to_vtx*
  for $ibnd = 1 \rightarrow |bnd|$ **do**
    Find the edges in the triangulation intersecting between the fluid boundary edges
    Flip the intersecting edges, in *edge_to_vtx* and *tri_to_vtx* via *edge_to_tri*
  end for
  Update the list *edge_to_tri*
  Remove the edges that are outside the fluid domain from *edge_to_vtx* and *tri_to_vtx* via *edge_to_tri*
  Make the vertex to vertex list *vtx_to_vtx* from *edge_to_vtx*
  return *tri_to_vtx* and *vtx_to_vtx*

domain resembles a wave sloshing in a tank and the upper one is an elliptical drop of water falling into the tank. The two fluid domains are disconnected and they need to remain disconnected in the numerical approximation. Initially the point set is created with the points lying inside the two subdomains and a boundary data structure is created with the five boundary segments. Then the triangulation is made based on the point set and, as seen in figure 7.4 b, this is a convex hull. Some of the edges in the triangulation intersect the boundary edges, these edges are flipped and now the triangles in the triangulation respect the boundaries. Finally all the edges outside the fluid domain are removed, and the remaining triangular mesh is a linear approximation of the fluid domain. This example is with two separate subdomain and it would also be reasonable to perform the triangulation on each subdomain, but in the present algorithm the triangulation is carried out over the total domain. With overturning waves and cavities in the fluid domain the edge flip is also required for a single domain.

Breadth First Search Stencils

The triangular mesh is used as a data structure for searching for computational stencils. The stencil of a point $\boldsymbol{x}_i$ is a set of points in its neighbourhood, and the actual point set depends on the search method used to find the point set. Figure 7.5 shows different types of stencils. The first is a finite difference stencil where the data structure is a structured mesh and the stencil is a number of points in each direction along the mesh lines from the center point. The second point set has no data structure and the stencil is the points within a radius of the center point. The third point set has no data stucture and the stencil is a specified number of nearest neighbours. The data structure on the fourth point set is a triangular mesh and the the stencil is found using a BFS. This method resembles the finite difference stencil in the way it respects the connectivity of the domain and it searches in levels around the center point. For each point in the point set $\mathcal{P}$ a stencil is found using BFS in the triangular mesh approximation of the fluid domain. The algorithm for the BFS is seen in algrithm 2. The BFS takes as input the graph $G = (\mathcal{P}, E)$, in form of an adjacency-list, a query vertex in the graph q and the number of points in the stencil $N_{\mathcal{S}}$ and it returns the first $N_{\mathcal{S}}$ discovered vertices. The

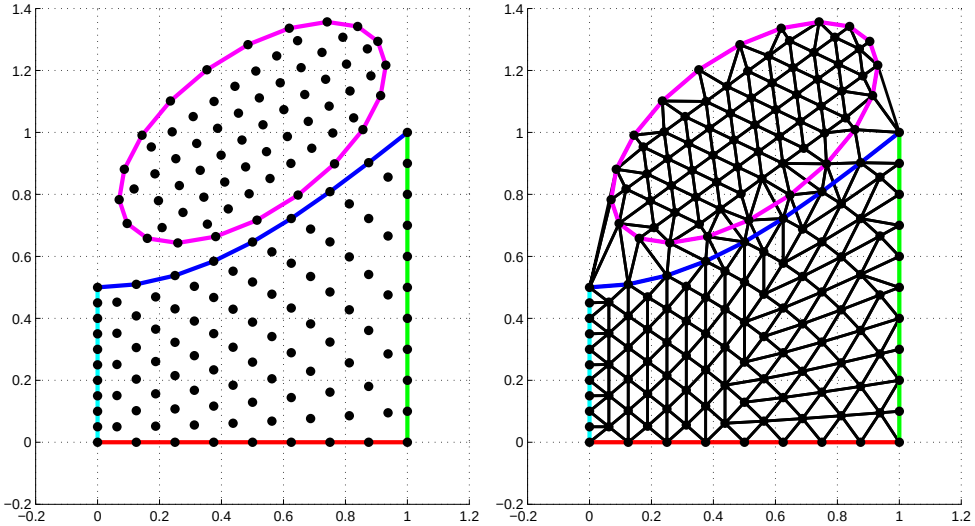

(a) Points and boundaries

(b) After triangulation

(c) After edge flip

(d) After edge remove

Figure 7.4: The construction of a fluid domain conforming non-convex triangular mesh.

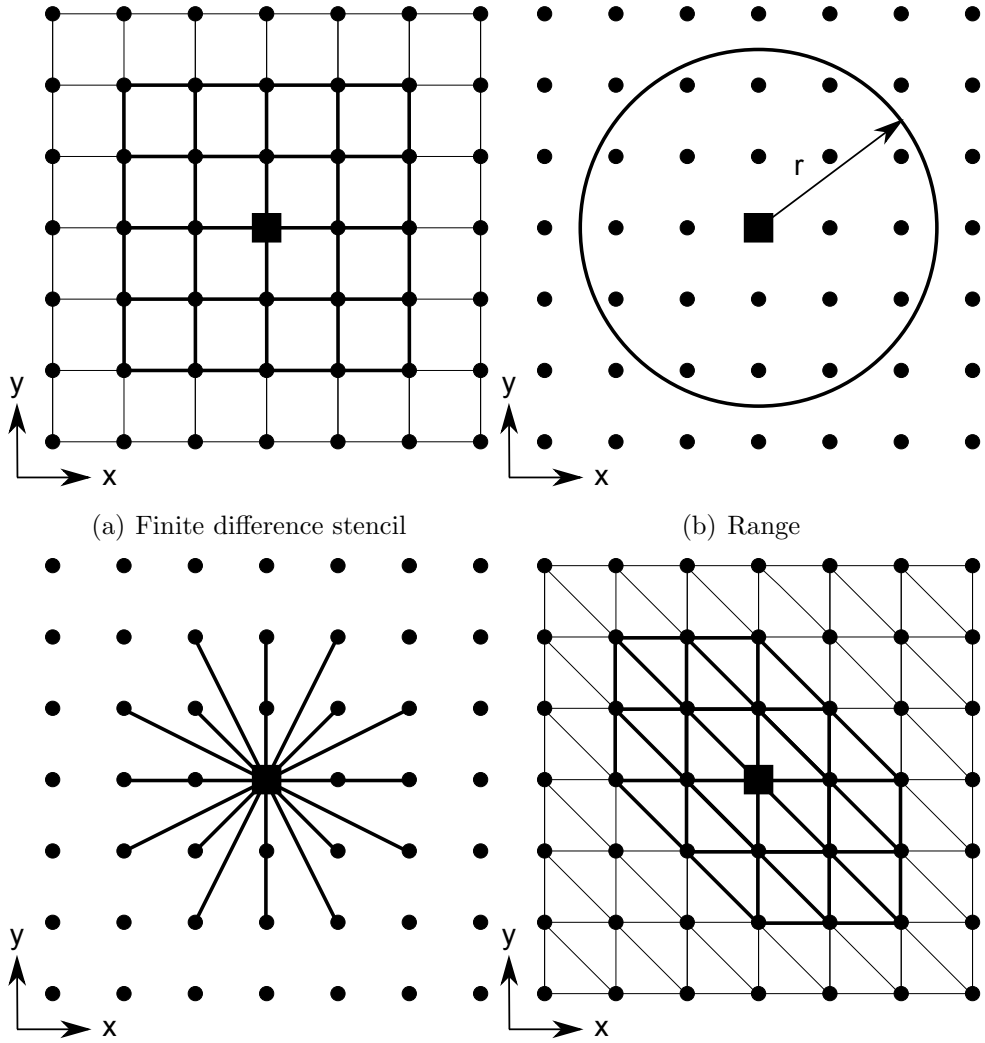

(a) Finite difference stencil

(b) Range

(c) kNN

(d) BFS

Figure 7.5: The figures illustrates the finite difference stencil, a range search, a k nearest neighbour search and a breath first search.

search algorithm uses a first-in, first-out queue Q to store the vertices that have been discovered and to get the adjacent vertices of the discovered vertices. The BFS algorithm 2 is similar to a standard BFS algorithm, e.g. as presented in Cormen et al. [2009], which returns the whole BFS tree instead of the first N_S discovered vertices.

Algorithm 2 The breadth first search algorithm finding the first k vertices closest to the query vertex q in the graph $G = (V, E)$.

Require: G, q and k
  for $u \in V \setminus q$ **do**
    $discovered[u] \leftarrow 0$
  end for
  $discovered[q] \leftarrow 1$
  `enqueue`(Q,q)
  $count \leftarrow 0$
  while $Q \neq \emptyset \ \wedge \ count < k$ **do**
    $u \leftarrow$ `dequeue`(Q)
    for all v adjencent to u **do**
      if $discovered[v] = 0$ **then**
        $discovered[v] \leftarrow 1$
        `enqueue`(Q, v)
        $stencil[count] \leftarrow v$
        $count \leftarrow count + 1$
      end if
    end for
  end while

Topology Changes in the Fluid Domain

As the fluid domain $\Omega(t)$ evolves it can change topology. Two examples of typical topology changes are given in figure 7.6, where an advancing front hits a wall and makes a plunging wave in the return flow. Initially the wave front is advancing towards the wall, and the fluid domain Ω has two boundary segments, Γ_1 next to the bottom and the free surface boundary segment Γ_2. As the wave front hits the wall, a new boundary segment Γ_3 is added to the fluid domain. Later an overturning wave is generated and as it plunges into the wave trough and a cavity is formed. The new free surface inside this cavity is boundary segment Γ_4. The fluid domain Ω is approximated by a triangular mesh Ω_h which is generated based on a set of points P as described above. The mesh points are Lagrangian, i.e. they move along streamlines in the flow, and the mesh evolves and deforms with the flow. The nature of the Lagrangian points makes the numerical approximation of the fluid domain simple as long as its topology is fixed, but when the topology of the fluid domain changes it becomes more complicated. The algorithm 3 is a bisection iteration method that approximates the time of intersection between fluid boundary segments and between the fluid boundary and solid boundary. Then the time of intersection is determined to the accuracy of the iteration method, the topology of the fluid domain and its boundaries are updated. The possible topology updates are

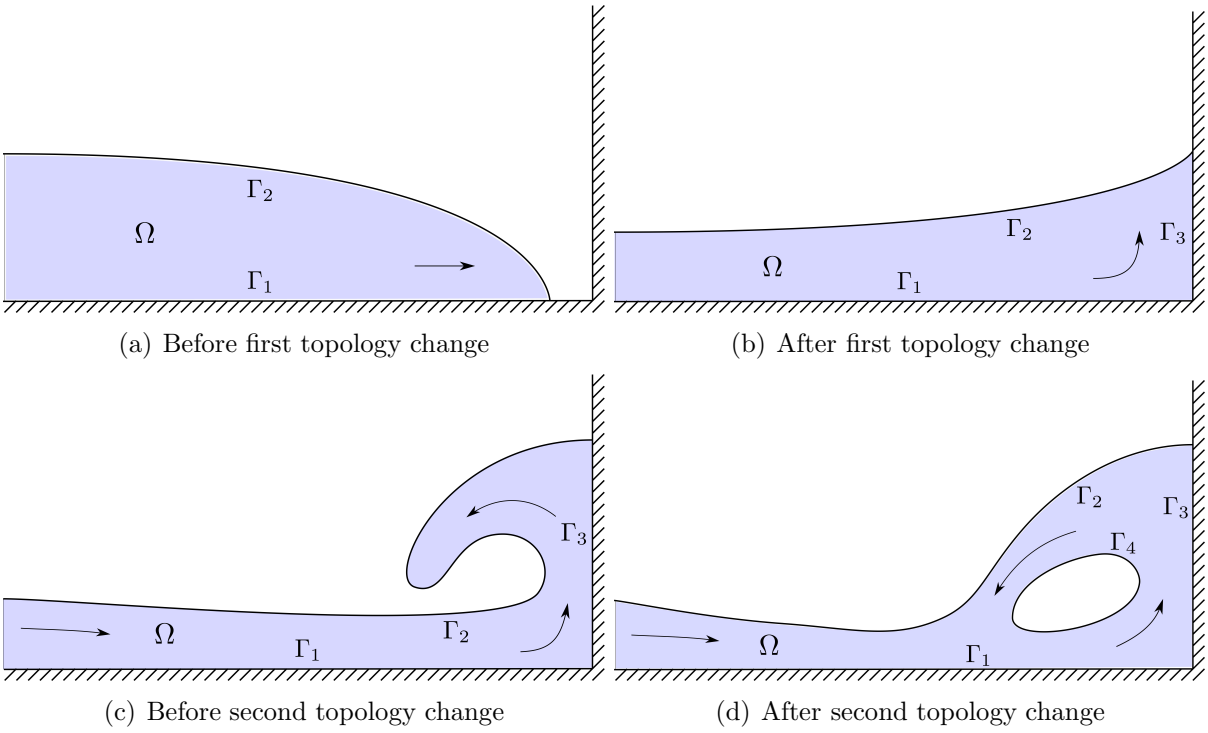

(a) Before first topology change

(b) After first topology change

(c) Before second topology change

(d) After second topology change

Figure 7.6: The two main topology changes when a wave front impacts on a wall. First the fluid boundary segment Γ_3 is added to the fluid domain as the wave front hits the vertical wall and as the overturning wave plunges into the wave trough, a cavity is formed and a new free surface boundary segment Γ_4 is added to the fluid domain.

- `insert` a new boundary segment.

- `remove` a boundary segment.

- `connect` boundary segments.

- `split` a boundary segment.

Using these operations the boundary segments can updated due to the topology changes of the fluid domain.

Algorithm 3 Approximation of the time of intersection via bisection iteration of the timestep.

Require: Γ_{wall}, Δt, $iter_{max}$ and tol
  $\Delta t_{min} \leftarrow 0$
  $\Delta t_{max} \leftarrow \Delta t$
  $iter \leftarrow 0$
  $intersection \leftarrow false$
  while $iter < iter_{max} \wedge res < tol$ **do**
    Calculate $\Gamma(t + \Delta t)$
    if $\sim intersection \wedge (\Gamma(t + \Delta t) \cup \Gamma(t + \Delta t) \neq \emptyset \vee \Gamma(t + \Delta t) \cup \Gamma_{wall} \neq \emptyset)$ **then**
      $intersection \leftarrow true$
    end if
    if $intersection$ **then**
      Calculate signed distance $dist$
      if $dist < 0$ **then**
        $\Delta t_{max} \leftarrow \Delta t$
      else if $dist > 0$ **then**
        $\Delta t_{min} \leftarrow \Delta t$
      end if
    end if
    $\Delta t \leftarrow \frac{1}{2}(\Delta t_{min} + \Delta t_{max})$
    $res \leftarrow dist$
    $iter \leftarrow iter + 1$
  end while

7.2 Refinement and Coarsening of the Point Set

Before each Runge-Kutta time step the point set is locally refined and coarsened to ensure good conditioning of the WLS matrices and a well-posed point set. For the definition of a well-posed (or unisolvent) point set see Wendland [2005]. Poorly-posed point distributions can result from the Lagrangian movement of the points, i.e. points can move too close or too far apart, and develop into thin structures in the flow, e.g. in sprays or thin layers close to walls.

The refinement and coarsening operations are carried out according to a set of adaptivity rules very similar to the ones presented in Iske [2004]. For a point point $\boldsymbol{x}$ in a set

of points $\mathcal{P}$, an error indicator $E(\boldsymbol{x})$ gives an estimate of the approximation quality at this point. The point is refined if the error estimator is below the lower bound

$$E(\boldsymbol{x}) > c_{refine} \max(E(\mathcal{P})), \tag{7.4}$$

where $c_{refine} \in [0, 1]$ and a point is coarsened if the error indicator is above a the upper bound

$$E(\boldsymbol{x}) < c_{coarse} \max(E(\mathcal{P})), \tag{7.5}$$

and $c_{coarse} < c_{refine} \in [0, 1]$. The coarsening operation removes a point from the point set $\mathcal{P} = \mathcal{P} \setminus \boldsymbol{x}$ and the refinement operation inserts a new set of points in the point set $\mathcal{P} = \mathcal{P} \cup \mathcal{P}_{new}$. The canditates for the new points are the barycenters of the triangles coming from the triangular mesh $\mathcal{T}(\mathcal{P})$.

A simple geometric error indicator is based on the fill distance, see Wendland [2005],

$$E(\mathcal{P}) = h_{\mathcal{P},\Omega} = \max_{\boldsymbol{y}\in\Omega} \min_{\boldsymbol{x}_i\in\mathcal{P}} ||\boldsymbol{y} - \boldsymbol{x}_i||_2, \tag{7.6}$$

and the local fill distance:

$$E(\boldsymbol{x}) = h_{\mathcal{P},B_r}(\boldsymbol{x}) = \max_{\boldsymbol{y}\in B_r(\boldsymbol{x})} \min_{\boldsymbol{x}_i\in\mathcal{P}} ||\boldsymbol{y} - \boldsymbol{x}_i||_2. \tag{7.7}$$

The fill distance adaption tends to give a uniform distribution of the point set and a the following parameters are used i this project

$$c_{refine} = 0.6, \quad \boldsymbol{x} \in \Omega \setminus \Gamma, \tag{7.8}$$
$$c_{refine} = 0.55, \quad \boldsymbol{x} \in \Gamma, \tag{7.9}$$
$$c_{coarse} = 0.3, \quad \boldsymbol{x} \in \Omega. \tag{7.10}$$

When a new point has been created the required fluid properties are approximated at this point using the WLS method presented in section 4.2. It is very difficult to make a good choice of the adaptivity parameters. Bad choices can result in the removal of too many points or the insertion of too many points. This method has been applied in a heuristic way and the choice of parameters above is based on experience.

7.3 Point Position Filtering

A point position filtering process is applied to increase the robustness of the WLS approximations. The last step in the time step preprocess is point position filtering. The point positions are smoothed using a Laplacian filter, according to Taubin [1995],

$$\boldsymbol{x}_i = \boldsymbol{x}_i + \frac{\lambda}{|\mathcal{S}_i|} \sum_{j\in\mathcal{S}_i} (\boldsymbol{x}_j - \boldsymbol{x}_i) \tag{7.11}$$

and the fluid variables are approximated at the new points by the WLS approximation.

Chapter 8

Applications to Free Surface Validation Tests

The physical model and its numerical approximation are subject to validation studies in this chapter. The area of application is free surface flow and three standard benchmark tests are used to assess the numerical model. These are the deforming elliptical drop, see e.g. Ferrari et al. [2009], small amplitude standing waves and a dam break, see Zhou et al. [1999].

There are many cases that are also relevant to free surface flow and in particular free surface flow with large deformations of the free surface. These are among others: Mildly nonlinear standing waves, Engsig-Karup [2006], strongly non-linear solitary wave reflection Madsen et al. [2002] and solitary wave breaking in deep water, Kway et al. [1998] and in shallow water, Ting and Kirby [1996].

8.1 Deforming Elliptical Drop

The deforming elliptical drop is a classical test case for free surface flow models. It was proposed by Monaghan [1994] for validation of a SPH method. Later it has been applied by Ellero et al. [2007] and Ferrari et al. [2009] among others, also for validation of SPH methods. Recently Dumbser [2011] used it for validation of a two-phase compressible flow model with volume of fluid (VOF) type interface capturing and finite volume type solution representation and equation approximation.

The initial condition for the fluid domain $\Omega(0)$ is a circular drop with radius $R = 1\text{m}$ and center in $\boldsymbol{x}_0 = [0, 0]^T$. The initial condition for the velocity is a linear function of x and y

$$\boldsymbol{u}(\boldsymbol{x}) = \begin{bmatrix} -100.0x \\ 100.0y \end{bmatrix}, \quad \boldsymbol{x} \in \Omega(0), \tag{8.1}$$

The fluid domain $\Omega(t)$ evolves in time to a ellipse with radii a and b. For an incompressible flow the product of $\omega = ab$ remains constant and the temporal evolution of the radius a

is described by the two coupled ordinary differential equations Monaghan [1994]

$$\frac{dA}{dt} = \frac{A^2(a^4 - \omega^4)}{a^4 + \omega^4}, \tag{8.2}$$

$$\frac{da}{dt} = -aA. \tag{8.3}$$

These equations are solved numerically using a RK45 method with the initial condition

$$a = R, \quad t = 0, \tag{8.4}$$

$$\begin{aligned} A &= -a\frac{da}{dt} \\ &= -R \cdot u(R, 0), \quad t = 0, \end{aligned} \tag{8.5}$$

in the time interval $t \in [0, 0.0076]$, the same time interval used for the deforming elliptical drop calculation in Ferrari et al. [2009].

The initial point distribution consists of hexagonal lattice in the interior of the fluid domain and uniformly distributed points on the free surface boundary. Four different cases with initially $N(0) = 934$, $N(0) = 2000$, $N(0) = 3634$ and $N(0) = 7614$ points have been run. The points are refined, coarsened and smoothed with the Laplacian filter before each time step.

Figure 8.1 shows the initial the time evolution of the smallest case $N(0) = 934$. It is presented to give an impression of the way the points evolve during the calculation. The points move with the fluid during the Runge-Kutta time steps and are refined, coarsened and smoothed between the Runge-Kutta steps. First of all it is seen that the final solution compares reasonably well with the analytical solution. At the upper and lower ends, where the curvature of the surface is high, the computed free surface is too smooth. This is due to the Rusanov flux and the smoothing of the point distribution, and most of all due to the very coarse resolution in this figure.

The next figure 8.2 shows the pressure final state of the four simulations. The computed free surface seems to approximated the analytical solution better as the resolution is increased. It is clear the the pressure is a nice and smooth solution, which is not trivial Ferrari et al. [2009].

The figures in 8.3 shows the error evolution in the radii of the ellipse. The numerical approximation is mostly convergent and the deviations are not well understood nor thorough analyzed. But in general the errors are small and acceptable for engineering accuracy.

Figure 8.4 shows the evolution in the fluid volume and the number of points. The errors in the computed fluid volume is less than around 1% in all cases. The number of points in the calculation increases very much (up to 35%) for one of the calculations, but less than 10% for the three other simulations.

The convergence of the calculated free surface position are seen in figure 8.5 for 2nd and 4th order approximations. The length scale for the convergence test is the global fill distance and the error metric is the infinity norm of the error in the radius of the ellipse. It is seen that the 4th order approximation converges faster than the 2nd order approximation for the more coarse point distributions, but none of the convergence rates match the theoretical rates.

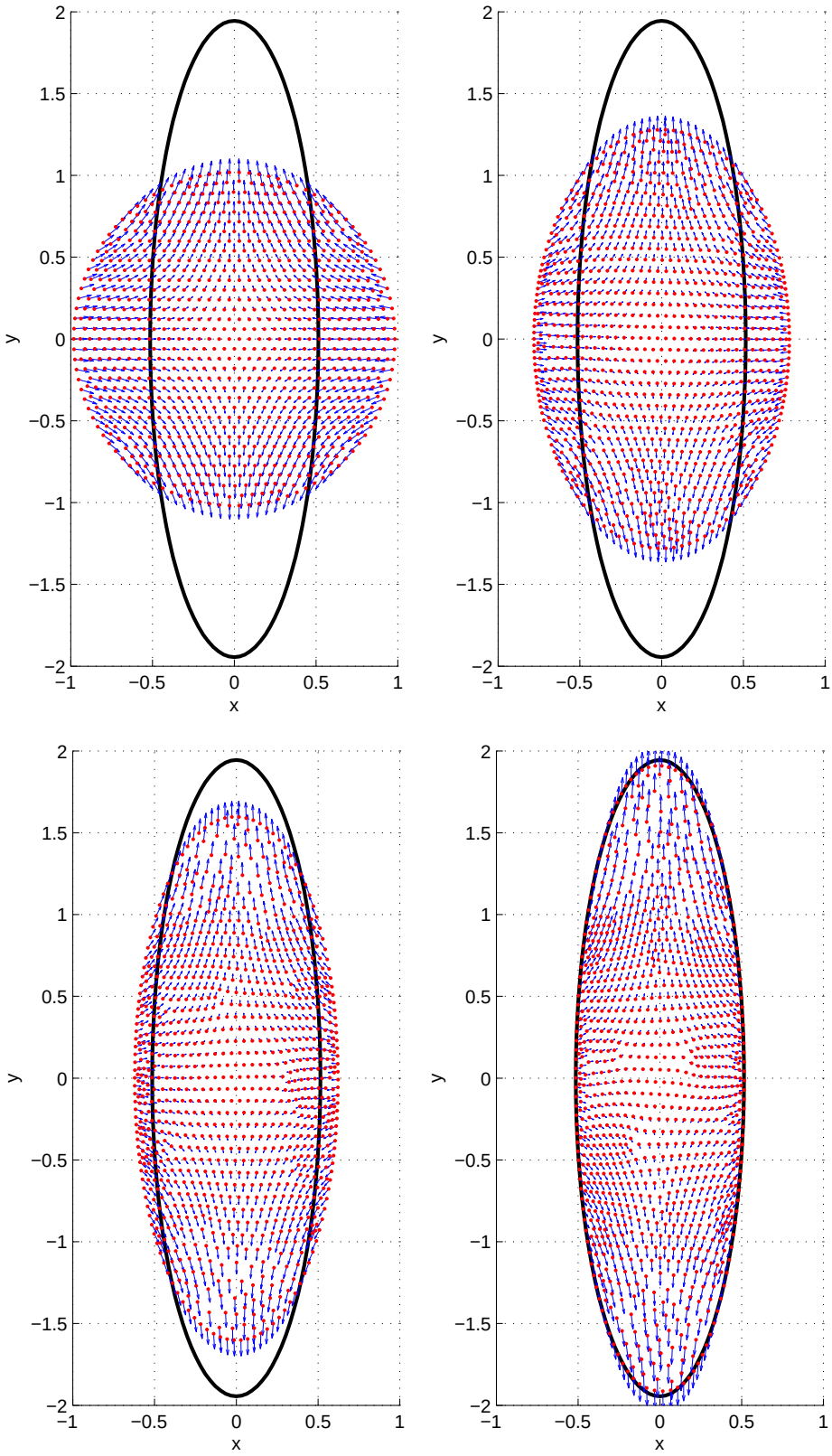

Figure 8.1: Point distributions and velocity fields in a elliptical drop calculation. The black line is the final free surface according the analytical solution. The initial number of points is $N(0) = 934$ and the figures show the solution at time $t/t_{final} = \{0, 1/3, 2/3, 1\}$

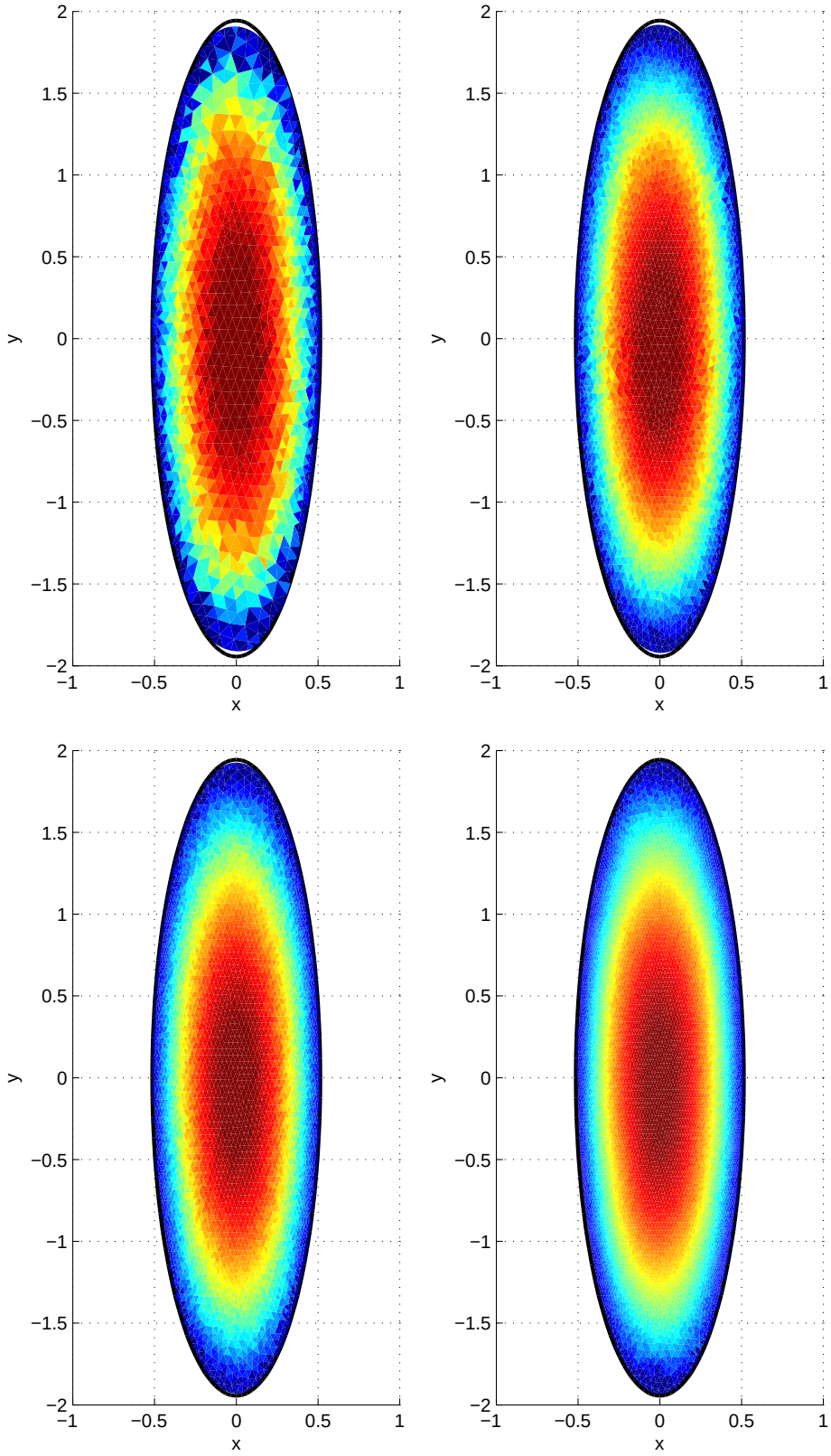

Figure 8.2: The final, $t = 0.0076$, physical domain and pressure distribution four cases with the following number of points in the initial condition $N(0) = 934$, $N(0) = 2000$, $N(0) = 3478$ and $N(0) = 7614$. The black line shows the theoretical free surface position at the final time. Dark blue is low pressure and dark red is high pressure.

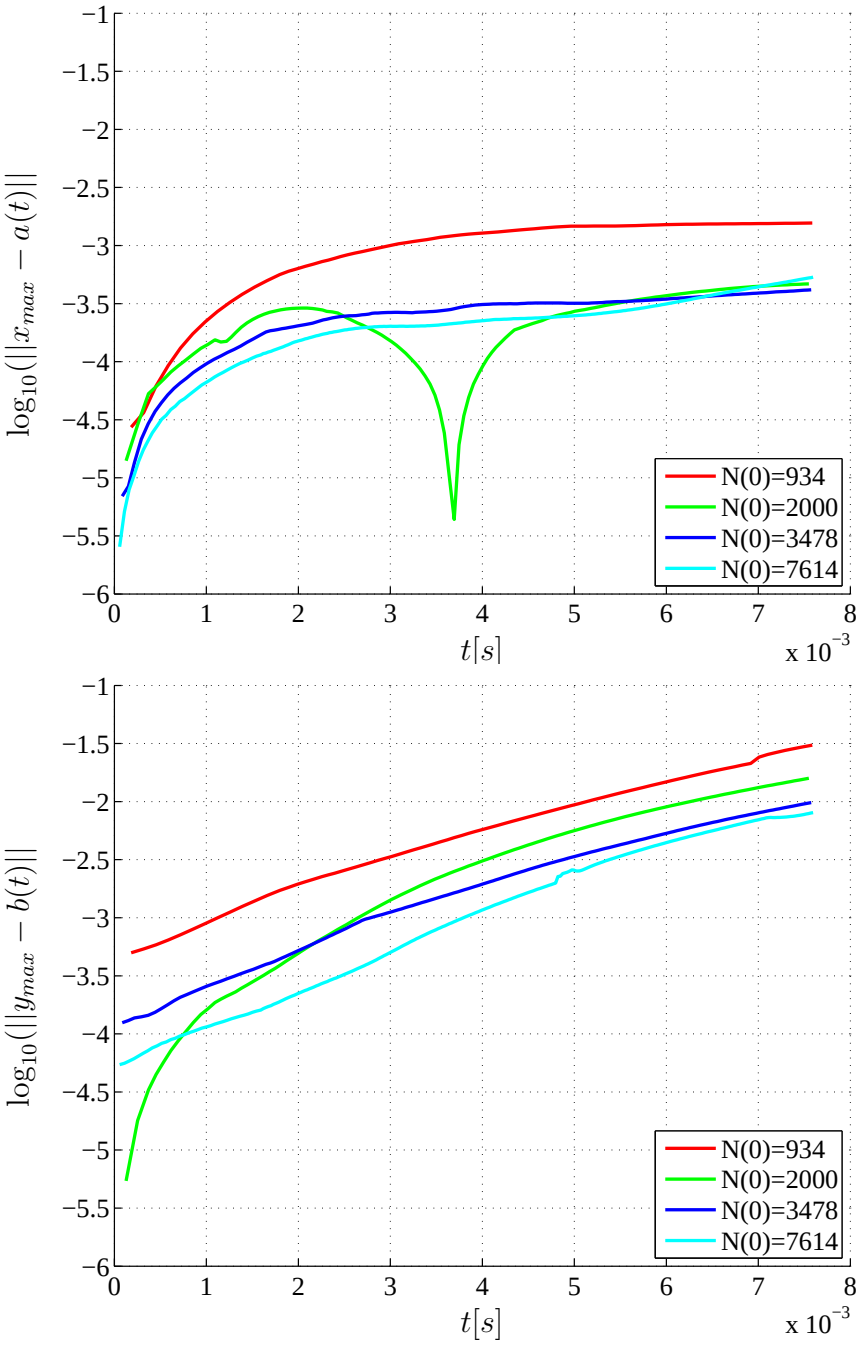

Figure 8.3: The maximum error of the elliptical drop deformation.

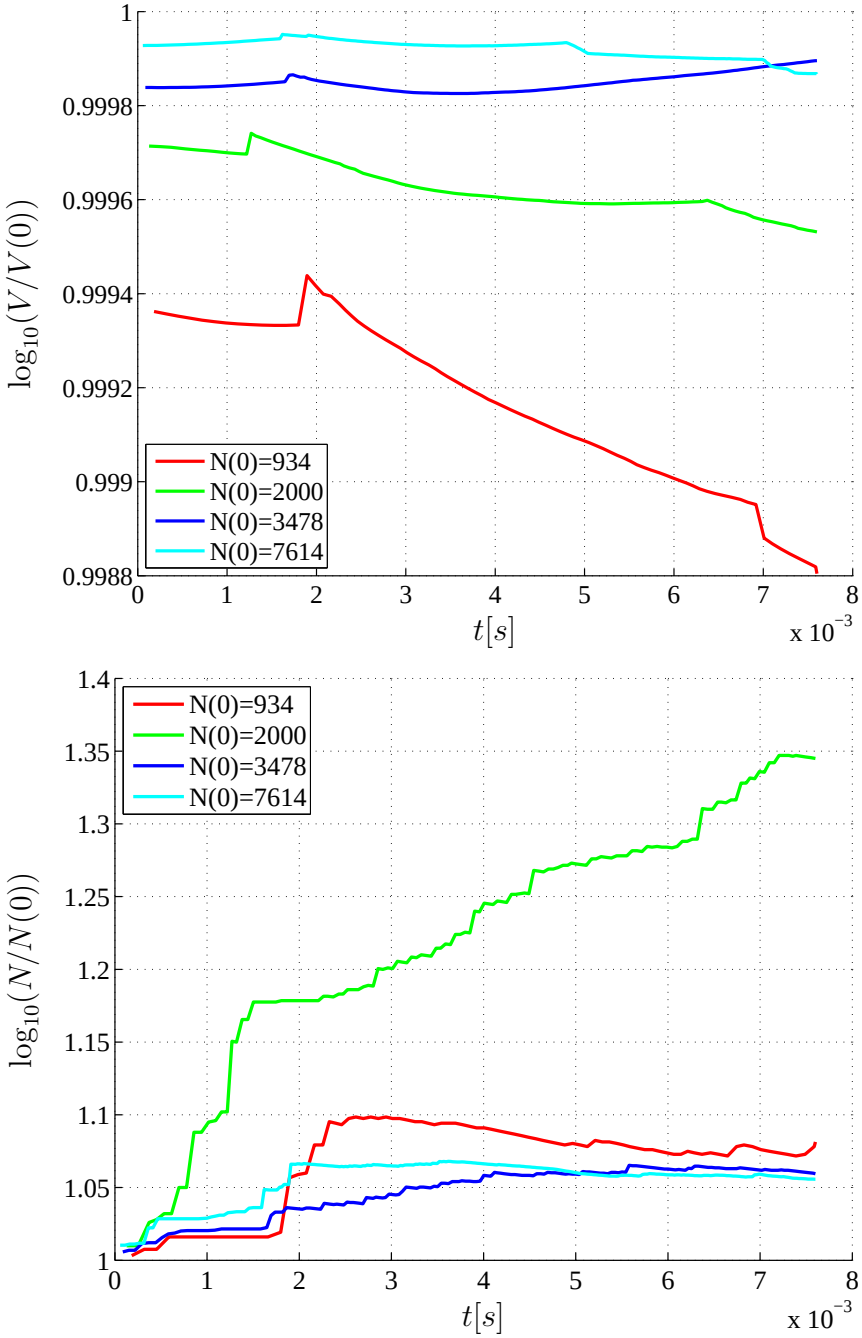

Figure 8.4: The evolution of the relative volume and the evolution in the relative number of points.

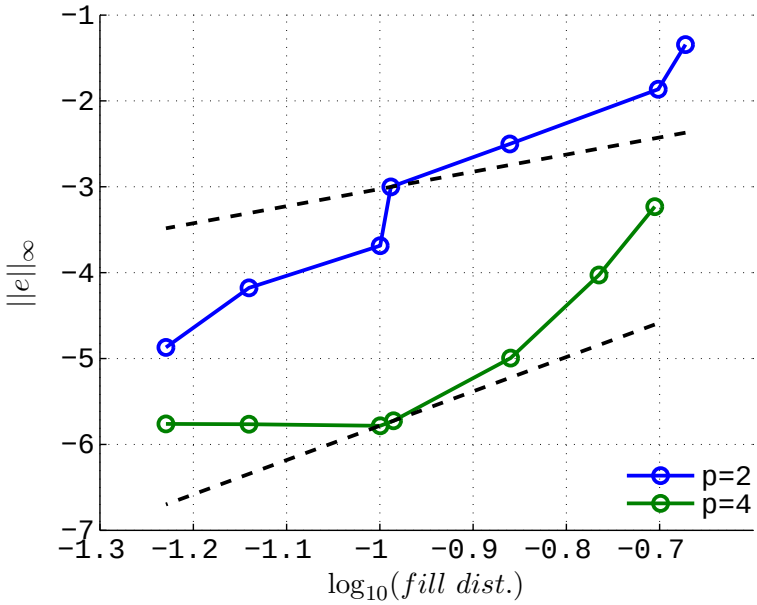

Figure 8.5: The convergence in the radius of the ellipse for 2nd and 4th order approximations.

8.2 Small Amplitude Waves

This test case considers modelling of a small amplitude wave in two spatial dimensions. The parameters for the initial condition are non-dimensional wave number $kh = \pi$ and wave steepness $H/L = 0.001$, where $k = 2\pi/L$ is the wave number, L is the wave length, H is the wave height and h is the water depth from the still water level. The initial free surface elevation at time $t/T = 0$ is

$$\eta(x) = H\cos(kx), \quad 0 \leq x \leq L. \tag{8.6}$$

The wave period T is calculated according to linear theory $T = 2\pi/\sqrt{gk}$, where $g = 9.81\text{m/s}^2$ is the gravitational acceleration.

The initial condition is given by the free surface solution and the zero velocity field

$$\mathbf{u}(\mathbf{x}, 0) = \mathbf{0}, \quad \mathbf{x} \in \Omega = [0, 1] \times [-h, \eta(x, 0)]. \tag{8.7}$$

The calculations are validated by the wave frequency and wave amplitude.

A sketch of the initial condition is seen in figure 8.6 together two other figures: One showing the point distribution and velocity vectors after one time step and one with the pressure after one time step. The two latter have $N(0) = 1172$ points in the initial condition and the initial point distribution is a hexagonal lattice.

The calculations has been run for 8 wave periods and the surface elevations at $x/L = 0$ (left) and $x/L = 1/2$ (right) are seen in figure 8.7 for 3 different resolutions. It is hard to see any difference between the calculations. The evolution in the volume of the fluid domain and the number of points in the simulation are also seen in 8.7. It is seen that the space conservation error is very small and decreasing for increasing number of points. The point adaptivity and smoothing adjust the initial point configuration within the first wave period and thereafter the number of points stays constant. This is a good behavior for the point adaptivity method when the fluid domain deformations are very small as in this case.

An error analysis based on the time history of the free surface elevation at the boundary walls are seen in figure 8.2. It is seen that the free surface elevations are more accurate for an increased number of points.

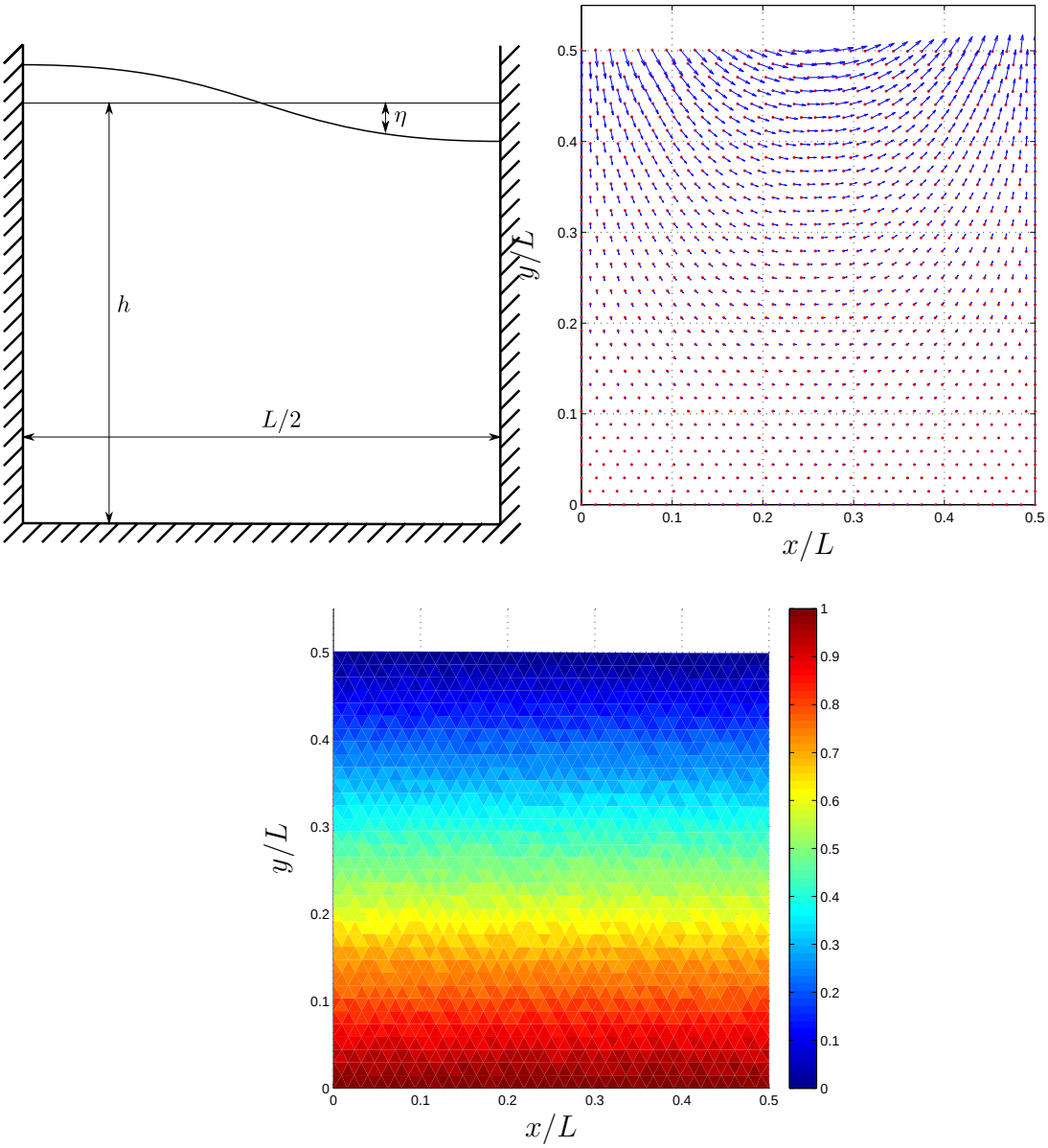

Figure 8.6: A sketch of the initial condition in the standing wave case and the initial the point distribution, velocity field and pressure. The color scale show the dimensionless pressure $p/(\rho g H)$.

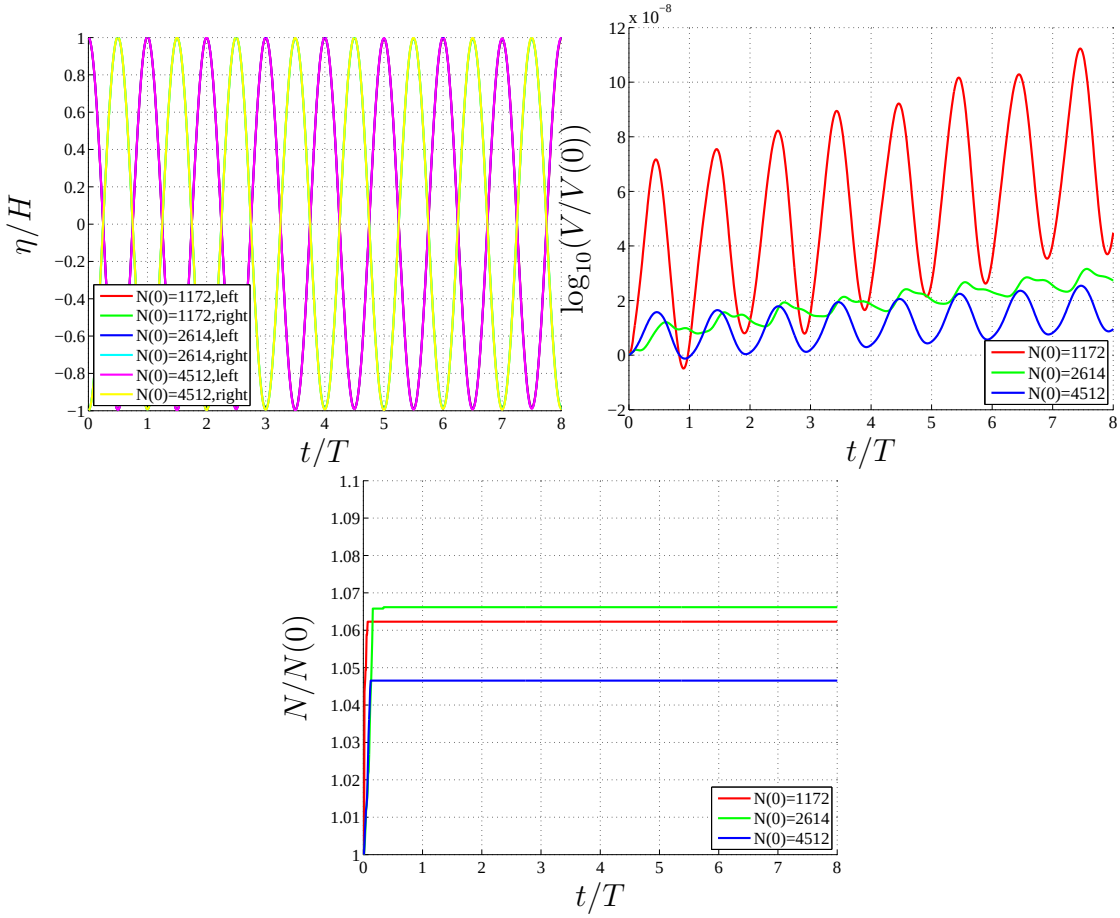

Figure 8.7: The free surface elevation on the left and right boundaries and the evolution in the fluid volume and the number of points.

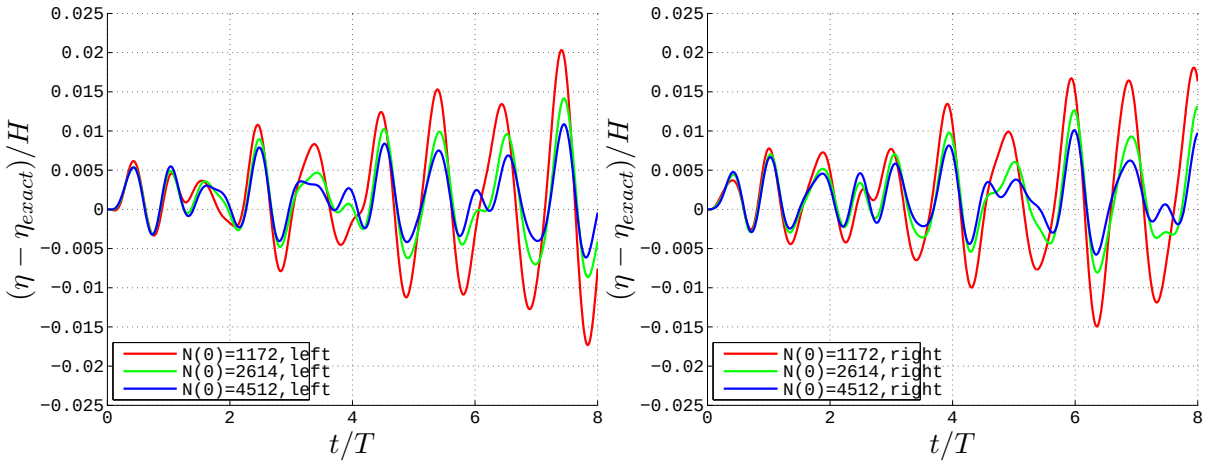

Figure 8.8: The errors of the free surface position at the left and right walls.

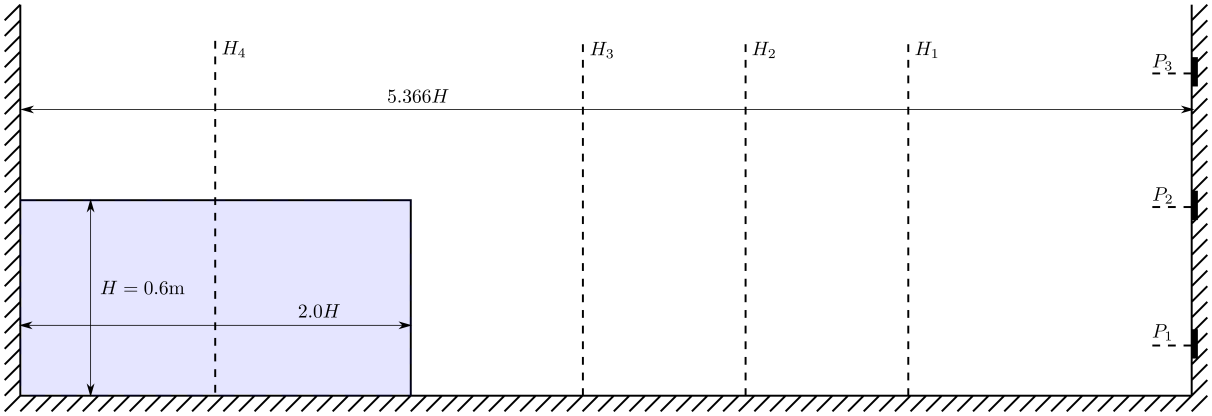

Figure 8.9: A sketch of the dam break experiment.

8.3 Dam Break

The dam break test case involves several physical phenomena: Propagation of a wetting front, wall impact, overturning waves and development of a complex free surface. Here the two dimensional dam-break is presented. A sketch of the initial condition for the dam break test is seen on figure 8.9. Initially the water is stored in a rectangular dam with the dimensions: Depth $H = 0.6$m and length $L = 2.0H = 1.2$m. The sluice gate is opened at the initial time $t = 0.0$s and the water will flow to the right. Eventually it will reach the vertical wall, and run up on the wall and generate an overturning return wave. The specific dimensions of the tank is from the experiment in Zhou et al. [1999], which is often used for assessment of numerical models developed for flows with extreme deformations of the free surface and wave impacts on structures, e.g. Ferrari et al. [2009]. In the experiment by Zhou et al. [1999] the depth was measured at four locations and the pressure (using pressure probes with a diameter of 9cm) at the right wall was measured at three locations. The location of the depth measurements are $x_{H_1} = 2.725$m, $x_{H_2} = 2.228$m, $x_{H_3} = 1.730$m and $x_{H_4} = 0.600$m and the vertical locations of the pressure probes are $y_{P_1} = 0.160$m, $y_{P_2} = 0.584$m and $y_{P_1} = 1.000$m.

The dam break has been run with four different resolutions. The resolution changes throughout the simulation, so each run will be identified by the initial number of points $N(0)$, which in the four cases are $N(0) = 2292$, $N(0) = 4972$, $N(0) = 8676$ and $N(0) = 19156$. Each case is run until the numerical model breaks down. The evolution of the fluid domain with $N(0) = 8676$ is seen in figures 8.10 and 8.11, where the the fluid domain is shown with time intervals of approximately $\sqrt{H/g}$. The first figure shows the initial fluid domain, just after the removal of the sluice gate. It is seen that the pressure is almost hydrostatic towards the left, but less than hydrostatic towards the right. This pressure distribution accelerates the water as in a corner flow: downwards and towards the right. At time $t/\sqrt{H/g} = 1.0$ and $t/\sqrt{H/g} = 2.0$ the fluid domain has a wetting front moving to the right. At time $t/\sqrt{H/g} = 3.0$ and $t/\sqrt{H/g} = 4.0$ the wetting front has hit the right wall and a jet is shooting up the wall. At time $t/\sqrt{H/g} = 5.1$ the jet has been decelerated and a wave focusing builds the overturning return wave. The overturning return wave is fully developed at time $t/\sqrt{H/g} = 6.1$ and is just about to plunge into the wave trough. At time $t/\sqrt{H/g} = 7.1$ the wave has plunged, a cavity has formed and

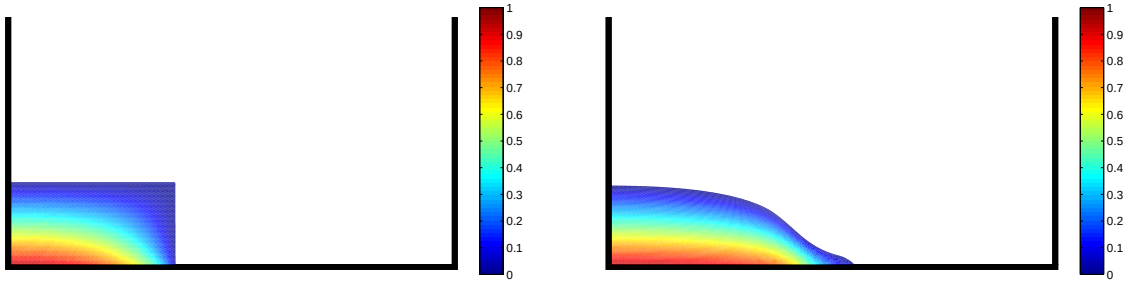

(a) $t/\sqrt{H/g} = 0.0$

(b) $t/\sqrt{H/g} = 1.0$

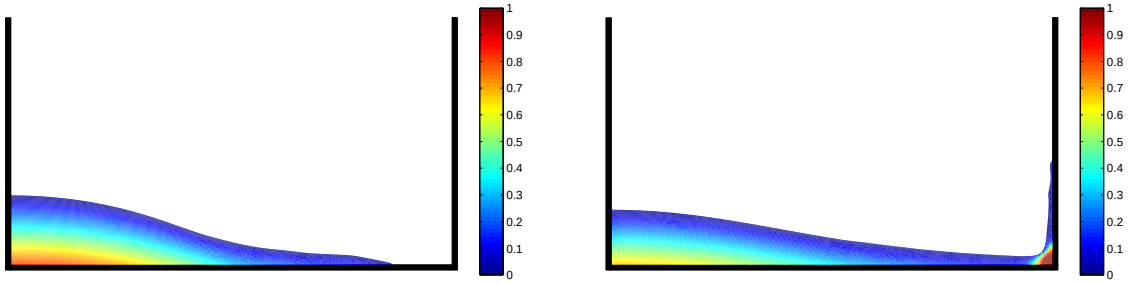

(c) $t/\sqrt{H/g} = 2.0$

(d) $t/\sqrt{H/g} = 3.0$

Figure 8.10: The evolution of the fluid domain after the dam break. The color scale is based on the dimensionless pressure $p/(\rho g H)$.

a new upwards moving jet is made by the plunging wave.

The asymptotic wave front velocity for the ideal fluid flow solution to the dam break problem on a dry bed has been derived by Ritter [1892], it is

$$u = 2\sqrt{Hg}. \tag{8.8}$$

Figure 8.12 shows the position of the front wave of the dam-break for all four simulations. In the same figure is the asymptotic solution by Ritter [1892] and the experimentally obtained front position in the experiment by Martin and Moyce [1952]. It is seen that the propagation speed obtained with the ALE-WLS solution tends to the asymptotic solution. The experimentally obtained front wave has a slower propagation speed than the ALE-WLS solution. This has also been observed with other models and methods, e.g. the SPH and level set method, see Ferrari et al. [2009].

Evolutions in the depths measurement location $H1$ and $H2$ are seen in figure 8.13. In the experiment the wave front is a turbulent bore and it give a small rise and fall in the free surface elevation as it passes the measurement location. This physics is not modelled in the this inviscid model and the numerically calculated wave front does not have this initial elevation rice and fall. After the front wave has passed the calculated elevations compares well. The time of appearance of the return wave in the measurement are $t/\sqrt{g/H} \approx 5.5$ at $H1$ and $t/\sqrt{g/H} \approx 6.5$ at $H1$. This time is very well predicted by

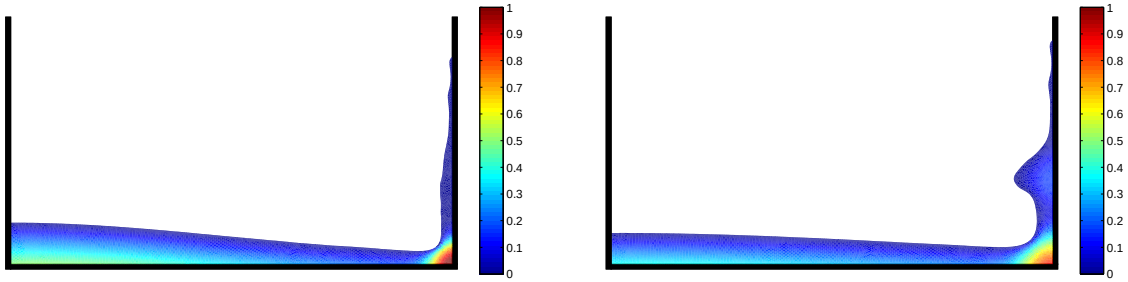

(a) $t/\sqrt{H/g} = 4.0$

(b) $t/\sqrt{H/g} = 5.1$

(c) $t/\sqrt{H/g} = 6.1$

(d) $t/\sqrt{H/g} = 7.1$

Figure 8.11: The evolution of the fluid domain after the dam break. The color scale is based on the dimensionless pressure $p/(\rho g H)$.

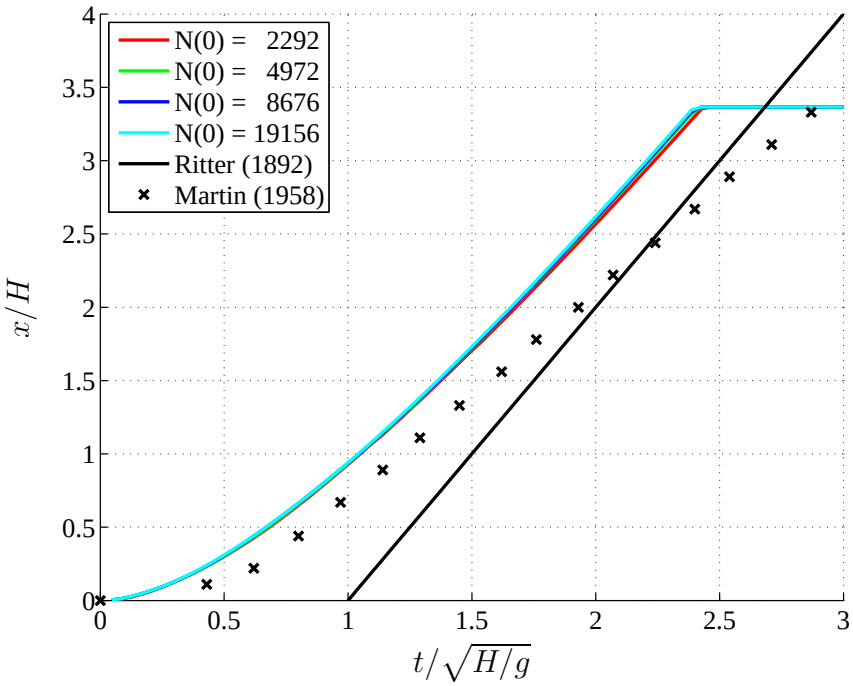

Figure 8.12: The position of the wave front as a function of time, compared with the asymptotic Ritter [1892] solution and the experiment by Martin and Moyce [1952].

the numerical model, but the elevation is too high. It is not fully understood why the numerical model is to high. It may come from the inviscid and incompressible governing equations. The viscosity would give less momentum in the return wave. The timescale of the wave impact on the wall is very small and the impact gives very large accelerations. In the incompressible model does not allow pressure wave to propagate throughout the medium at a finite speed. These pressure waves resulting from the impact may be of importance Bredmose et al. [2009].

The water reaches the pressure probe P2 at approximately $t/\sqrt{H/g} = 2.5$. The pressure at P2 is seen in figure 8.14. After the water has reached the probe the pressure increases very fast to a local peak pressure. The numerical model under estimates this initial pressure increase. From approximately $t/\sqrt{H/g} = 4$ to $t/\sqrt{H/g} = 6$ the pressure is almost constant. This is corresponds to the time of maximum run-up to the time where the overturning return wave plunges. The overturning return wave develops in this time interval. As the upwards jet is decelerated the pressure increases close to wall, it pushes the water away from the wall and this results in the overturning return wave. The initial development of the return wave is seen in figure 8.15. The plunging of the return wave results in a large pressure on the wall at $t/\sqrt{H/g} = 6$ to $t/\sqrt{H/g} = 7$. It is also in this time interval that the force on the wall is maximum, as seen in figure 9.16.

The plunging of the overturning return wave is seen in figures 8.16. As the wave plunges the pressure increases in a small area just were the wave impinges. The most pronounced result of this high pressure is the formation of a jet which shoots up and away from the plunging wave. A phenomenon like this gives very large pressure gradients and accelerations.

The evolutions in the number of calculation points are seen in figure 8.18. There

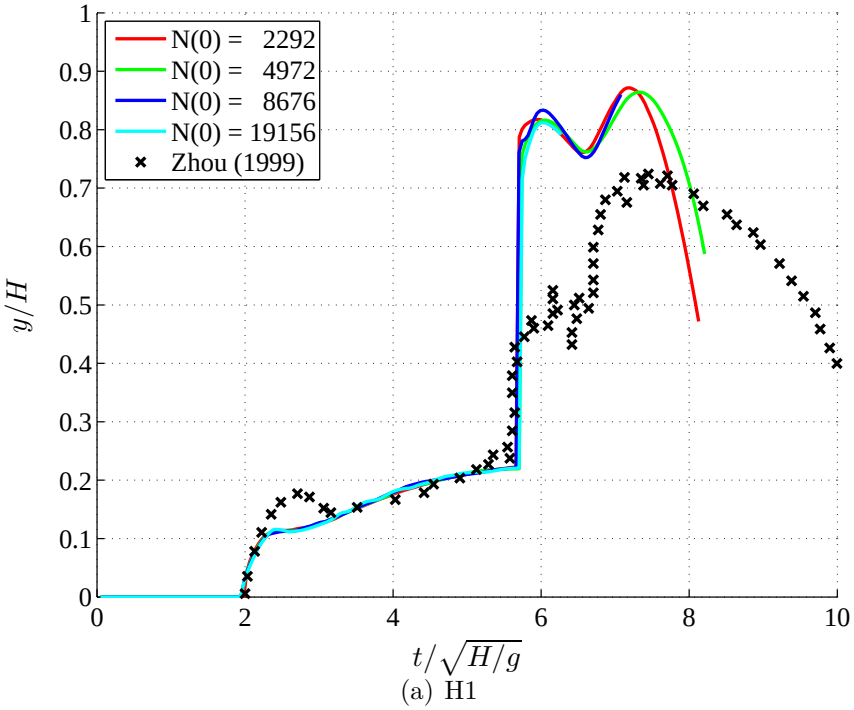

(a) H1

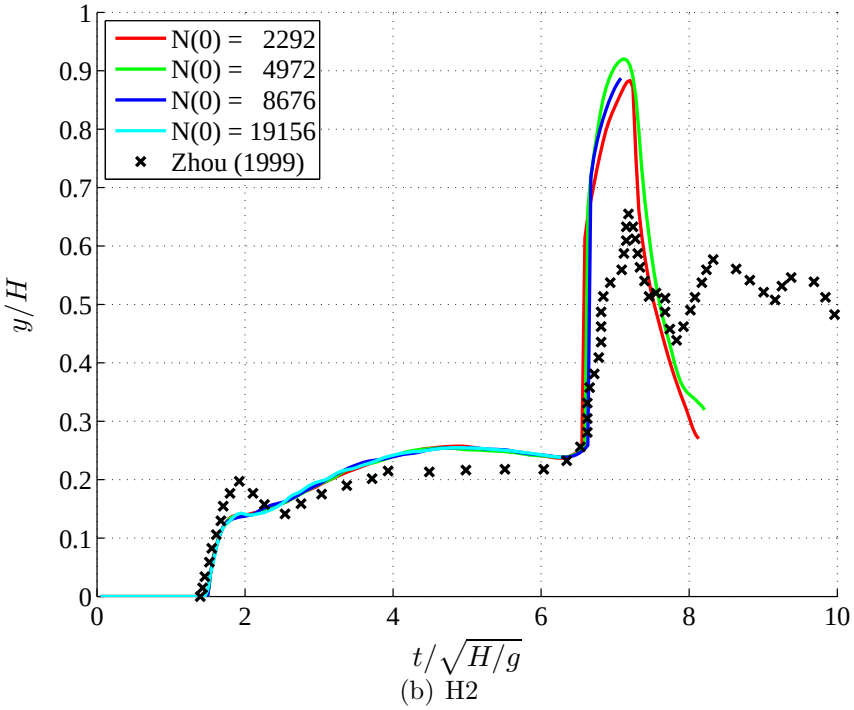

(b) H2

Figure 8.13: Depth at measurement location $H1$ and $H2$.

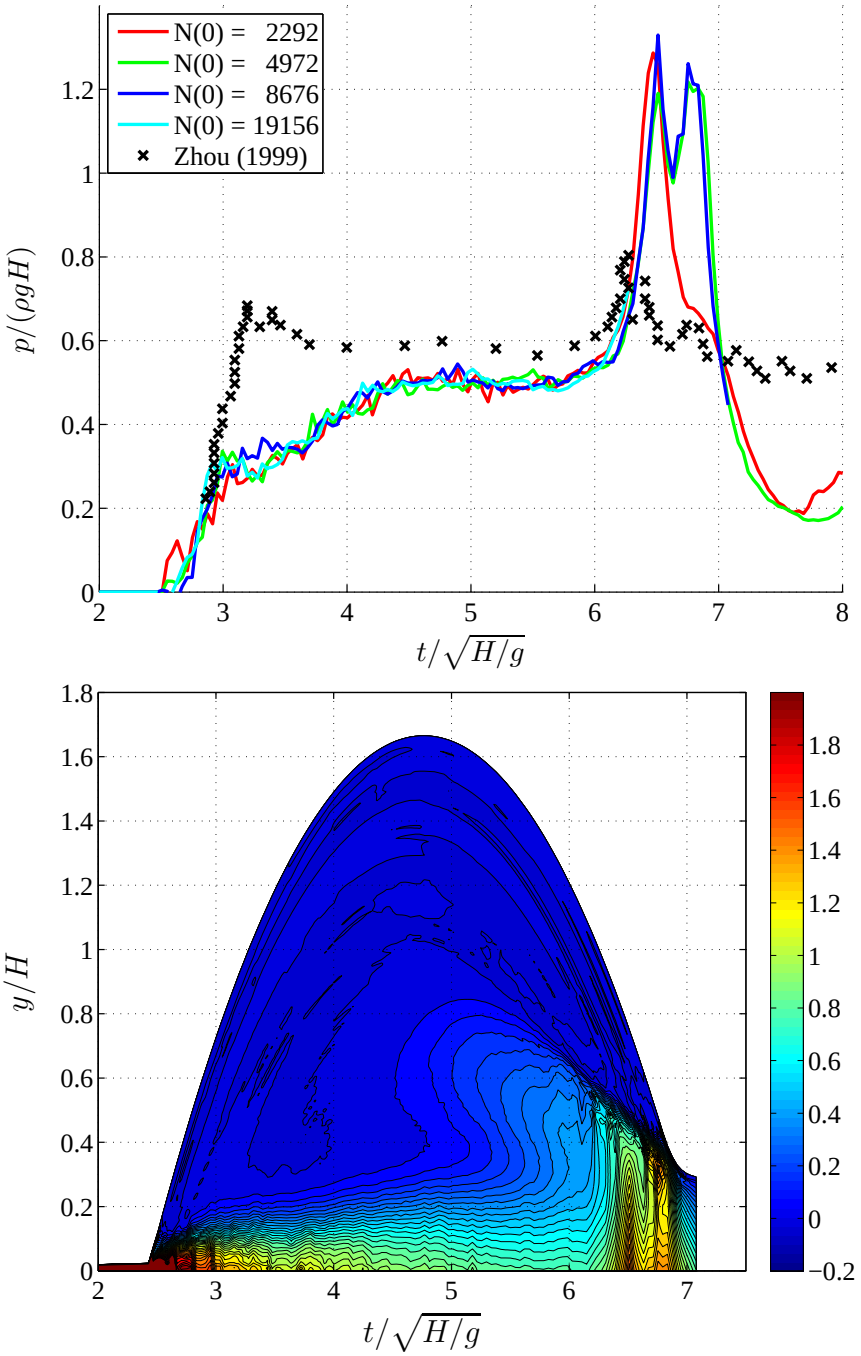

Figure 8.14: Top: The pressure calculated at probe P2. Bottom: Pressure $p/(\rho g H)$ at the vertical wall.

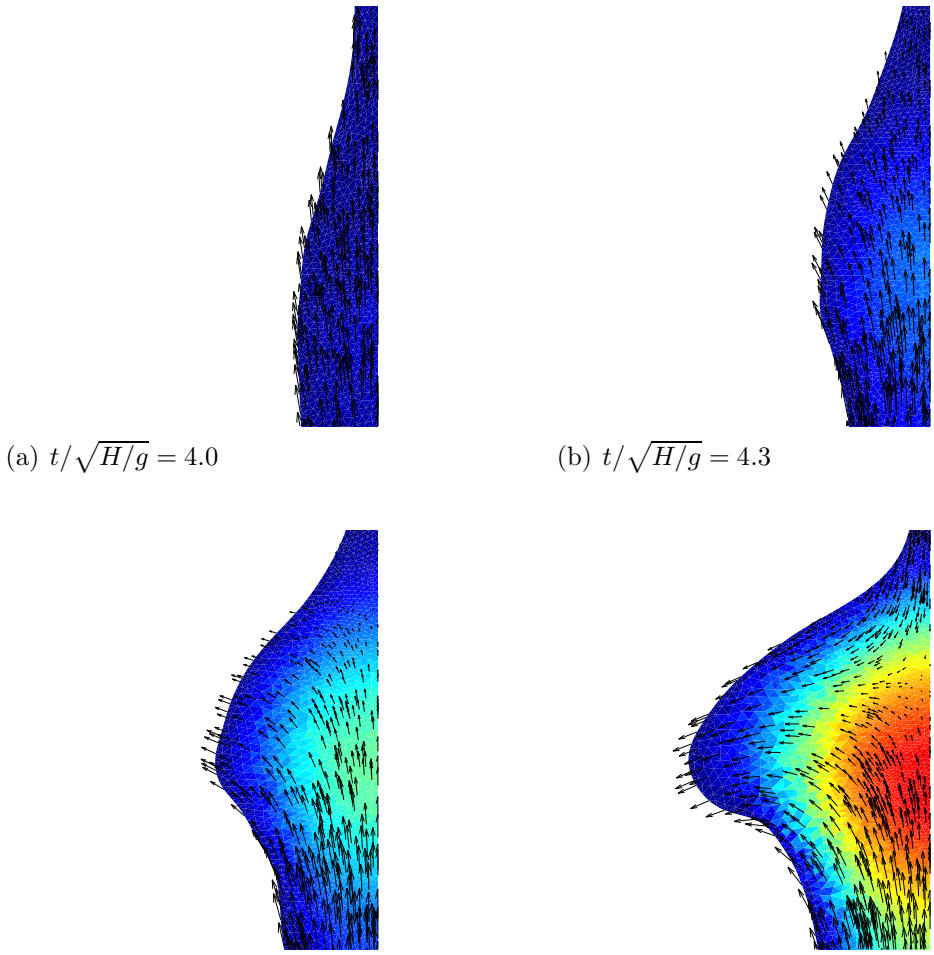

(a) $t/\sqrt{H/g} = 4.0$

(b) $t/\sqrt{H/g} = 4.3$

(c) $t/\sqrt{H/g} = 4.7$

(d) $t/\sqrt{H/g} = 5.0$

Figure 8.15: Development of the overturning return wave. The color scale from for pressure has the range from 0 (blue) to $\frac{1}{6}\rho g H$ (red).

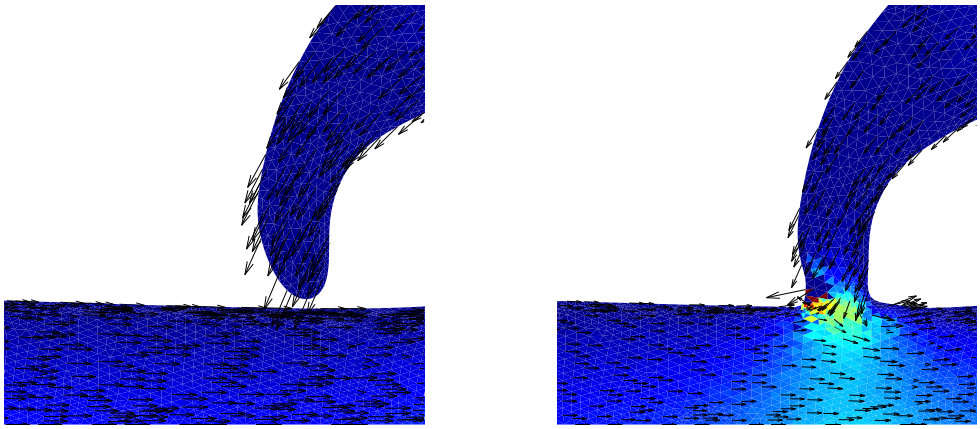

(a) $t/\sqrt{H/g} = 6.03$ (b) $t/\sqrt{H/g} = 6.07$

(c) $t/\sqrt{H/g} = 6.11$ (d) $t/\sqrt{H/g} = 6.15$

Figure 8.16: The plunging of the overturning return wave.Development of the overturning return wave. The color scale from for pressure has the range from 0 (blue) to $2\rho gH$ (red).

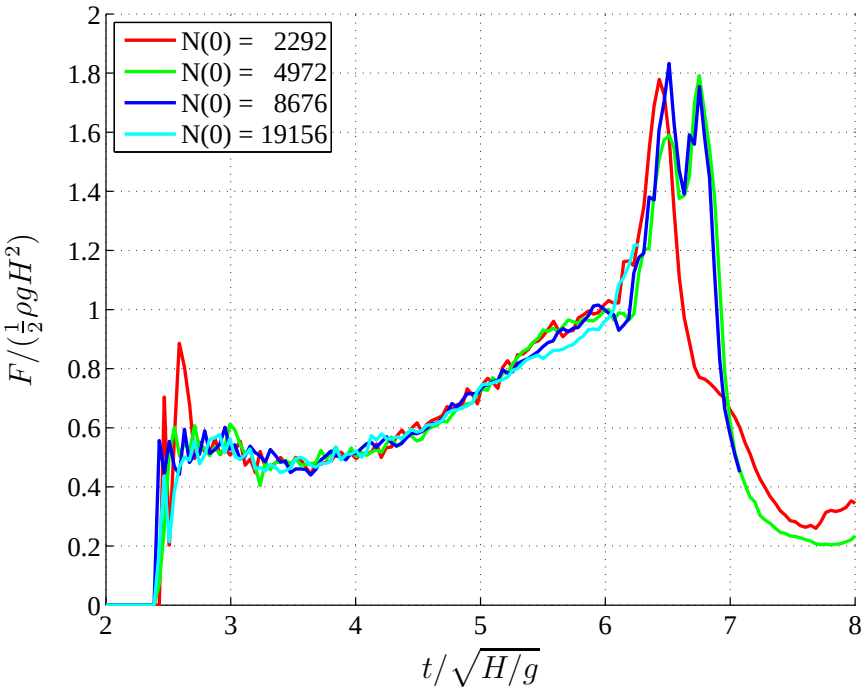

Figure 8.17: The pressure force on the vertical wall.

are some variations in the number of points throughout the simulations. The coarse simulation has a 50% increase in the number of points, where as the two finest resolution has a 10% loss in the number of points. Recall the the number of points are controlled by the coarsening and refinements criteria based on fill distance. It is clear that the adaptivity is dependent on the resolution and it could be a good idea to add a lower limit to the number of points, e.g. the initial number of points $N(0)$.

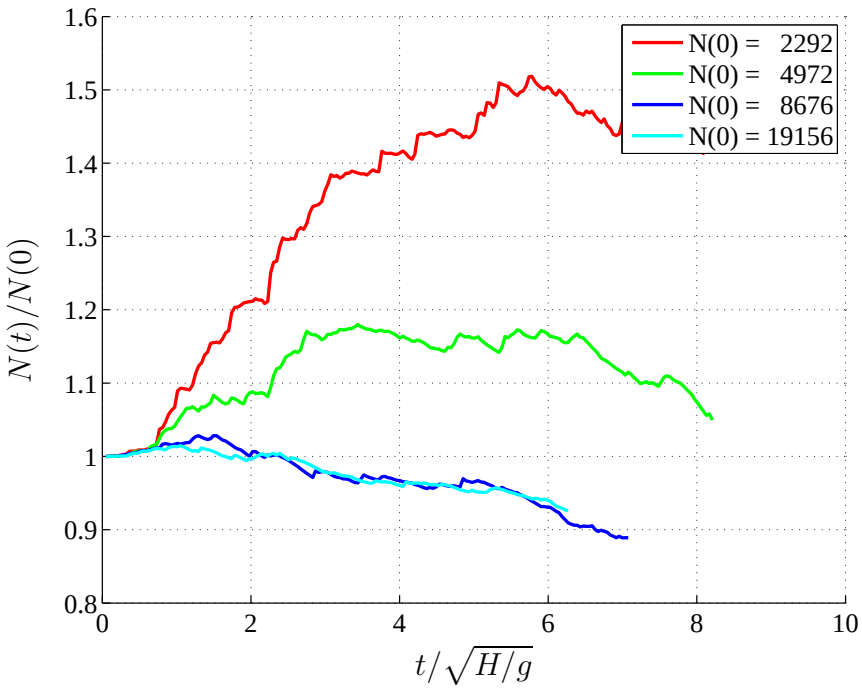

Figure 8.18: The relative number of points as a function of time for each of the four simulations.

Chapter 9

Breaking Wave Impact on a Vertical Breakwater

Thorough experimental and numerical investigations of breaking wave impacts on a vertical wall have been conducted in the series of papers Bullock et al. [2007] and Bredmose et al. [2009]. The first paper presents experimental data for impact pressures and forces generated by waves up to a height of $H = 1.7$m. The second paper presents a theoretical study of the breaking wave impacts on a vertical wall. They confirm that the presence of either entrained or trapped air is important for the physical phenomenon and force calculations. Both entrained and trapped air are neglected in the incompressible and inviscid ALE-WLS model presented in this project and the interesting question is: How applicable is this model to breaking wave impacts? To answer this question, the same calculations as Bredmose et al. [2009] are carried out with the incompressible and inviscid ALE-WLS model. This comparison can give an indication of whether an incompressible single phase model is applicable to breaking wave impacts.

The physical domain for the theoretical study is a two dimensional approximation of an experiment conducted in the Grosser Wellenkanal (GWK) Bredmose et al. [2009]. The dimensions of the wave tank are: length 350m and width 5m. The bottom of the wave channel is flat, with the exception of a rubble mound placed below the vertical wall. The rubble mound is approximated by an quarter of an ellipse with length 18m, height 3m and depth 4.25m. The initial condition is a fully nonlinear wave train Fenton [1988], which is modulated by a envelope function that creates a short wave group with three significant crests. The wave impact characteristics Sumer and Fredsøe [1997] are found to be dependent on the initial offshore wave height H and the observed wave impacts are of the types

- Reflective sloshing: The wave is non-overturning and a thin sheet of water runs up the wall as the wave is reflected on the wall.

- Flip-though: The approaching wave is overturning, but no air is trapped due to a sudden acceleration of the wave trough which forms a jet that shoots up the wall.

- Overturning wave with trapped air: The approaching wave is overturning and a cavity with trapped air forms between the free surface and the wall.

The flip-through impact occurs for the offshore wave heights of $H = 1.33$m and $H = 1.36$m. The wave heights of $H = 1.42$m and $H = 1.45$m gives an impact between flip-through and overturning wave with trapped air. Finally the heights $H = 1.48$m and $H = 1.51$m make an overturning wave with trapped air.

For the smooth and non-overturning waves the compressible, viscous and rotational effects are negligible and potential flow theory gives a good approximation Engsig-Karup et al. [2009]. These effects are also negligible in the early stages of wave breaking and the potential flow theory is still a valid approximation Bredmose et al. [2009]. In the later stages of wave breaking the fluid becomes a water and air mixture where viscous and rotational effects becomes significant. The largest forces due to wave impact occur if the wave overturning develops just before the impact Sumer and Fredsøe [1997] where potential flow theory is applicable. In Bredmose et al. [2009] this was exploited and the overturning wave was modeled with a potential flow model. The compressible, viscous and rotational effects can be neglected if the impact resembles a reflective sloshing, but it gives relatively small forces and is therefore of less interest. Steep and slightly overturning waves that make a flip through impact which can be modelled by potential flow theory Peregrine [2003]. If a cavity of air gets trapped then multi-phase and compressible effects are important for an accurate force calculation.

In this project two models have been coupled to calculate the wave impacts: The first model calculates the wave propagation from offshore to the vicinity of the breakwater and the second model calculates the wave overturning and impact on the breakwater. The first model is a higher-order finite difference potential flow model with nonlinear kinematic and dynamic free surface boundary conditions Engsig-Karup et al. [2009]. The second is the incompressible and inviscid ALE-WLS model presented in this project. The wave groups are propagated to the vicinity of the breakwater where the waves are steep, but still smooth and non-overturning. These waves are used as the initial condition for the incompressible and inviscid WLS model and the wave impacts on the vertical breakwater are simulated using this model. The governing equations for the nonlinear potential flow model are presented in the next section. The numerical approximations, implementation and examples of wave propagation are given in Engsig-Karup et al. [2009]. The incompressible and inviscid ALE-WLS model are described in the chapters 4, 5, 6 and 7. In summary the approximations are explicit 4th order Runge-Kutta time integration, 2nd order WLS combined with central or Rusanov flux and 2nd order GFPM approximation of the Poisson equation.

9.1 The Nonlinear Potential Flow Model

This section describes the potential flow model of Engsig-Karup et al. [2009]. The coordinate in the two dimensional fluid domain $\Omega(t) \subset \mathbb{R}^2$ is defined by a time-dependent mapping of a reference coordinate $\boldsymbol{\xi} \in \Xi \subset \mathbb{R}^2$ via the transformation

$$\boldsymbol{x}(t, \boldsymbol{\xi}) : \Xi \to \Omega(t), \quad \xi \in \Xi, \quad t \in [0, t_{max}], \tag{9.1}$$

where t is time. The limits of the reference domain is $0 \leq \xi_1 \leq L_1$ for the horizontal coordinates and $0 \leq \xi_2 \leq 1$ for the vertical coordinate. The coordinate transform is given

by the linear transfinite interpolation

$$\begin{aligned} x_1 &= \xi_1, \\ x_2 &= x_2(t,\xi_1,0) + \xi_2\left(x_2(t,\xi_1,1) - x_2(t,\xi_1,0)\right), \end{aligned} \tag{9.2}$$

where the latter is often called the σ-coordinate transform. The lower boundary condition for the fluid domain is the depth measured from the still water level $x_2(t,\xi_1,0) = -h = -h(x_1)$ and the upper boundary condition is the elevation of the free surface also measured from the still water level $x_2(t,\xi_1,1) = \eta = \eta(t,x_1)$. The elevation of the free surface is related to the flow kinematics through the total derivative

$$\frac{d\eta}{dt} = \frac{\partial\eta}{\partial t} + u_1\frac{\partial\eta}{\partial x_1}, \quad \xi_2 = 1, \tag{9.3}$$

where $u_1 \in \mathbb{R}$ is the horizontal fluid velocity at the free surface. This model assumes the fluid to be inviscid and incompressible and the flow to be irrotational, thus the flow velocity is the gradient of the velocity potential $\boldsymbol{u} = [u_1, u_2]^T = \nabla\phi \in \mathbb{R}^2$. The velocity potential is related to the dynamic and static pressures at the free surface through the Bernoulli equation

$$\frac{\partial\phi}{\partial t} + \frac{1}{2}\boldsymbol{u}\cdot\boldsymbol{u} + g\eta = 0, \quad \xi_2 = 1, \tag{9.4}$$

which the dynamic boundary condition at the free surface. In the incompressible, isothermal and irrotational fluid the mass conservation is satisfied via the Laplace equation for the velocity potential

$$\nabla^2\phi = 0, \quad 0 \le \xi_2 \le 1. \tag{9.5}$$

and finally the condition for impermeable and frictionless boundaries

$$\boldsymbol{n}\cdot\boldsymbol{u} = 0, \tag{9.6}$$

where $\boldsymbol{n}$ is the outward normal to the boundary. This zero normal flow condition is to be satisfied at the seabed $\xi_2 = 0$ and at the vertical walls at $\xi_1 = 0$ and $\xi_1 = L_x$.

The following system of evolution equations is obtained when the derivatives are written in therms of the reference coordinates and the velocity in terms of the velocity potential

$$\frac{\partial\phi}{\partial t} = -g\eta - \frac{1}{2}\left(\frac{\partial\phi}{\partial\xi_1}\right)^2 + \frac{1}{2}\left(\frac{1}{J}\frac{\partial\phi}{\partial\xi_2}\right)^2\left(1 + \left(\frac{\partial\eta}{\partial\xi_1}\right)^2\right), \tag{9.7}$$

$$\frac{\partial\eta}{\partial t} = -\frac{\partial\phi}{\partial\xi_1}\frac{\partial\eta}{\partial\xi_1} + \frac{1}{J}\frac{\partial\phi}{\partial\xi_2}\left(1 + \left(\frac{\partial\eta}{\partial\xi_1}\right)^2\right), \quad \xi_2 = 1, \tag{9.8}$$

where J is the Jacobian of the transformation eq. (9.2). For the Laplace equation and the zero normal flow boundary condition as a function of the reference we refer to Engsig-Karup et al. [2009].

The temporal derivatives are approximated by the classical fourth order Runge-Kutta method and the spatial derivatives are approximated using arbitrary order finite difference. The overall solution procedure and computer implementation of these equation are described and validated in Engsig-Karup et al. [2009]. This model can simulate nonlinear waves, but overturning waves and wave breaking are beyond its scope. As the waves starts to become steep, we switch to the incompressible and inviscid ALE-WLS model and use it to calculate the wave impact on the breakwater.

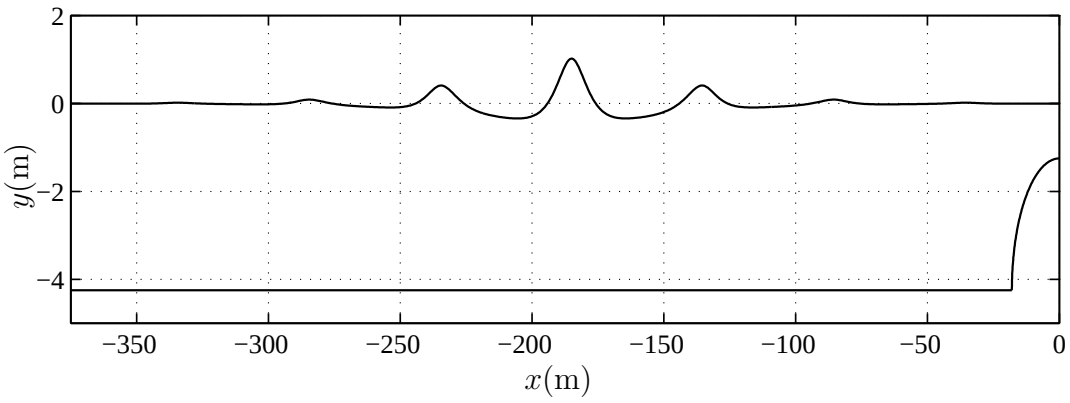

Figure 9.1: The seabed and the initial elevation of the free surface with $H = 1.45$m. The elliptical shaped rubble mount is seen in the right side.

9.2 Breaking Wave Impact

The models are applied to the calculation of pressure, force and impulse on a vertical breakwater subject to a wave impact. The specific test case is found in Bredmose et al. [2009], where the seabed is flat and the breakwater is protected by rubble mound with an idealized elliptical shape. The incident wave is a fully nonlinear regular wave in constant depth with the wave parameters height $H = 1.36$m, 1.40m, 1.42m, 1.45m, 1.48m and 1.51m, wavelength $L = 50$m and the modulated wave group is centered at $x = x_0 = -185$m. An example of an initial condition is seen in Fig. 9.1.

Smooth Wave Propagation

The wave group propagation towards the vertical breakwater has been simulated using the potential flow model Engsig-Karup et al. [2009]. The horizontal length of the physical domain is $L_x = 375$m, the depth offshore is $h(-375\text{m}) = 4.25$m and the depth at the wall is $h(0\text{m}) = 1.25$m. The elliptical rubble mound in front of vertical breakwater has a horizontal radius of $a = 18$m and a vertical radius of $b = 3$m. The mesh for the finite difference approximations has $N_x = 1025$ points in the horizontal direction and $N_z = 9$ points in the vertical direction and the finite difference approximations of spatial derivatives in the kinematic free surface boundary condition (9.8), dynamic free surface boundary condition (9.7) and the Laplace equation are of sixth order. The simulation has been run with a fixed time step of $\Delta t = 0.05$s, which corresponds to a Courant number of $C = c \times \Delta t/\Delta x \approx 0.8$, where c is the wave celerity of the incident wave according to linear wave theory.

An example of the calculated free surface evolution for an initial wave height $H = 1.48$m, is seen in figure 9.2 together with the corresponding potential flow calculation from Bredmose et al. [2009]. The free surface elevations from the two models compare very well until $t \approx 27$s. Beyond $t \approx 27$s the waves become increasingly steeper and spurious high frequency oscillations appears in the free surface elevations. These high frequency oscillations increase unbounded and eventually the model breaks down with a floating point exception.

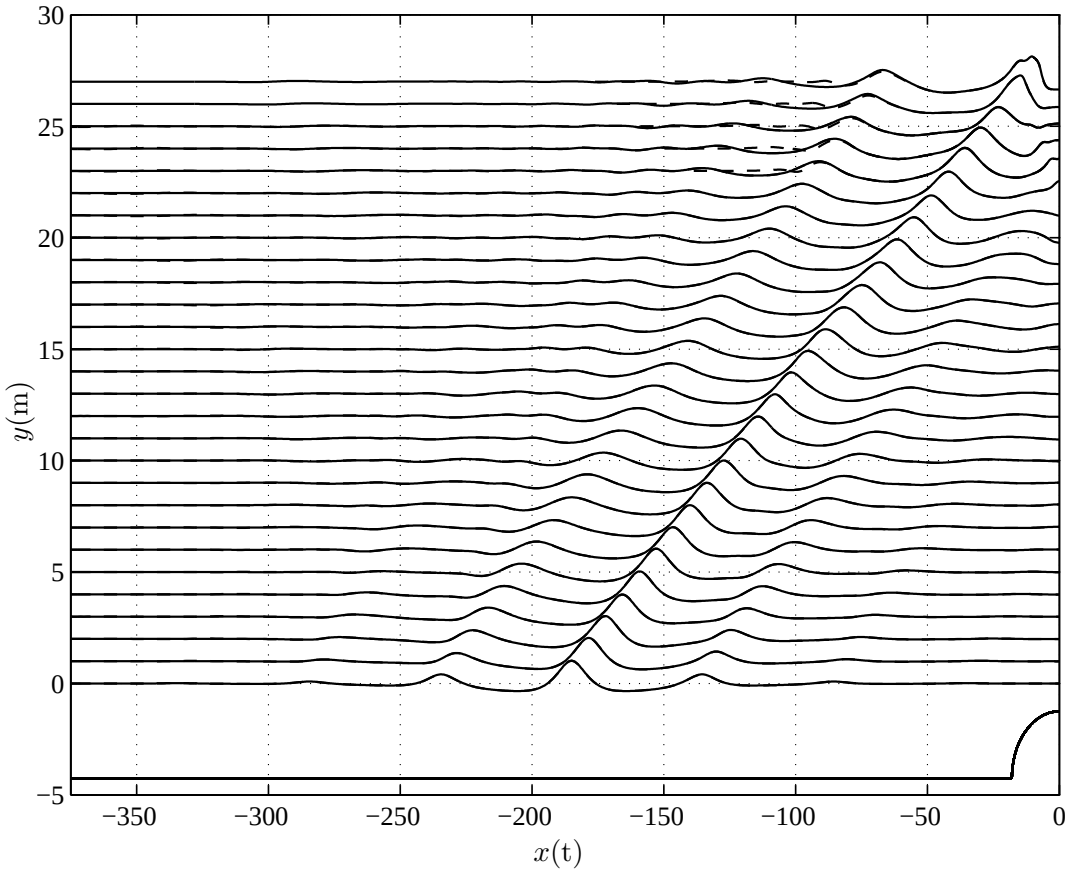

Figure 9.2: In this figure the lower line is the flat seabed and the surface of the elliptical rubble mound. The second line from below is the initial elevation of the free surface and the lines above are elevations of the free surface at later times with intervals of $\Delta t = 1$s. The time stack is made by offsetting the elevations by $t \times 1m/s$. Elevations with a full line are calculated with the present potential flow model and the elevations with the dashed line are calculated with the potential flow model in Bredmose et al. [2009].

The solutions for the free surface elevation and flow kinematics of the waves at $t = 27$s are now used as initial conditions for the incompressible and inviscid ALE-WLS model. This model calculates the waves approach to the vertical breakwater and its impact on the vertical breakwater.

Overturning Wave Propagation

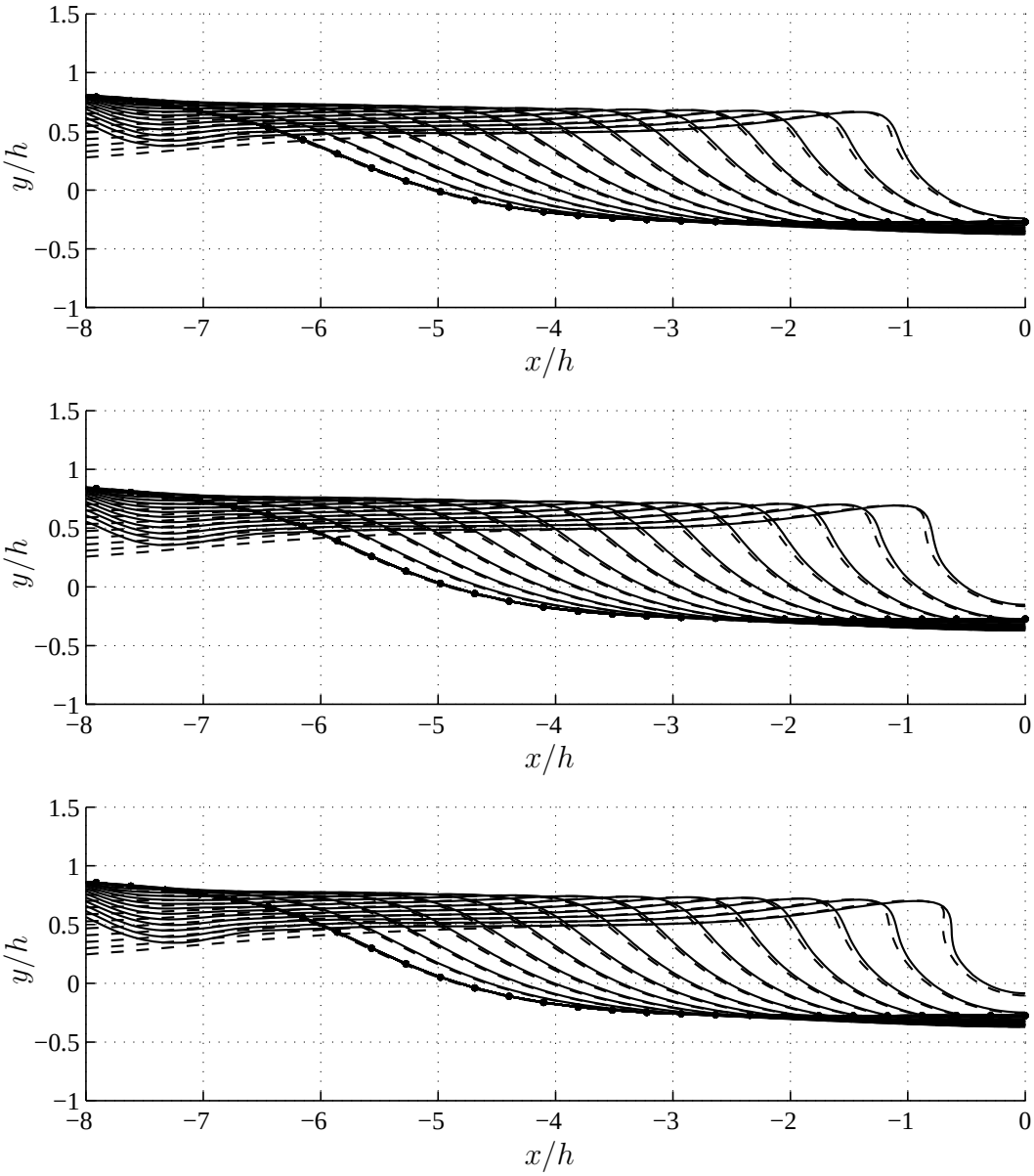

Figure 9.3: The free surfaces elevation from the ALE-WLS model with central flux, from time $t = 27.0$s to $t = 28.4$s with intervals of 0.1s, for the cases $H = 1.36$m, $H = 1.40$m and $H = 1.42$m. The dashed line show the free surface computed with BEM Bredmose et al. [2009] and the solid line with ALE-WLS.

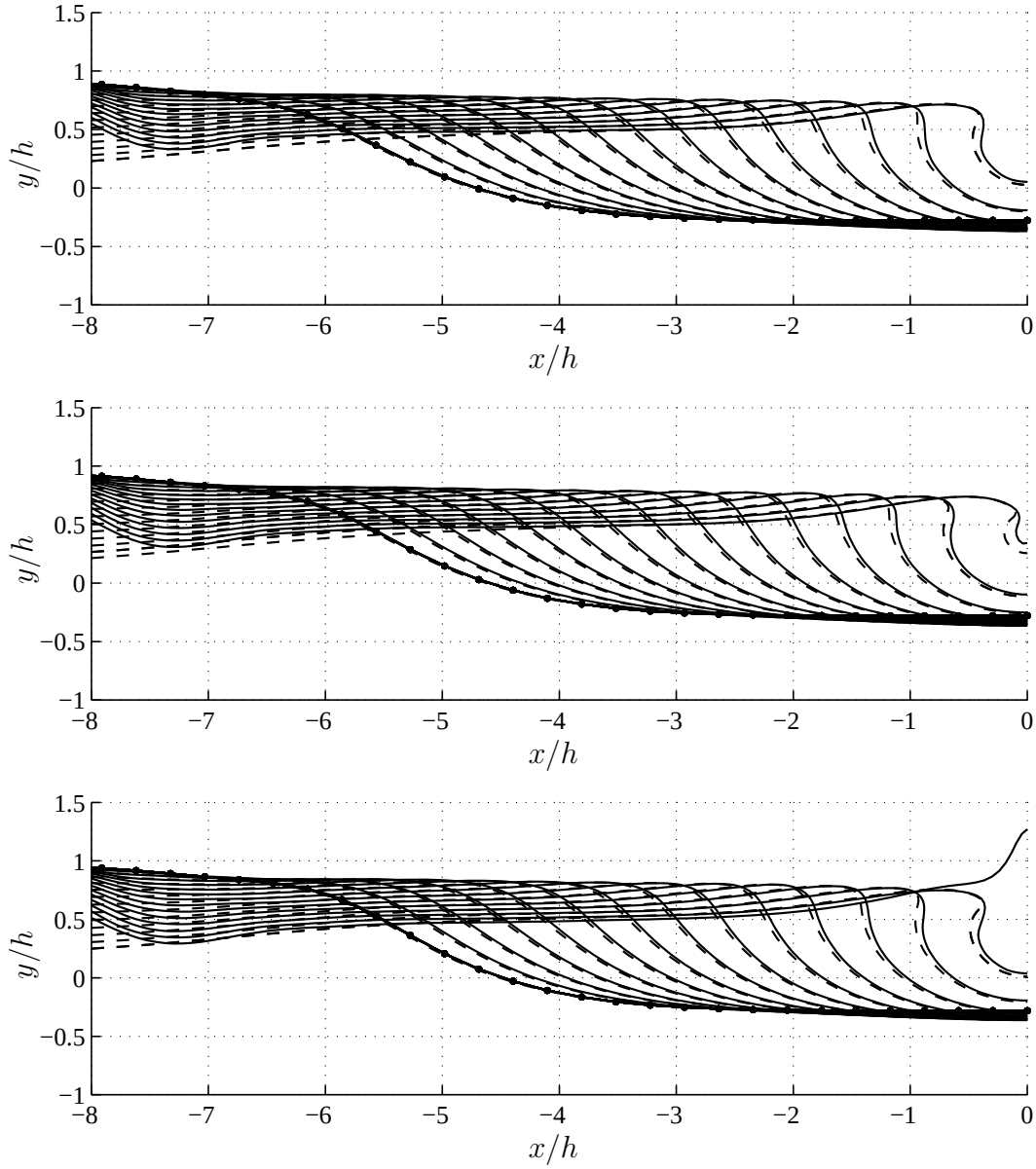

Figure 9.4: The free surfaces elevation from the ALE-WLS model with central flux, from time $t = 27.0$s to $t = 28.4$s with intervals of 0.1s, for the cases $H = 1.45$m, $H = 1.48$m and $H = 1.51$m. The dashed line show the free surface computed with BEM Bredmose et al. [2009] and the solid line with ALE-WLS.

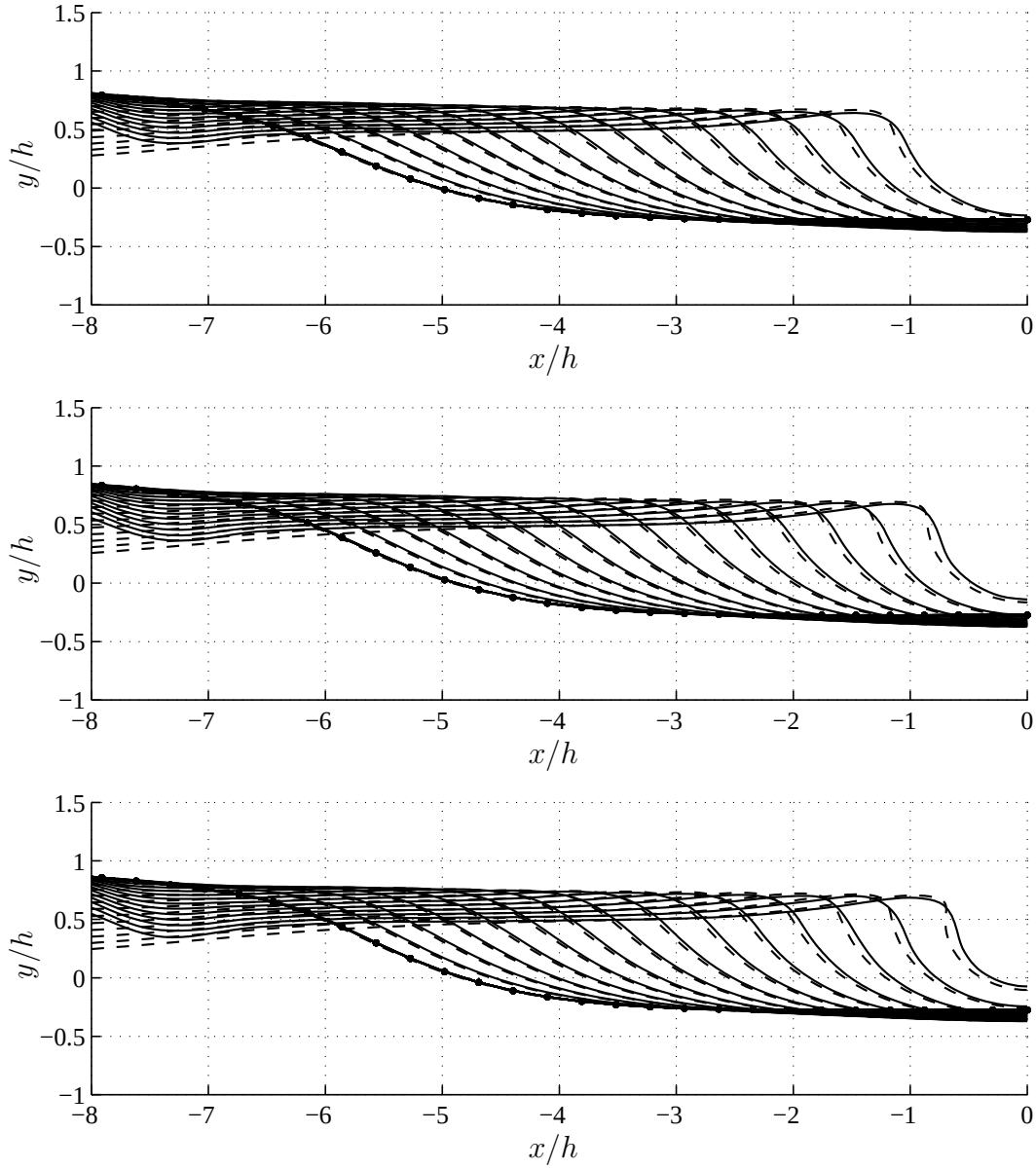

Figure 9.5: The free surface elevation from the ALE-WLS model with Rusanov flux, from time $t = 27.0$s to $t = 28.4$s with intervals of 0.1s, for the cases $H = 1.36$m, $H = 1.40$m and $H = 1.42$m. The dashed line show the free surface computed with BEM Bredmose et al. [2009] and the solid line with ALE-WLS.

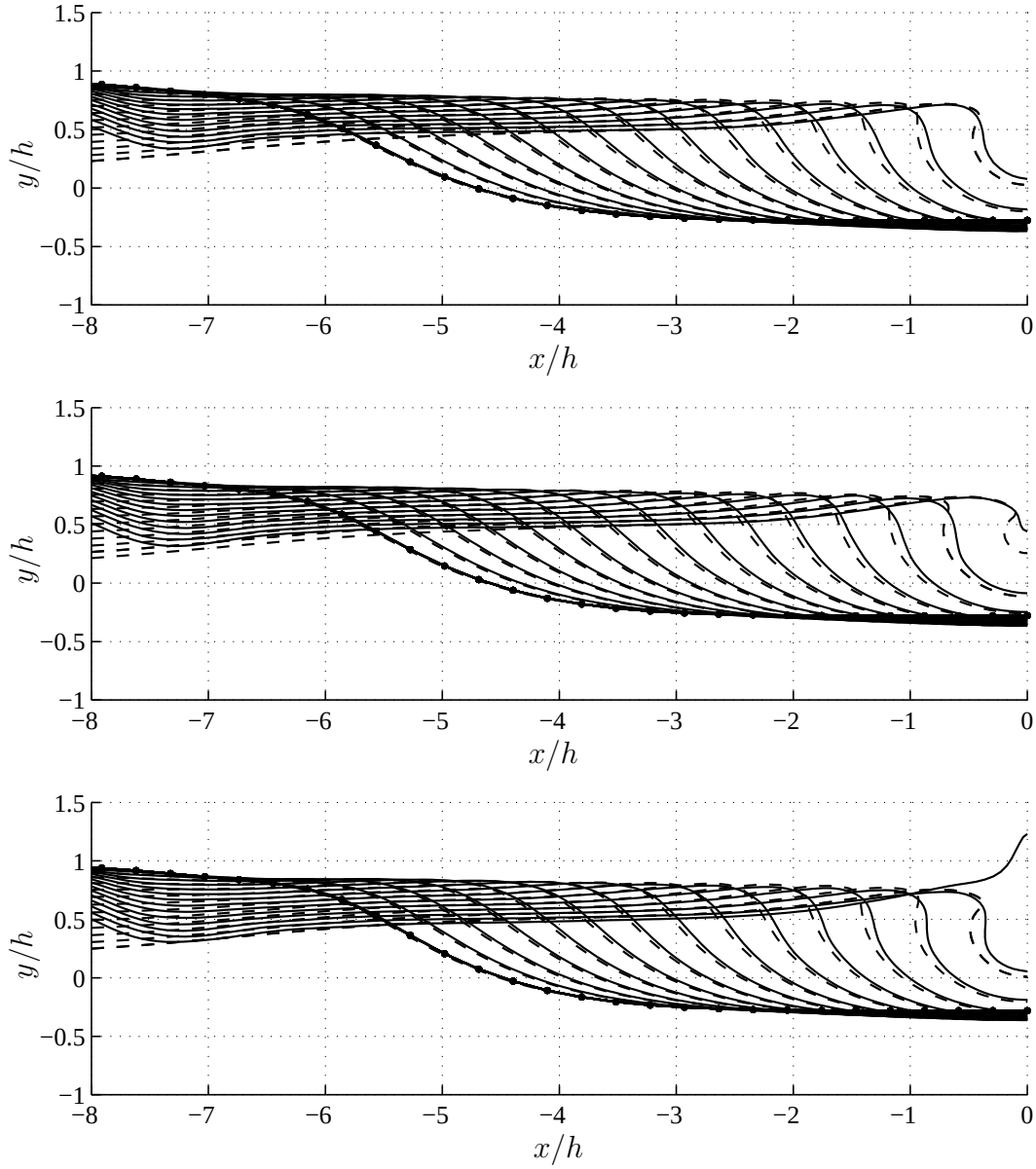

Figure 9.6: The free surface elevation from the ALE-WLS model with Rusanov flux, from time $t = 27.0$s to $t = 28.4$s with intervals of 0.1s, for the cases $H = 1.45$m, $H = 1.48$m and $H = 1.51$m. The dashed line show the free surface computed with BEM Bredmose et al. [2009] and the solid line with ALE-WLS.

The free surface elevations and the flow kinematics at time $t = 27.0$s are used as initial conditions for the incompressible and inviscid ALE-WLS model model. The physical domain for these simulations is much smaller: From $x = -10.0$m to the breakwater at $x = 0.0$m. The finite difference mesh is too coarse for this model and the initial conditions need to be interpolated to a finer point distribution. This interpolation is carried out in the reference coordinates (9.2), where the new points are $169 \times 61 = 10339$ uniformly distributed points between $-10.0 \leq \xi_1 \leq 0.0$ and $0.0 \leq \xi_2 \leq 1.0$. The 2nd order WLS method is used for the solution interpolations and the points are mapped back to the physical domain using the coordinate transform (9.2).

The incompressible and inviscid ALE-WLS model is run with both central and Rusanov flux. The free surface evolutions calculated with central flux are seen in the figures 9.4 and the free surface evolutions with Rusanov flux are seen in the figures 9.6. It is seen that the initial conditions at $t = 27.0$s are smooth and non-overturning. The free surface elevations from $t = 27.0$s to $t = 28.4$s are plotted with intervals of 0.1s, together with the corresponding free surface elevations from the potential flow model Bredmose et al. [2009]. The two simulations have some small differences, but otherwise the two models seems to give comparable results. The central flux calculations compare reasonably well also for the overturning waves. The Rusanov flux seem to smooth the velocity field such that the wave overturning is not calculated as well. The accuracy depends on the spatial and temporal numerical resolution. All the calculations presented here are not satisfactorily resolved around the wave impact. This applies to the resolution in both space and time.

It is seen that evolution of the free surface elevation depends on the initial wave height H. A high initial wave elevation results in a the higher propagation speed and the wave steepening and overturning starts earlier. These results shows that the coupling of the nonlinear potential flow model and the incompressible and inviscid ALE-WLS models can calculate two-dimensional nonlinear overturning waves which are compare able to potential flow BEM calculations in Bredmose et al. [2009].

Wave Impact

More detailed free surface profiles and pressure contours on the vertical breakwater for are seen in the figures 9.8 and 9.9. The pressure has been smoothed using a second order WLS filter to produce the contour plots. The impact characteristic of the smallest wave $H = 1.36$m are of the reflective sloshing type. The impact characteristics of the waves with $H = 1.40$m, $H = 1.42$m and $H = 1.45$m are of flip through type, because the wave is almost overturning or overturning and no cavity is formed between the water and the wall. The impact characteristics of the waves $H = 1.48$m and $H = 1.51$m are probably also flip through type, but they are very close to being an overturning wave with trapped air.

The pressure increase on the wall is associated with the deceleration of the wave in the horizontal direction and an upward acceleration of the water. The infinite speed of pressure waves due to the incompressible assumption is clearly seen in these figures. The pressure increase from the local wave impact results in a sudden pressure increase on the whole wall. The pressure contours becomes very vertical during the wave impact, this is due to the infinite propagation speed of pressure waves. The pressure contours show that

the duration of the wave impact becomes smaller with increasing initial wave height H. The maximum pressure increases with increasing wave height. The increasing maximum pressure with increasing initial wave height is also seen in figure 9.10. In Bredmose et al. [2009] the maximum pressure and force occur for the wave with height $H = 1.45m$, due to the effect of trapped air which gives a compressible cushion effect. The maximum pressure for the $H = 1.45$m wave calculated with the incompressible and inviscid ALE-WLS with central flux is ≈ 2 times larger than the corresponding compressible calculation in Bredmose et al. [2009]. In the present calculation the largest wave height $H = 1.51$m gives the maximum force. The maximum force is for the wave with height $H = 1.45$m in Bredmose et al. [2009]. The maximum force for the $H = 1.45$m wave calculated with the incompressible and inviscid ALE-WLS with central flux is ≈ 1.5 times larger than the corresponding compressible calculation in Bredmose et al. [2009].

The figures 9.12 and 9.13 shows the breaking wave impacts calculated with the incompressible and inviscid ALE-WLS model with Rusanov flux. The impact characteristic of the of the smallest waves $H = 1.36$m and $H = 1.40$m are of reflective sloshing type. The rest of the wave impacts $H = 1.42$m, $H = 1.45$m, $H = 1.48$m and $H = 1.51$m are of flip through type. Non of the waves are overturning with trapped air. Clearly the Rusanov-flux has smoothed the kinematics of the incompressible and inviscid ALE-WLS model. Figure 9.16 shows that the $H = 1.48$m wave gives the maximum pressure on the wall. The maximum pressure for the $H = 1.45$m wave is $\approx 1.5 - 2.0$ times higher that calculated with the compressible model in Bredmose et al. [2009]. The maximum force is increasing with increasing wave height. For the $H = 1.45$m wave the maximum force is approximately the same as calculated with the compressible model Bredmose et al. [2009]. In general the maximum pressures and the forces are smaller than with a central flux.

Wave impact on a vertical breakwater, Bredmose et al [2009]

Convergence for 2nd order WLS and GPFM with Rusanov flux:

Wave impact on a vertical breakwater, Bredmose et al [2009]

Convergence for 4th order WLS and GPFM with Rusanov flux:

Performance

Performance measurement of total time loop (green) and Runge-Kutta 4th order (red) for the cases elliptical drop, standing wave, dam break and wave impact:

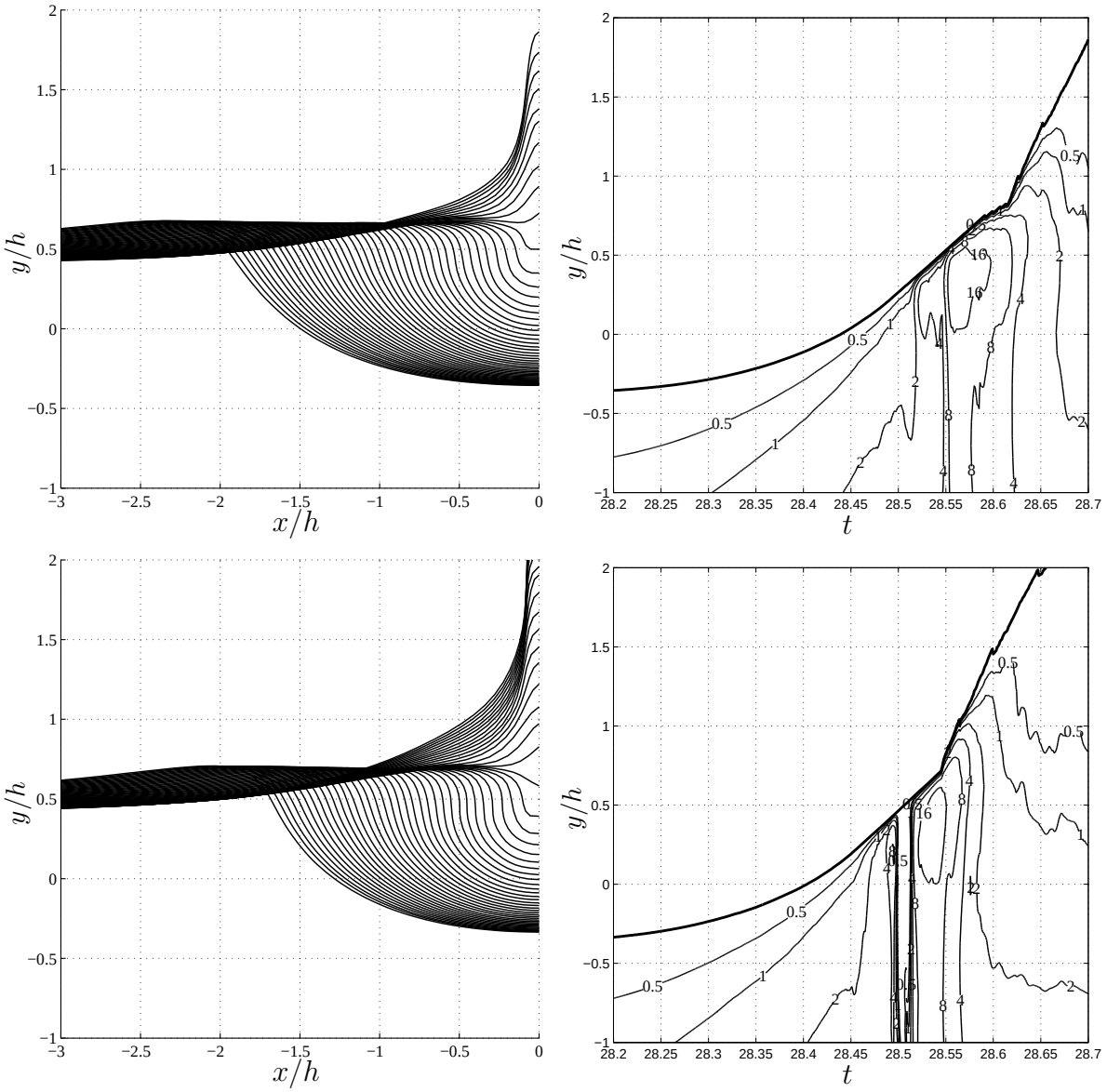

Figure 9.7: Wave impacts with the incompressible and inviscid ALE-WLS model with central flux. Left column: The free surface from time $t = 28.2$s to $t = 28.7$s with intervals of 0.01s, for the initial wave heights of $H = 1.36$m and $H = 1.40$m. Right column: The dimensionless pressure $p/(\rho g h)$ on the vertical wall for the same wave heights.

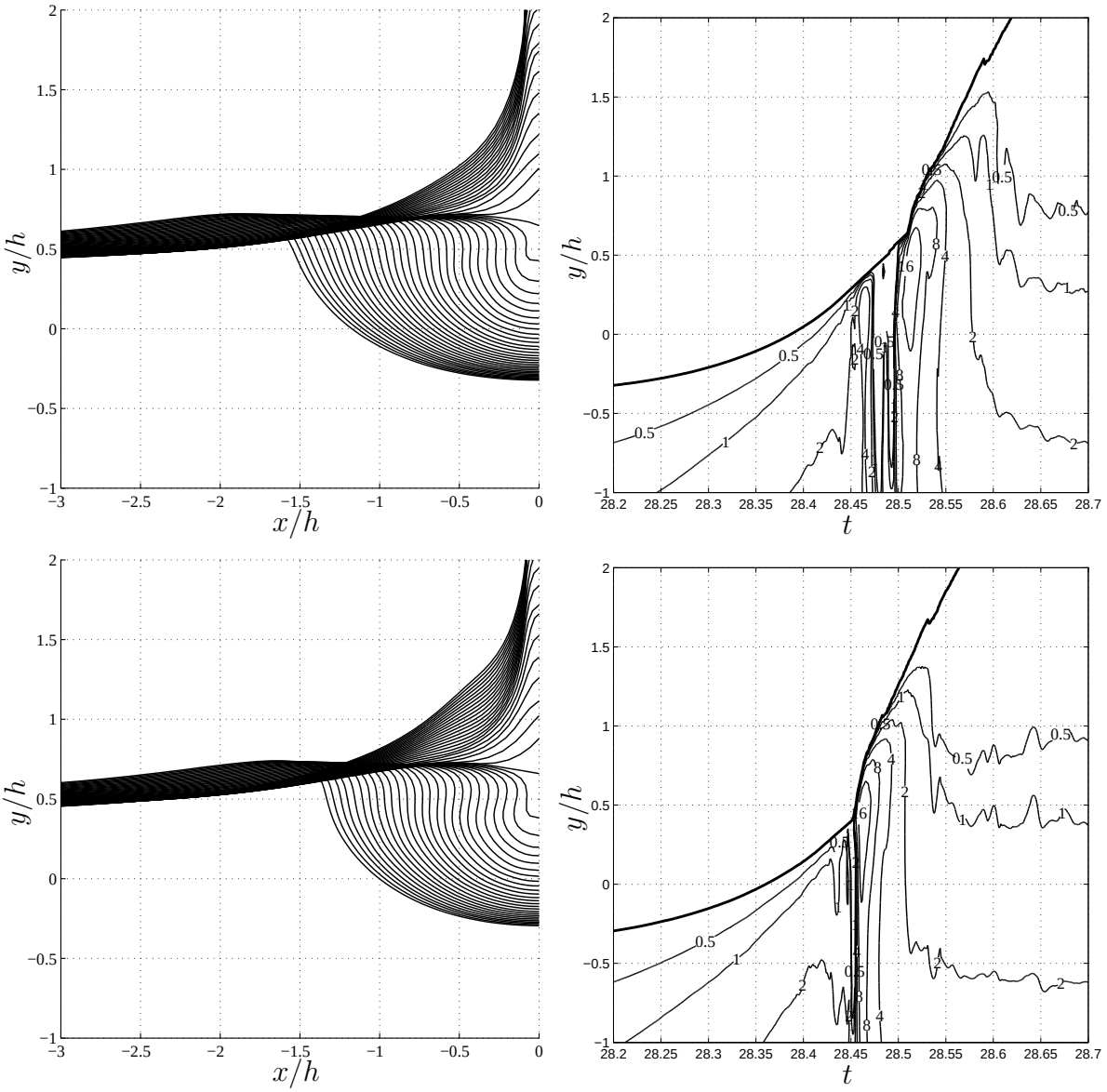

Figure 9.8: Wave impacts with the incompressible and inviscid ALE-WLS model with central flux. Left column: The free surface from time $t = 28.2$s to $t = 28.7$s with intervals of 0.01s, for the initial wave heights of $H = 1.42$m and $H = 1.45$m. Right column: The dimensionless pressure $p/(\rho g h)$ on the vertical wall for the same wave heights.

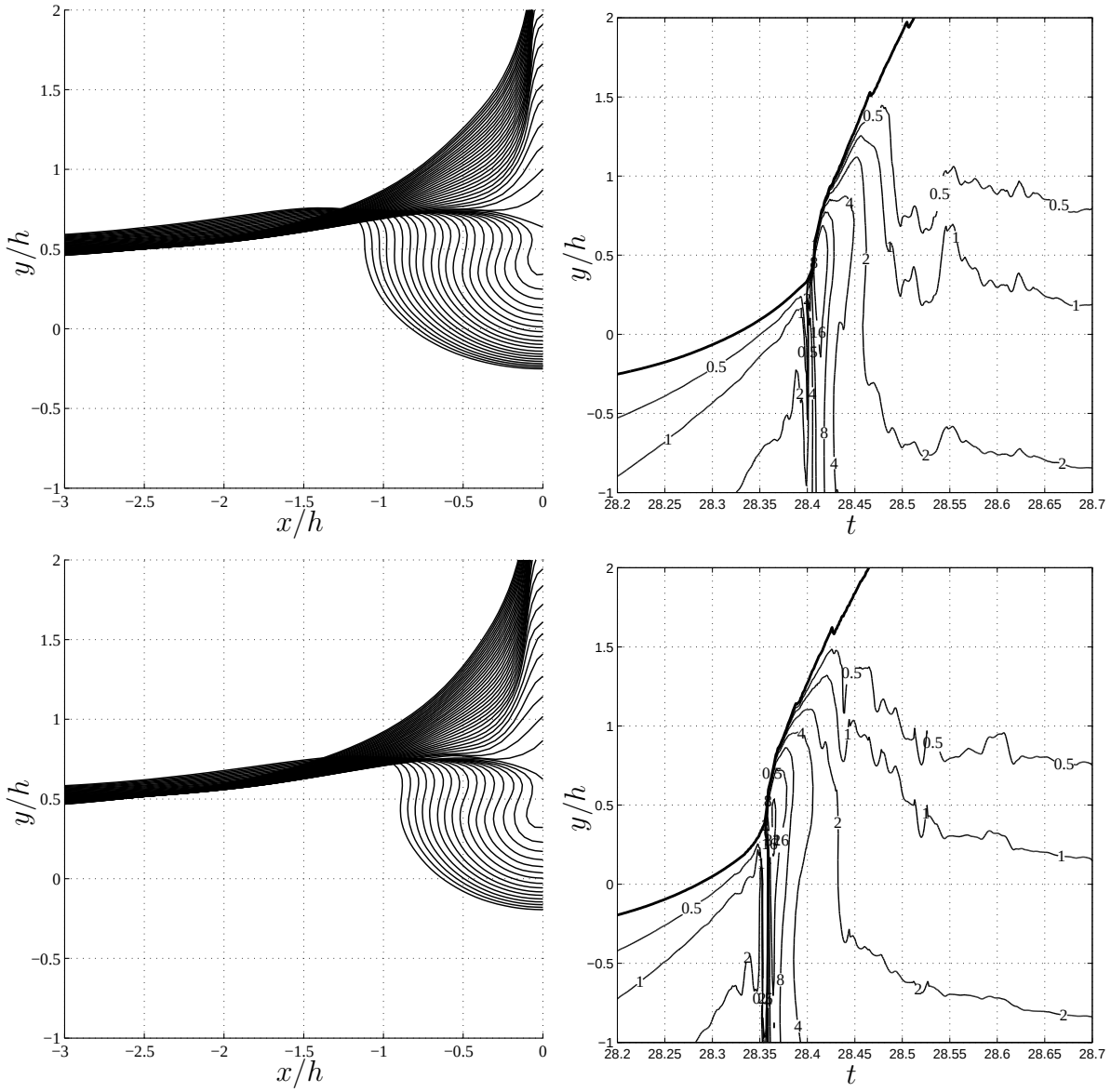

Figure 9.9: Wave impacts with the incompressible and inviscid ALE-WLS model with central flux. Left column: The free surface from time $t = 28.2$s to $t = 28.7$s with intervals of 0.01s, for the initial wave heights of $H = 1.48$m and $H = 1.51$m. Right column: The dimensionless pressure $p/(\rho g h)$ on the vertical wall for the same wave heights.

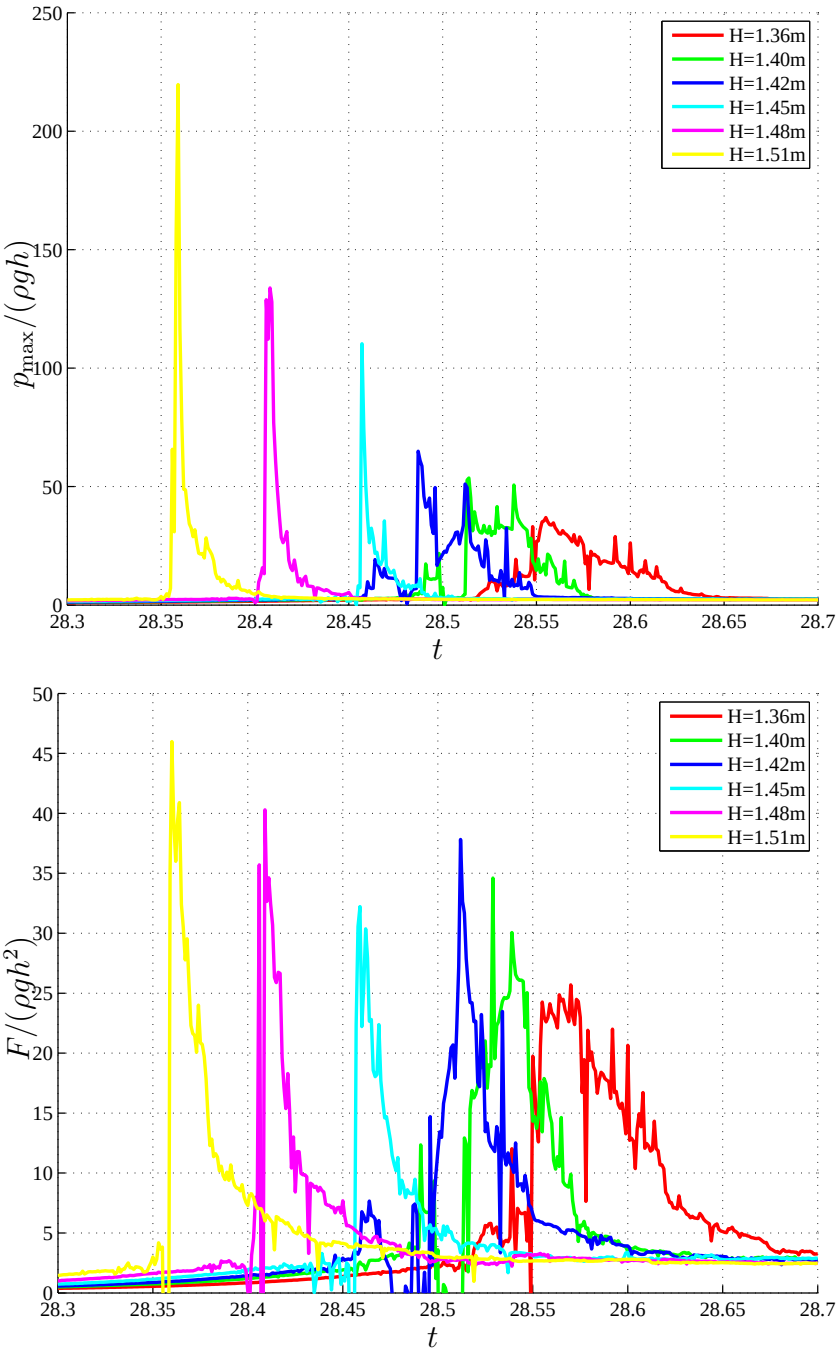

Figure 9.10: Wave impacts with the incompressible and inviscid ALE-WLS model with central flux: The maximum pressure and force on the vertical breakwater.

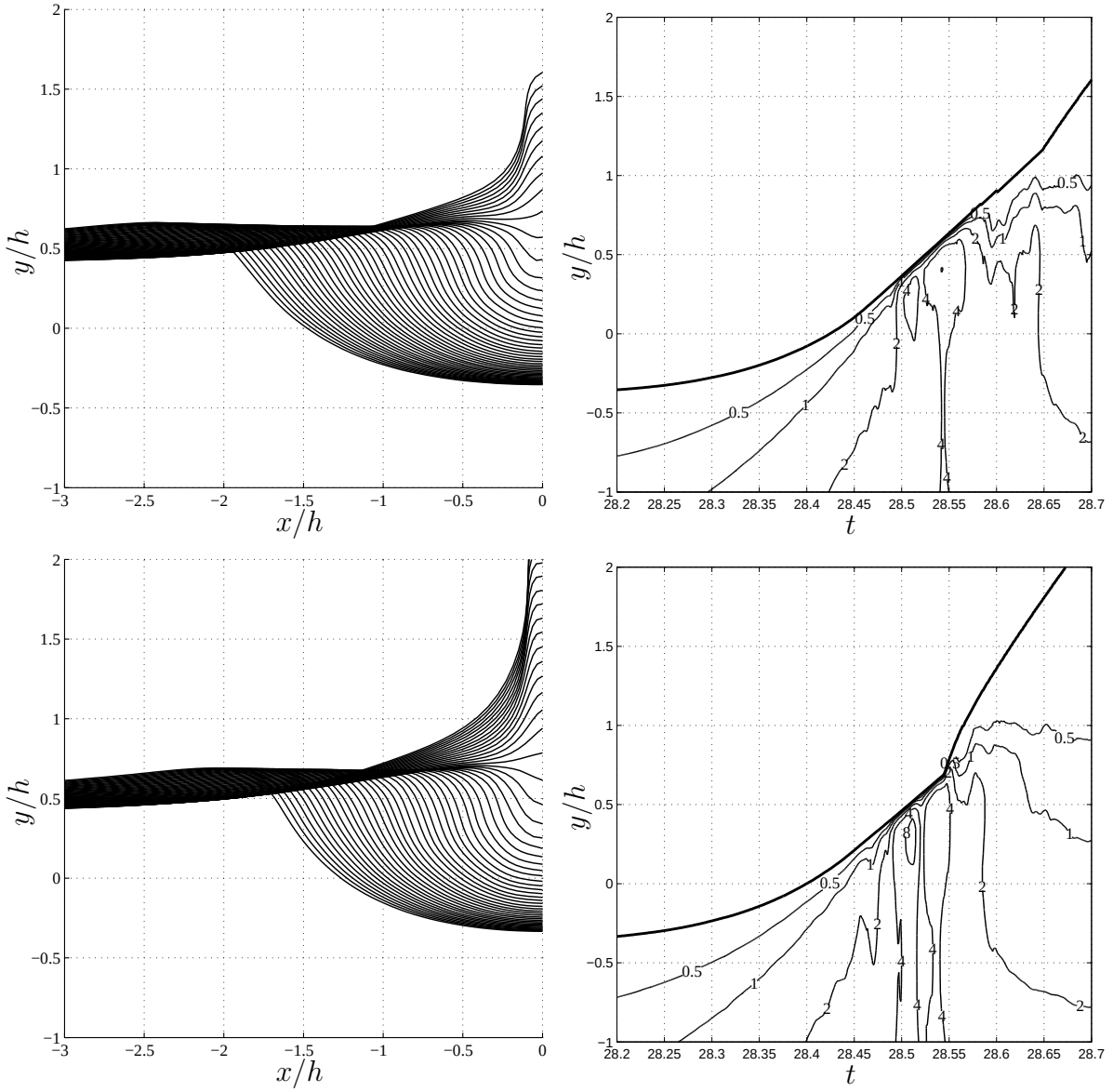

Figure 9.11: Wave impacts with the incompressible and inviscid ALE-WLS model with Rusanov flux. Left column: The free surface from time $t = 28.2$s to $t = 28.7$s with intervals of 0.01s, for the initial wave heights of $H = 1.36$m and $H = 1.40$m . Right column: The dimensionless pressure $p/(\rho g h)$ on the vertical wall for the same initial wave heights.

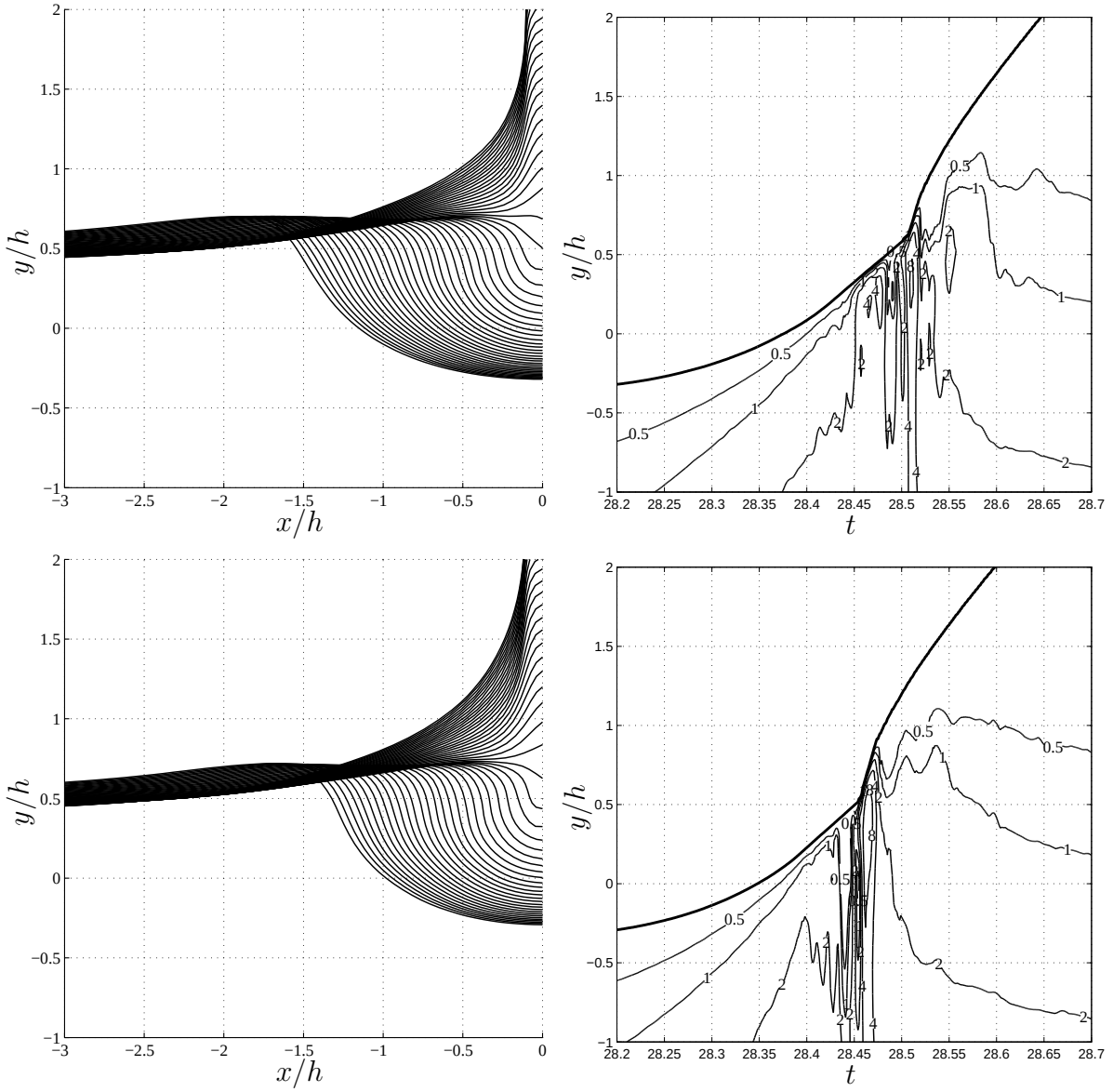

Figure 9.12: Wave impacts with the incompressible and inviscid ALE-WLS model with Rusanov flux. Left column: The free surface from time $t = 28.2$s to $t = 28.7$s with intervals of 0.01s, for the initial wave heights of $H = 1.42$m and $H = 1.45$m. Right column: The dimensionless pressure $p/(\rho g h)$ on the vertical wall for the same initial wave heights.

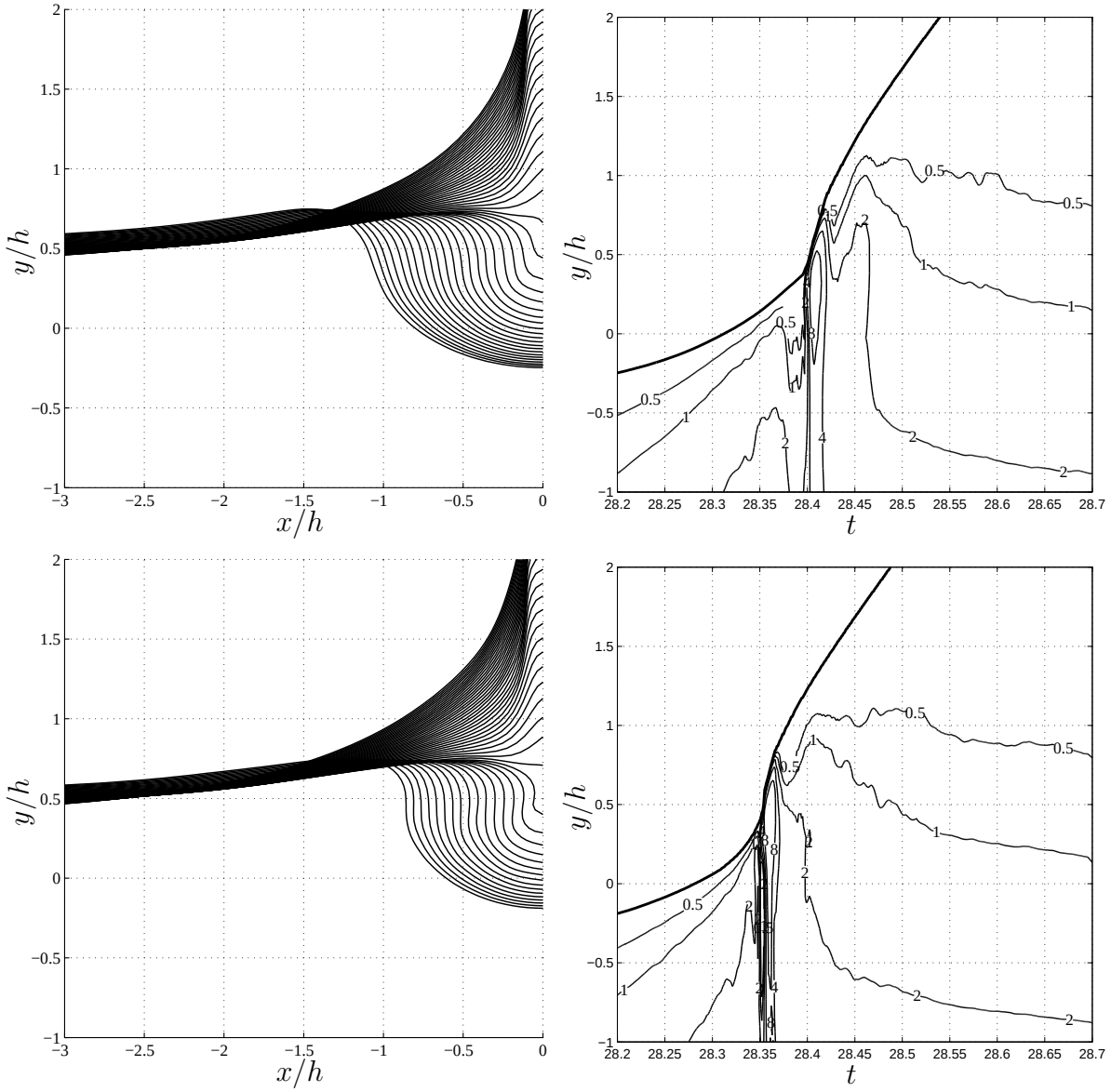

Figure 9.13: Wave impacts with the incompressible and inviscid ALE-WLS model with Rusanov flux. Left column: The free surface from time $t = 28.2$s to $t = 28.7$s with intervals of 0.01s, for the initial wave heights of $H = 1.48$m and $H = 1.51$m. Right column: The dimensionless pressure $p/(\rho g h)$ on the vertical wall for the same initial wave heights.

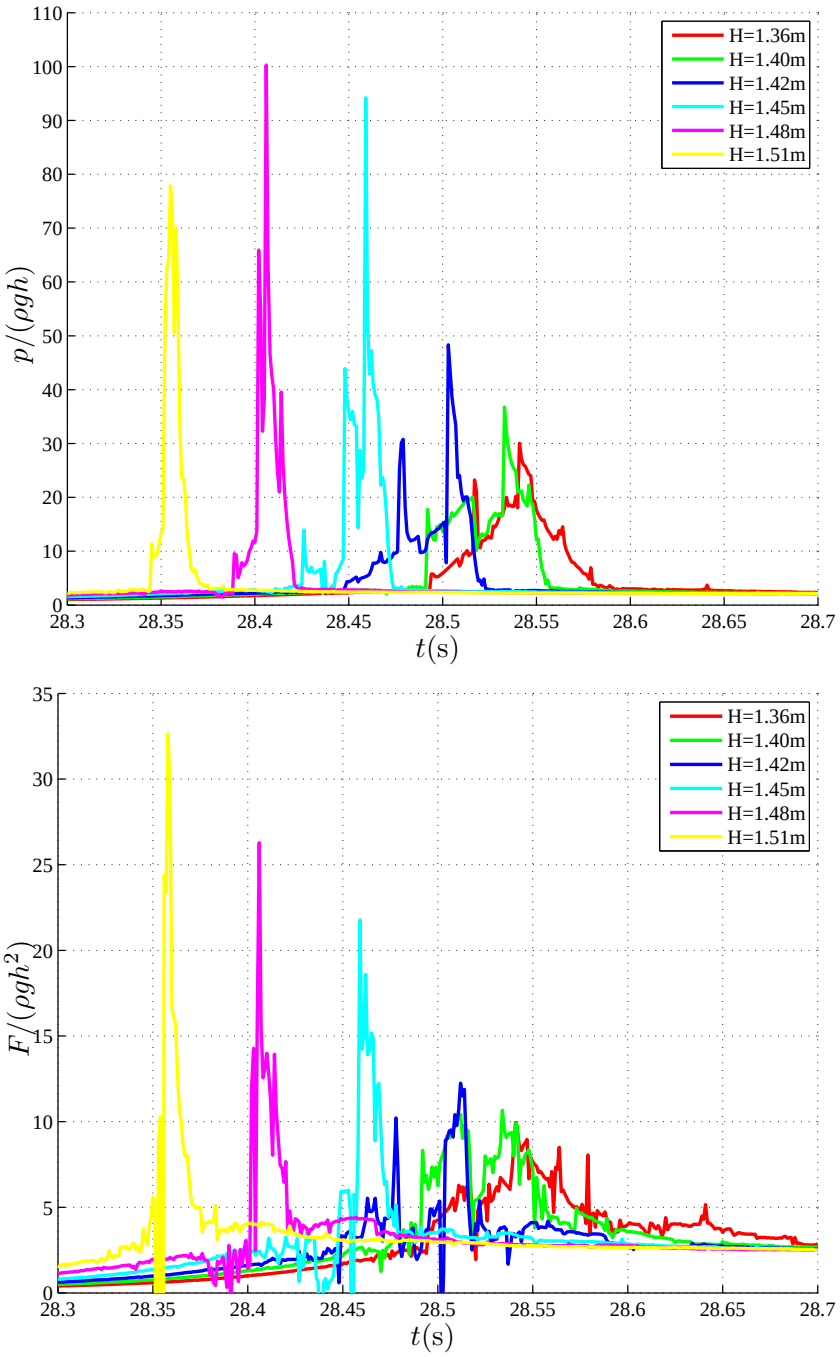

Figure 9.14: Wave impacts with the incompressible and inviscid ALE-WLS model with Rusanov flux: The maximum pressure and force on the vertical breakwater.

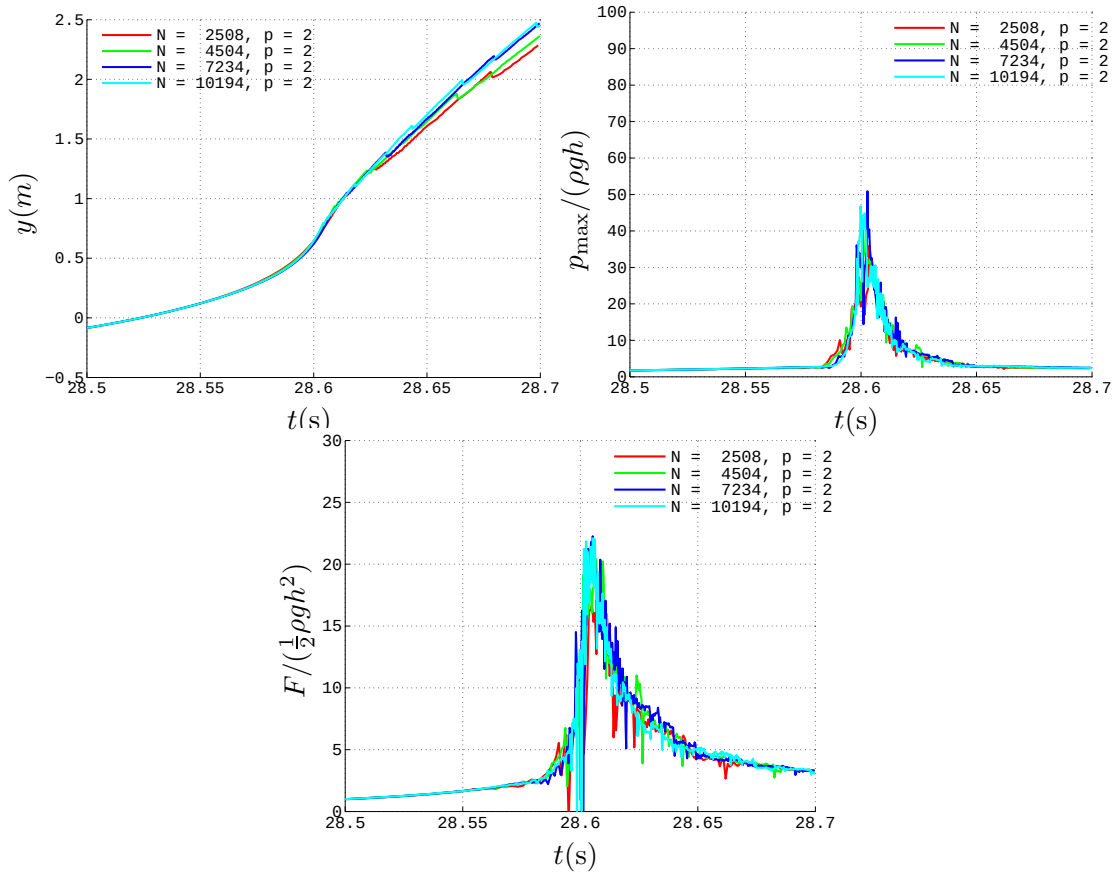

Figure 9.15: The maximum pressure at the vertical breakwater as a function of time and the force on the vertical breakwater as a function of time.

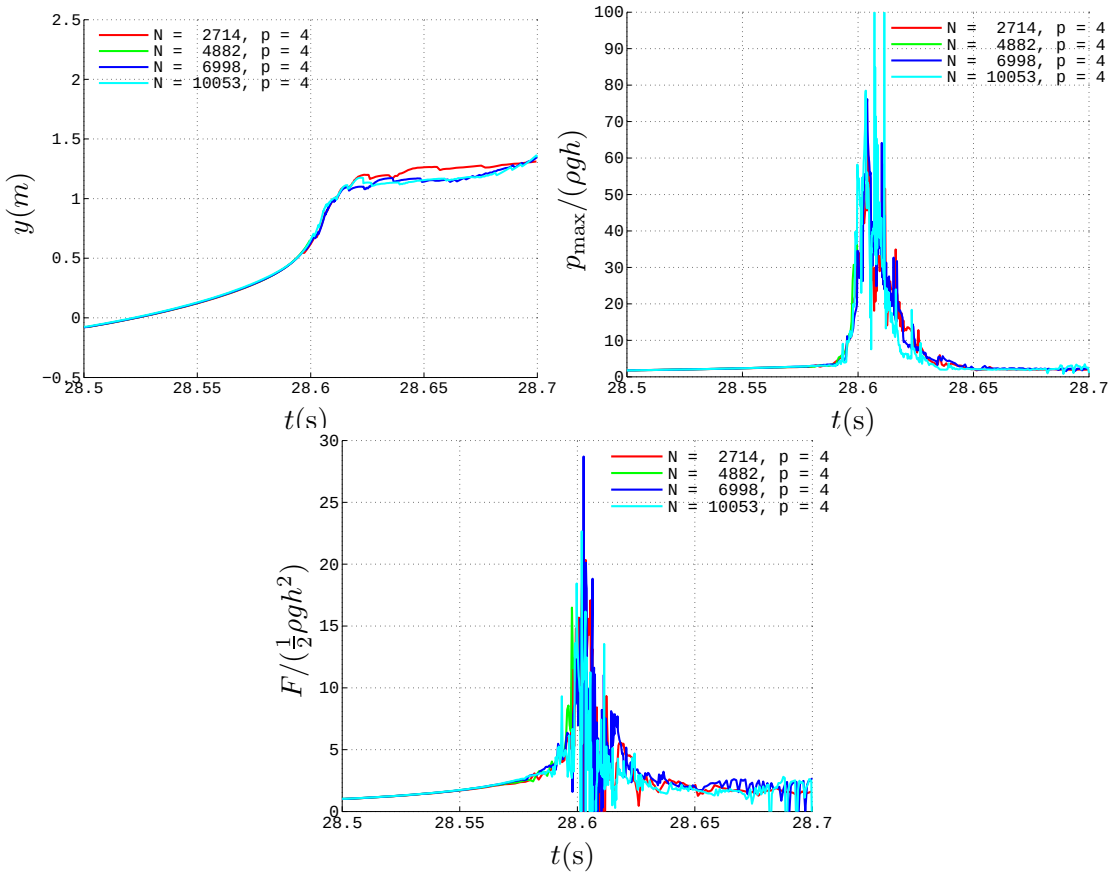

Figure 9.16: The maximum pressure at the vertical breakwater as a function of time and the force on the vertical breakwater as a function of time.

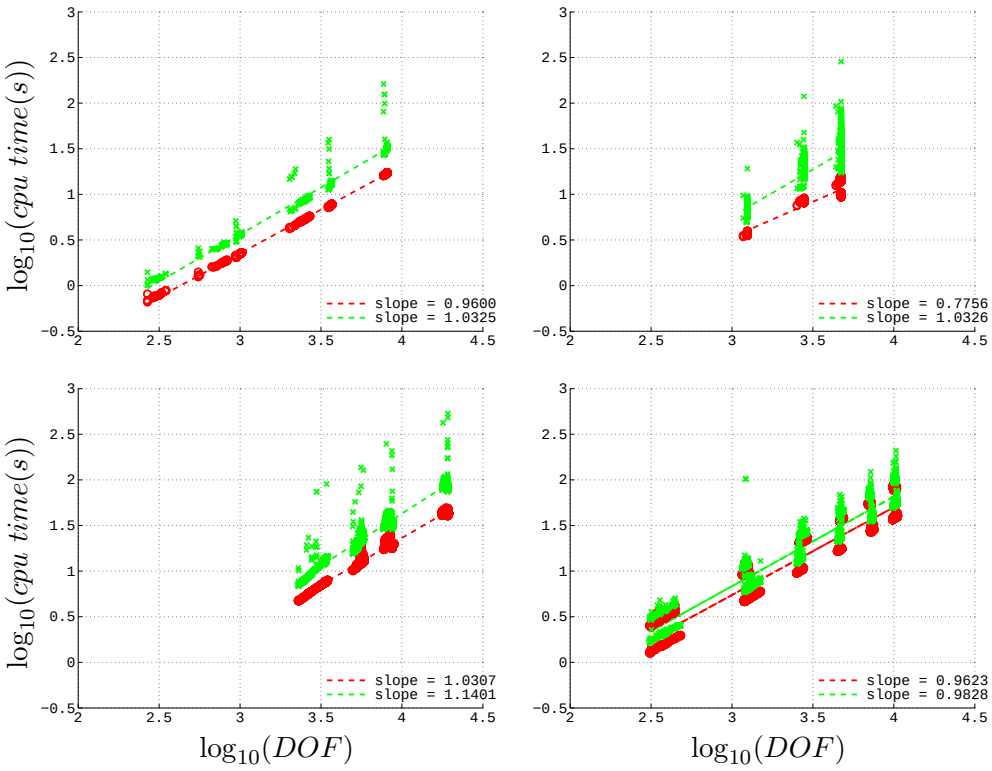
slope = 0.9600
slope = 1.0325
slope = 0.7756
slope = 1.0326
slope = 1.0307
slope = 1.1401
slope = 0.9623
slope = 0.9828
$\log_{10}(cpu\ time(s))$
$\log_{10}(DOF)$

9.3 Summary

Two free surface flow models are coupled and applied to a wave impacts on a vertical breakwater. A nonlinear potential free surface flow model with finite difference approximations is coupled with the incompressible and inviscid ALE-WLS model. The potential flow model is used to calculate smooth and non-overturning waves and the incompressible and inviscid ALE-WLS model is used to calculate overturning waves and wave impacts. The waves have been propagated from offshore to the vicinity of the breakwater by the potential flow model and the wave steepening, overturning and impacts on the wall have been calculated by the incompressible and inviscid ALE-WLS model. Two different calculations of the wave impacts are carried out: With a central flux and Rusanov flux. The kinematics of the wave overturning was captured well with the central flux, but the calculations with Rusanov flux did not calculate the kinematics satisfactorily. It is believed to be due to poor resolution of the wave impacts in both space and time. The fill distance adaptive has to be changed with some solution dependent adaptivity, to provide better resolution locally. For central flux the impact characteristics of reflective sloshing, flip through and overturning with trapped air are identified. For Rusanov flux the impact characteristic are of reflective sloshing and flip through type. The maximum pressures for the wave width height $H = 1.45$m are $\approx 1.5 - 2$ times the corresponding maximum pressures in Bredmose et al. [2009]. The maximum pressures for the wave with height $H = 1.45$m are $\approx 1 - 1.5$ times the corresponding maximum pressures in Bredmose et al. [2009].

Chapter 10

An Efficient Model for Two Dimensional Lagrangian Flow

10.1 Lagrangian Incompressible and Inviscid Free Surface Flow

Assuming the flow to be incompressible the space conservation law leads to the equation for a divergence free velocity field

$$\nabla \cdot \boldsymbol{u} = 0, \quad \boldsymbol{x} \in \Omega, \tag{10.1}$$

where $\boldsymbol{u} = \boldsymbol{u}(\boldsymbol{x}, t) \in \mathbb{R}^d$ is the fluid velocity vector, $\boldsymbol{x}$ is the position and $\Omega = \Omega(t) \in \mathbb{R}^d$ is the fluid domain. The constant d is the number of spatial dimensions. The law of conservation of momentum in a Lagrangian flame of reference is

$$\frac{d\boldsymbol{u}}{dt} = -\frac{1}{\rho}\nabla p + \boldsymbol{b}, \quad \boldsymbol{x} \in \Omega, \tag{10.2}$$

where ρ is the fluid density, p is the fluid pressure and $\boldsymbol{b}$ is the vector of accelerations due to body forces. A fluid particle follow the path

$$\frac{d\boldsymbol{x}}{dt} = \boldsymbol{u}, \quad \boldsymbol{x} \in \Omega. \tag{10.3}$$

The fluid is subject to the physical boundary conditions of a frictionless, impermeable and stationary wall and a free surface without surface tension. In the Lagrangian frame of reference the free surface moves with the flow velocity and the force balance on the free surface of an incompressible fluid gives the dynamic boundary condition

$$p = p_0, \quad \boldsymbol{x} \in \Gamma_{fs}, \tag{10.4}$$

where p_0 is the constant pressure at the free surface. The boundary condition for the frictionless, impermeable and stationary wall is

$$\boldsymbol{n} \cdot \boldsymbol{u} = 0, \quad \boldsymbol{x} \in \Gamma_{wl}, \tag{10.5}$$

where $\boldsymbol{n}$ is the outward normal to the wall and $\Gamma_{wl} \subset \partial\Omega$ is the wall part of the fluid domain boundary.

Time Integration and Mass Conservation

The temporal terms in (10.2) and (10.3) are approximated using a fourth order Runge-Kutta method

$$\boldsymbol{u}^{(k)} = \boldsymbol{u}^{(k-1)} + \sum_{l=1}^{k} \left(\beta_{kl} \Delta t \boldsymbol{f}(\boldsymbol{u}^{(l-1)}, t^{(l-1)}) \right), \quad k = 1, \ldots, r, \tag{10.6}$$

where $\boldsymbol{u}^{(k)}$ is the solution at RK stage k, $\beta_{kl},\ k, l = 1, \ldots, r$, are the coefficients defining the ERK method, Δt is the time step and $t^{(k)}$ time of the ERK stage k. The classical 4-stage method (RK4) has the coefficients

$$\boldsymbol{\beta} = \begin{bmatrix} 1/2 & 0 & 0 & 0 \\ 0 & 1/2 & 0 & 0 \\ 0 & 0 & 1 & 0 \\ 1/6 & 2/6 & 2/6 & 1/6 \end{bmatrix}. \tag{10.7}$$

The the right hand side for the equation for conservation of momentum (10.2) is

$$\boldsymbol{f}(\boldsymbol{u}^n, t^n) = -\frac{1}{\rho}(\nabla p)^n + \boldsymbol{g}, \quad i = 1, \ldots, N. \tag{10.8}$$

The equation for conservation of mass (10.1) has to be satisfied at each new Runge-Kutta stage $t^{(k)}$, hence we have a problem of constrained evolution, where the pressure $p^{(k-1)}$ is to be determined such that the velocity $\boldsymbol{u}^{(k)}$ becomes divergence free

$$\begin{aligned} \nabla \cdot \boldsymbol{u}^{(k)} = \nabla \cdot \Big(\boldsymbol{u}^{(k-1)} + \sum_{l=1}^{k} \left(\beta_{kl} \Delta t \boldsymbol{f}(\boldsymbol{u}^{(l-1)}, t^{(l-1)}) \right) \Big) = 0, \\ k = 1, \ldots, r. \end{aligned} \tag{10.9}$$

Rearranging the terms gives an equation for the pressure $p^{(k-1)}$ which ensures a divergence-free velocity $\boldsymbol{u}_h^{(k)}$

$$\begin{aligned} \nabla \cdot \nabla p^{(k-1)} = \frac{\rho}{\beta_{kk} \Delta t} \nabla \cdot \sum_{l=1}^{k-1} \Big(\alpha_{kl} \boldsymbol{u}^{(l-1)} + \beta_{kl} \Delta t \boldsymbol{f}(\boldsymbol{u}^{(l-1)}) \Big) \\ + \alpha_{kk} \boldsymbol{u}^{(k-1)} + \beta_{kk} \Delta t \boldsymbol{f}^*(\boldsymbol{u}^{(k-1)}), \\ k = 1, \ldots, r. \end{aligned} \tag{10.10}$$

where the ODE right hand side for the stage $k-1$ is

$$\boldsymbol{f}^*(\boldsymbol{u}^{(k-1)}) = \boldsymbol{f}(\boldsymbol{u}^{(k-1)}) + \frac{1}{\rho} \nabla p^{(k-1)}, \quad k = 1, \ldots, r. \tag{10.11}$$

To simplify the notation the following intermediate velocity is introduced

$$\begin{aligned} \boldsymbol{u}_h^{(k)*} = \sum_{l=1}^{k-1} \Big(\alpha_{kl} \boldsymbol{u}^{(l-1)} + \beta_{kl} \Delta t \boldsymbol{f}(\boldsymbol{u}^{(l-1)}) \Big) \\ + \alpha_{kk} \boldsymbol{u}^{(k-1)} + \beta_{kk} \Delta t \boldsymbol{f}^*(\boldsymbol{u}^{(k-1)}), \quad k = 1, \ldots, r, \end{aligned} \tag{10.12}$$

and (10.10) reduces to

$$\nabla \cdot \nabla p^{(k-1)} = \frac{\rho}{\beta_{kk}\Delta t} \nabla \cdot \boldsymbol{u}_h^{(k)*}, \quad k = 1, \ldots, r. \tag{10.13}$$

Making a numerical approximation of the divergence of the gradient $\nabla \cdot \nabla p$ which results in a stable approximation of the pressure is not a trivial task. Instead it is approximated by the Poisson equation

$$\nabla^2 p^{(k-1)} = \frac{\rho}{\beta_{kk}\Delta t} \nabla \cdot \boldsymbol{u}_h^{(k)*}, \quad k = 1, \ldots, r. \tag{10.14}$$

This Poisson equation is solved in each Runge-Kutta stage prior the update of the velocity.

Parametric Equations

By making the numerical approximation of the solution and the equations above in a time independent reference domain the efficiency and robustness of the numerical model can be improved significantly. For a thorough introduction to the transformation of functions and partial differential equations into a reference domain I refer to the book Liseikin [1999]. In the remaining part of this chapter is kept in two spatial dimensions in order to focus on the key concepts and to keep things simple. Nevertheless it is believed that the method generalize to three spatial dimensions, without increasing the computational complexity.

Assume that there exist a unique and invertible mapping from a reference domain Ξ into a the physical domain Ω with a coordinate transformation $\boldsymbol{x}(\boldsymbol{\xi}) : \Xi \to \Omega$, then the model equations can be solved on in the reference domain Ξ with respect to the independent variable $\boldsymbol{\xi} \in \mathbb{R}^d$.

The equation for conservation of mass (10.1) as a function of the reference coordinates is

$$\nabla \cdot \boldsymbol{u} = \frac{1}{\sqrt{g}} \frac{\partial}{\partial \xi^i}(u_i \sqrt{g}), \quad \boldsymbol{\xi} \in \Xi, \tag{10.15}$$

where g is the determinant of the covariant metric tensor. Likewise is the equation for conservation of momentum in the reference coordinates

$$\frac{d\boldsymbol{u}}{dt} = -\frac{1}{\rho} \frac{\partial p}{\partial \xi^i} \boldsymbol{g}^i + \boldsymbol{b}, \quad \boldsymbol{\xi} \in \Xi, \tag{10.16}$$

where the vector $\boldsymbol{g}^i$ is the contravariant basis vector. The Poisson equation (10.14) is

$$\nabla^2 p^{(k-1)} = \frac{1}{J} \frac{\partial}{\partial \xi^j} \left(J g^{ij} \frac{\partial p^{(k-1)}}{\partial \xi^i} \right) = \frac{1}{\sqrt{g}} \frac{\partial}{\partial \xi^i}(u_i^* \sqrt{g}), \quad \boldsymbol{\xi} \in \Xi, \tag{10.17}$$

where J is the Jacobian of the transformation and g^{ij} is the contravariant metric tensor.

10.2 Construction of a Parameter Domain

An introduction to methods for construction of a parametrized computational domain Ξ is given by Botsch et al. [2010].

The making of a parametrization consist of: Finding a unique and continuous mapping of the physical domain $\Omega \in \mathbb{R}^d$ into a computational domain $\Xi \in \mathbb{R}^d$

$$\boldsymbol{\xi}(\boldsymbol{x}) : \Omega \to \Xi, \tag{10.18}$$

with the Dirichlet boundary conditions

$$\boldsymbol{\xi} = \boldsymbol{\xi}_0, \quad \boldsymbol{\xi} \in \partial\Xi, \tag{10.19}$$

where the boundary condition is choose such that Ξ is convex and the two domains Ω and Ξ are topological equivalent. A possible choice of mapping is the harmonic mapping

$$\nabla^2\boldsymbol{\xi} = \mathbf{0}, \quad \boldsymbol{\xi} \in \Xi. \tag{10.20}$$

The solution to the harmonic mapping with the Dirichlet boundary condition gives the desired coordinate transformation. Instead of a analytical solution to the harmonic mapping, we will represent it as a piecewise linear solution on a triangular mesh.

Numerical Approximation of Domain and Laplacian

A set of N points are distributed over the physical domain Ω

$$\mathcal{P} = \{\boldsymbol{x}_i : i = 1, \ldots, N \wedge \boldsymbol{x}_i \in \Omega\}. \tag{10.21}$$

such that the triangulation of the point set gives an approximation of the physical domain Ω by a conforming triangular mesh

$$\Omega \approx \Omega_h = \mathcal{T}(\mathcal{P}) = \bigcup_{i=1}^{N_T} T_i. \tag{10.22}$$

where T_i is a straight-sided triangles. A subset of the point set $\mathcal{P}$ is located on the boundary of the physical domain

$$\mathcal{P}_\Gamma = \{\boldsymbol{x}_i : \boldsymbol{x}_i \in \mathcal{P}_\Omega \wedge \boldsymbol{x}_i \in \Gamma\}. \tag{10.23}$$

Based on the triangular mesh $\mathcal{T}(\mathcal{P})$ and a discrete approximation the harmonic map a unique, continuous and piecewise linear mapping $\boldsymbol{\xi}(\boldsymbol{x}) : \mathcal{T} \to \Xi$ can be found. Two very simple approximations Laplace operator in (10.20) are the uniform graph Laplacian and the cotangent formula, both described in Botsch et al. [2010]. The uniform graph Laplacian is

$$\nabla^2 f(\boldsymbol{x}_i) \approx \frac{1}{|\mathcal{N}_i|} \sum_{j \in \mathcal{N}_i} (f(\boldsymbol{x}_j) - f(\boldsymbol{x}_i)), \quad \boldsymbol{x}_i \in \mathcal{P}_\Gamma, \tag{10.24}$$

where $\mathcal{N}_i$ is the neighbourhood of the point $\boldsymbol{x}_i$ in the triangle mesh $\mathcal{T}(\mathcal{P})$. This Laplacian is very simple and efficient to compute, but suffers from poor accuracy. The cotangent formula is based on a mixed finite element and finite volume approximation of the Laplacian

$$\nabla^2 f(\boldsymbol{x}_i) \approx \frac{1}{2A_i} \sum_{j \in \mathcal{N}_i} (\cot \alpha_{ij} + \cot \beta_{ij})(f(\boldsymbol{x}_j) - f(\boldsymbol{x}_i)), \quad \boldsymbol{x}_i \in \mathcal{P}_\Gamma, \tag{10.25}$$

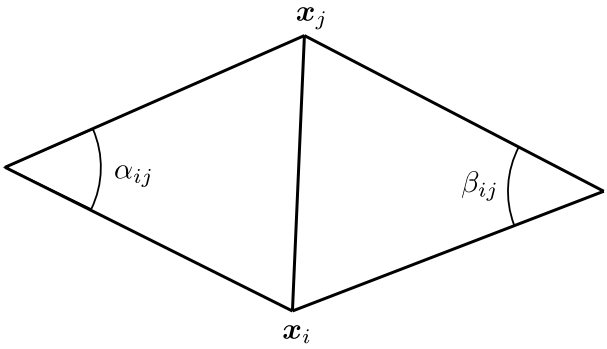

Figure 10.1: The triangles on each side of the edge going from $\boldsymbol{x}_i$ to $\boldsymbol{x}_j$ and the angles opposite of this edge, which are used in the cotangent formula (10.25).

where A_i is the area covered by the triangles in the neighbourhood $\mathcal{N}_i$ and the angles α_{ij} and β_{ij} are shown in figure 10.1. While this formula is more accurate it can cause triangles to flip, e.g. when used for computations of parametrization of meshes, if the sum of the angles $\cot\alpha_{ij} + \cot\beta_{ij} > \pi$. It is therefore important that the coefficients of the approximations of the Laplacian gives a convex combination mapping. Using one of these approximations of the Laplacian and the Dirichlet boundary conditions (10.19) the position of the points $\boldsymbol{\xi}_i,\ i = 1, \ldots, N$ in the parameter domain Ξ can be solved for. This point set in the parameter domain is resulting from the constructed mapping is $\boldsymbol{P}_\Xi = \{\boldsymbol{\xi}_i :\ i = 1, \ldots, N\ \wedge\ \boldsymbol{\xi}_i = \boldsymbol{\xi}(\boldsymbol{x}_i)\ \forall \boldsymbol{x}_i \in \mathcal{P}\}$.

10.3 Numerical Approximation of Solution and Equations

The solutions for the position $\boldsymbol{x}$, velocity $\boldsymbol{u}$ and pressure p are to be approximated numerically in the parameter domain, along with the equations for the evolution of the position (10.3), the equation for the conservation of momentum (10.16) and the Poisson equation for the pressure (10.17).

The solution for the position is approximated the following local vector polynomials in the neighbourhoods $\Xi(\boldsymbol{\xi}_i) \subset \Xi$ of each point in $\mathcal{P}_\Xi$

$$\boldsymbol{x}_h = \boldsymbol{x}_h(\boldsymbol{\xi}, t) = \sum_{|\boldsymbol{\alpha}|=0}^{\boldsymbol{\alpha}_{\max}} \boldsymbol{a}_{\boldsymbol{\alpha}}(t)(\boldsymbol{\xi} - \boldsymbol{\xi}_i)^{\boldsymbol{\alpha}}, \quad \boldsymbol{\xi} \in \Xi(\boldsymbol{\xi}_i), \tag{10.26}$$

where multi-index notation is used and $\boldsymbol{a}_{\boldsymbol{\alpha}}(t)$ is the vector of coefficients to the $\boldsymbol{\alpha}$ term in the polynomial. The solution for the velocity is approximated the similar local polynomials

$$\boldsymbol{u}_h = \boldsymbol{u}_h(\boldsymbol{\xi}, t) = \sum_{|\boldsymbol{\alpha}|=0}^{\boldsymbol{\alpha}_{\max}} \boldsymbol{b}_{\boldsymbol{\alpha}}(t)(\boldsymbol{\xi} - \boldsymbol{\xi}_i)^{\boldsymbol{\alpha}}, \quad \boldsymbol{\xi} \in \Xi(\boldsymbol{\xi}_i), \tag{10.27}$$

where $\boldsymbol{b}_{\boldsymbol{\alpha}}(t)$ is the vector of coefficients to the $\boldsymbol{\alpha}$ term. Finally the pressure is also

approximated by a local scalar polynomial

$$p_h = p_h(\boldsymbol{\xi}, t) = \sum_{|\boldsymbol{\alpha}|=0}^{\boldsymbol{\alpha}_{\max}} a_{\boldsymbol{\alpha}}(t)(\boldsymbol{\xi} - \boldsymbol{\xi}_i)^{\boldsymbol{\alpha}}, \quad \boldsymbol{\xi} \in \Xi(\boldsymbol{\xi}_i), \tag{10.28}$$

where $a_{\boldsymbol{\alpha}}(t)$ is the scalar coefficient to the $\boldsymbol{\alpha}$ term.

The solution approximations above are inserted in the equations (10.3), (10.16) and (10.17)

$$\frac{d\boldsymbol{x}_h}{dt} = \boldsymbol{u}_h, \quad \boldsymbol{\xi} \in \Xi, \tag{10.29}$$

$$\frac{d\boldsymbol{u}_h}{dt} = -\frac{1}{\rho}\frac{\partial p_h}{\partial \xi^m}\boldsymbol{g}^m + \boldsymbol{b}, \quad \boldsymbol{\xi} \in \Xi, \tag{10.30}$$

$$\frac{1}{J}\frac{\partial}{\partial \xi^j}\left(Jg^{mj}\frac{\partial p_h^{(k-1)}}{\partial \xi^m}\right) = \frac{1}{\sqrt{g}}\frac{\partial}{\partial \xi^m}(u^*_{h,m}\sqrt{g}), \quad \boldsymbol{\xi} \in \Xi, \tag{10.31}$$

and the residual of these equations are required to be minimum at the N points in $\mathcal{P}_\Xi$

$$\frac{d\boldsymbol{x}_i}{dt} = \boldsymbol{u}_i, \ i \in [1, N], \tag{10.32}$$

$$\frac{d\boldsymbol{u}_i}{dt} = -\frac{1}{\rho}\left(\frac{\partial p_h}{\partial \xi^m}\boldsymbol{g}^m\right)_i + \boldsymbol{b}, \ i \in [1, N], \tag{10.33}$$

$$\left(\frac{1}{J}\frac{\partial}{\partial \xi^j}\left(Jg^{mj}\frac{\partial p_h^{(k-1)}}{\partial \xi^m}\right)\right)_i = \left(\frac{1}{\sqrt{g}}\frac{\partial}{\partial \xi^m}(u^*_{i,m}\sqrt{g})\right)_i, \ i \in [1, N], \tag{10.34}$$

where $\boldsymbol{x}_i = \boldsymbol{x}_h(\boldsymbol{\xi}_i, t)$, $\boldsymbol{u}_i = \boldsymbol{u}_h(\boldsymbol{\xi}_i, t)$ and $p_i = p_h(\boldsymbol{\xi}_i, t)$. All the derivatives in the equations above are with respect to the $\boldsymbol{\xi}$ coordinate and they are approximated using the weighted least squares method described in chapter 4.

10.4 Deforming Elliptical Drop

The performance of the above described approximation and solution to incompressible and inviscid Lagrangian flow using a computational domain is demonstrated with application to the deforming elliptical drop test case.

The initial condition for the fluid domain $\Omega(0)$ is a circular drop radius $R = 1m$ with its center in $\boldsymbol{x}_0 = [0, 0]^T$ and the initial condition for the velocity is a linear function function of $\boldsymbol{x}$

$$\boldsymbol{u}(\boldsymbol{x}) = \begin{bmatrix} -100.0x_1 \\ 100.0x_2 \end{bmatrix}, \quad \boldsymbol{x} \in \Omega(0), \tag{10.35}$$

The fluid domain $\Omega(t)$ evolves in time to a ellipse with radii a and b. For an incompressible flow the product of $\omega = ab$ remains constant and the temporal evolution of the radius a is described by the two coupled ordinary differential equations

$$\frac{dA}{dt} = \frac{A^2(a^4 - \omega^4)}{a^4 + \omega^4}, \tag{10.36}$$

$$\frac{da}{dt} = -aA. \tag{10.37}$$

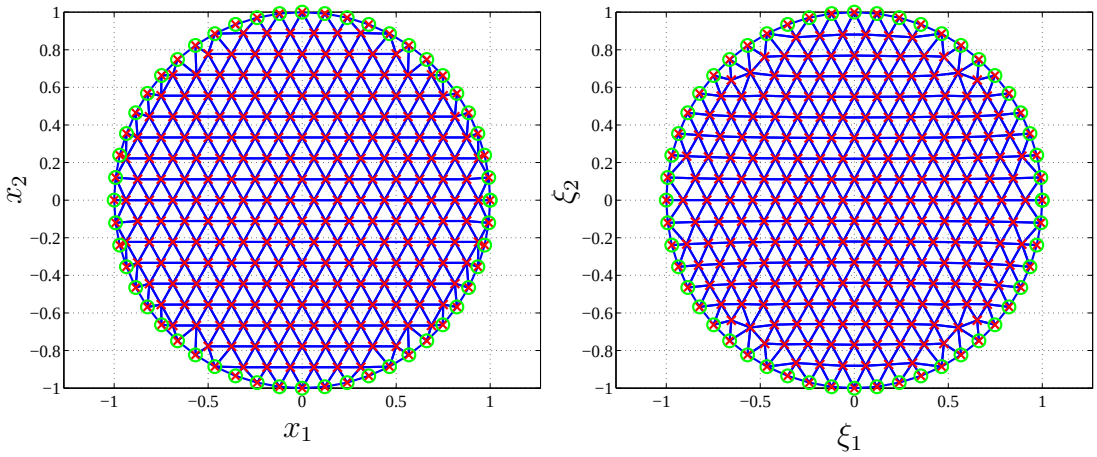

Figure 10.2: The left figure shows the initial positions for the points $\boldsymbol{x}_i,\ i = 1, \ldots, N$ in the physical domain and the figure on the right shows position of the corresponding points $\boldsymbol{\xi}_i,\ i = 1, \ldots, N$ in the computational domain. The red crosses marks the points, the blue lines show the triangle mesh and the green circles mark the boundary points.

These equations are solved numerically using a RK45 method with the initial condition

$$a = R, \quad t = 0, \tag{10.38}$$

$$\begin{aligned} A &= -a\frac{da}{dt} \\ &= -R \cdot u(R, 0), \quad t = 0, \end{aligned} \tag{10.39}$$

in the time interval $t \in [0, 0.0076]$, the same time interval as the used for the deforming elliptical drop simulation in Ferrari et al. [2009].

The initial condition for the points in the physical domain Ω and the computational domain Ξ are seen in figure 10.2 with $N = 268$ points. The chosen initial point configuration in the physical domain is hexagonal lattice inside the domain and equidistant distribution points along the boundary. The point distribution in the computational domain is obtained by solving the Laplace equation for the inner points, using the uniform graph Laplacian 10.24 approximation, with the boundary positions of the physical domain as Dirichlet boundary condition.

The flow has been evolved until the final time at $t = 0.0076s$ and the final solution is seen in figure 10.3. Judging from these figures the result seems satisfactory.

The CPU time spend on the this calculation is $\approx 4s$ for a well implemented Matlab code. The same simulation based on the earlier described WLS/GFPM method takes $\approx 28s$ also in a Matlab code.

10.5 Summary

A model for Lagrangian flow based on computations in a time independent computational domain has been presented. For a small simulation of a deforming elliptical drop very good results has been obtained and a significant speed up for a single case has been reported.

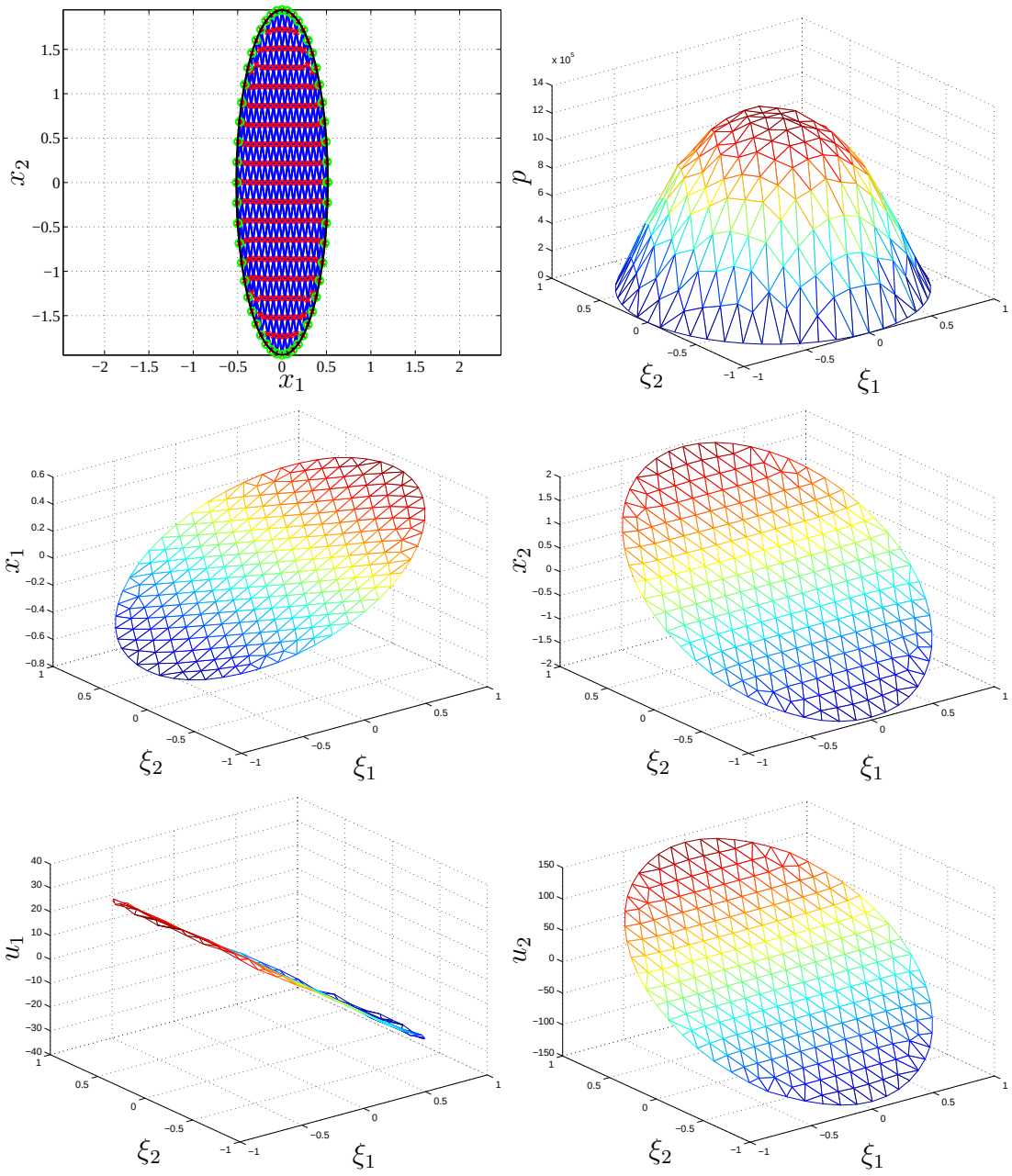

Figure 10.3: The final solution for the deforming liquid drop. Top left: The point positions with red crosses, the boundary points with green circles and the triangle mesh in blue. The black line shows the theoretical position of the free surface at the time $t = 0.0076s$. The rest of the figures are the solutions in computational domain. Top right: pressure p, middle left: horizontal position x_1, middle right: vertical position x_2, bottom left: horizontal velocity u_1 and bottom right: vertical velocity u_2.

A possible development of the parametric domain is to make local parameter spaces for each point. The global parametric domain is complicated, because it has to be topological equivalent to the global physical domain. Hence if the topology of the physical domain changes, then the parametric domain has to be recalculated with the same topology as the physical domain. To do this one needs to make a decision on how to construct the parametric domain and this seems like a complicated task. If local parametric domains are constructed for each point, which are locally topological equivalent, then these are independent of the global topology and would not require updating when the global topology changes. An example of local parameter spaces is found in Dumbser et al. [2008] where it is applied on the context of WENO reconstruction in a mixed FV and DGFEM method.

This method can possible be generalized and it need to be based on an flexible choice of matching equivalent topologies between the physical domain and the computational domain.

Chapter 11

Conclusion

The ambitious purpose in this project is to make an accurate, robust, geometrically flexible and efficient numerical model for calculation of forces from breaking wave impacts on structures in the marine environment. The presented incompressible and inviscid ALE-WLS model gives fairly accurate results when applied to standard validation cases: deforming elliptical drop, small amplitude standing wave and the dam break problem. For application to breaking wave impacts on a vertical breakwater the model needs refinement before it can be claimed to be accurate. The model is robust for simple flows such as the elliptical drop and small amplitude standing waves, but for very nonlinear flows, dam break and breaking wave impacts, the model breaks down after some time due to ill-conditioning of the WLS Taylor expansions matrix. The model is geometrically flexible, because it is based on calculation of WLS derivatives and a BFS data structure. The efficiency is the main challenge for this model. The inversion of the WLS and GFPM matrices are very time consuming. The components of the model scale with $\mathcal{O}(N\log(N))$ or $\mathcal{O}(N)$, but still the model is computationally expensive. The focus has been more on improvement of accuracy and robustness of the model than its efficiency.

It has been necessary to make a substantial amount of development to calculate breaking wave impacts with the incompressible and inviscid ALE-WLS model. Some of the important developments in this project are:

- The presentation of the incompressible and inviscid Euler equations in the ALE moving frame of reference.
- The enforcement of mass conservation combined with explicit Runge-Kutta time-integration.
- The combination of WLS method with approximate Riemann solvers.
- A generalization of the FPM method to higher-order approximations of elliptical PDEs with inhomogeneous Dirichlet or Neumann boundary conditions on unstructured point sets.
- The modified BFS data structure that enables a search for stencils that respect the topology of the fluid domain.

- The fluid-wall and fluid-fluid intersection algorithm and subsequent topology update of boundary and BFS data structures.
- The removal of the singularity at the contact point of the wet-dry interface.
- The applicability of the incompressible and inviscid ALE-WLS model to both small amplitude linear waves and nonlinear breaking waves.
- The one-way coupling of the potential flow finite difference model by Engsig-Karup et al. [2009] with the incompressible and inviscid ALE-WLS model.
- The comparison of breaking wave impacts calculated with a compressible two-phase model by Bredmose et al. [2009] with the incompressible and inviscid ALE-WLS model.

The incompressible and inviscid ALE-WLS model has successfully been applied to calculation of breaking wave impacts on a vertical breakwater. These calculation needs to be refined in both time and space. This means that the point adaptivity method has to be coupled to the error approximation, gradients or curvatures of the solution.It has nevertheless been possible to calculated maximum pressures and forces on the vertical breakwater that are compare able to Bredmose et al. [2009]. An interesting perspective of this is to identify the flow regimes where incompressible and inviscid single-phase models are applicable to the breaking wave impact calculations. In three dimensional calculations the likelihood of trapping large air pockets are smaller than in two dimensional calculations. Thus the incompressible model can be even more useful in three dimensional calculations.

11.1 Future Work

The presented incompressible and inviscid ALE-WLS model is not yet robust and efficient enough to be applied as a tool for a CFD engineer.

Further development of this incompressible and inviscid single-phase type model should done be to enhance the accuracy, robustness and efficiency of the numerical approximations. The accuracy study should include the physical approximations and development of engineering guidelines for the applicability of the following types of models to breaking wave impacts:

- Nonlinear potential free surface flow, single phase.
- Incompressible and inviscid or viscous flow, single or multi-phase.
- Compressible and inviscid or viscous flow, single or multi-phase.

This combined with further investigations of the role of entrained and trapped air in both two and three dimensional breaking wave impact calculations.

Even though the WLS method gives geometric flexibility and has the potential for higher-order accuracy it is sensitive to the point distribution and the Taylor expansion matrix can (easily) become ill-conditioned. An interesting path would be to exchange

the polynomial representation of the solutions with an orthogonal polynomial basis and apply CGFEM, DGFEM or SEM type methods for the solution of ALE compressible or incompressible Navier-Stokes equations such as done by Deville et al. [2002] and Kopriva [2009]. The fluid domain approximation could be improved by these methods with applications unstructured quadrilateral and/or triangle meshes with curved boundaries. The DGFEM method has been successfully applied to free surface flow and fluid structure interaction by Engsig-Karup et al. [2008].

The point adaptivity based on the geometric fill-distance error indicator tends to give a uniform distribution of the calculation points. To make real multiscale calculations the adaptivity should be coupled to the solution and allow for non-uniform point distributions. Structured and unstructured grid generation Liseikin [1999] and FEM type methods can perhaps provide an improved basis for adaptivity methods.

Appendix A

Multi Index Notation

A multi index is a n-dimensional vector of natural numbers

$$\boldsymbol{\alpha} = \begin{bmatrix} \alpha_1 \\ \alpha_2 \\ \vdots \\ \alpha_n \end{bmatrix} \quad \in \mathbb{N}_0^n. \tag{A.1}$$

The $\boldsymbol{\alpha}$ power of a vector of real numbers $\mathbf{x} \in \mathbb{R}^n$ in the multi-index notation is

$$\mathbf{x}^{\boldsymbol{\alpha}} = x_1^{\alpha_1} \cdot x_2^{\alpha_2} \dots x_n^{\alpha_n}. \tag{A.2}$$

The modulus or absolute value of a multi-index vector is

$$|\boldsymbol{\alpha}| = \alpha_1 + \alpha_2 + \cdots \alpha_n, \tag{A.3}$$

and the factorial is

$$\boldsymbol{\alpha}! = \alpha_1! \cdot \alpha_2! \cdots \alpha_n!. \tag{A.4}$$

The partial derivative operator in the multi-index notation is

$$D^{\boldsymbol{\alpha}} = \frac{\partial^{|\boldsymbol{\alpha}|}}{\partial_{x_1}^{\alpha_1} \partial_{x_2}^{\alpha^2} \dots \partial_{x_n}^{\alpha^n}}. \tag{A.5}$$

Scaling the $\boldsymbol{\alpha}$ power of a vector with a positive real number $\varepsilon \in \mathbb{R}^+$ gives

$$\mathbf{x}^{\boldsymbol{\alpha}} = \varepsilon^{|\boldsymbol{\alpha}|} \left(\frac{1}{\varepsilon} \mathbf{x} \right)^{\boldsymbol{\alpha}}. \tag{A.6}$$

M. Antuono, A. Colagrossi, S. Marrone, and C. Lugni. Propagation of gravity waves through an SPH scheme with numerical diffusive terms. *Computer Physics Communications*, 182(4):866–877, April 2011.

H. B. Bingham and H. Zhang. On the accuracy of finite-difference solutions for nonlinear water waves. *Journal of Engineering Mathematics*, 58(1-4):211–228, 2007.

M. Botsch, L. Kobbelt, M. Pauly, Alliez P., and B. Levy. *Polygon Mesh Processing*. A K Peters, Ltd., 2010.

H. Bredmose, D. H. Peregrine, and G. N. Bullock. Violent breaking wave impacts. Part 2: modelling the effect of air. *Journal of Fluid Mechanics*, 641:389–430, December 25 2009. ISSN 0022-1120. doi: 10.1017/S0022112009991571.

H. Bredmose, A. Hunt-Raby, R. Jayaratne, and G. N. Bullock. The ideal flip-through impact: experimental and numerical investigation. *Journal of Engineering Mathematics*, 67(1-2):115–136, June 2010. ISSN 0022-0833. doi: 10.1007/s10665-009-9354-3.

Henrik Bredmose and Niels G. Jacobsen. Breaking Wave Impacts on Offshore Wind Turbine Foundations: Focused Wave Groups and CFD. In *29th International Conference on Ocean, Offshore and Arctic Engineering 2010, vol. 3*, pages 397–404, 2010.

G. N. Bullock, C. Obhrai, D. H. Peregrine, and H. Bredmose. Violent breaking wave impacts. Part 1: Results from large-scale regular wave tests on vertical and sloping walls. *Coastal Engineering*, 54(8):602–617, AUG 2007. ISSN 0378-3839. doi: 10.1016/j.coastaleng.2006.12.002.

E.S. Chan and W.K. Melville. Deep-Water Plunging Wave Pressures on a Vertical Plane Wall. *Proceedings of the Royal Society of London Series A-Mathematical Physical and Engineering Sciences*, 417(1852):95–131, May 9 1988. ISSN 1364-5021. doi: 10.1098/rspa.1988.0053.

Hubert Chanson. A Simple Solution of the Laminar Dam Break Wave. *Journal of Applied Fluid Mechanics*, 1(1):1–10, 2008.

A. Colagrossi and M. Landrini. Numerical simulation of interfacial flows by smoothed particle hydrodynamics. *Journal of Computational Physics*, 191(2):448–475, November 1 2003.

Thomas H. Cormen, Charles E. Leiserson, Ronald L. Rivest, and Clifford Stein. *Introduction to Algorithms*. Massachusetts Institute of Technology, 2009.

R. A. Dalrymple and B. D. Rogers. Numerical modeling of water waves with the SPH method. *Coastal Engineering*, 53(2-3, SI):141–147, FEB 2006.

Mark de Berg, Otfried Cheong, Marc van Kreveld, and Mark Overmars. *Computational Geometry*. Springer-Verlag Berlin Heidelberg, 2008.

M. O. Deville, P. F. Fischer, and E. H. Mund. *High-Order Methods for Incompressible Fluid Flow*. Cambridge University Press, 2002.

J. Donea, S. Guiliani, and J. P. Halleux. An Arbitrary Lagrangian-Eulerian Finite-Element Method for Transient Dynamic Fluid Structure Interactions. *Computer Methods in Applied Mechanics and Engineering*, 33(1-3):689–723, 1982.

Michael Dumbser. A simple two-phase method for the simulation of complex free surface flows. *Computer Methods in Applied Mechanics and Engineering*, 200(9-12):1204–1219, 2011. ISSN 0045-7825. doi: 10.1016/j.cma.2010.10.011.

Michael Dumbser, Dinshaw S. Balsara, Eleuterio F. Toro, and Claus-Dieter Munz. A unified framework for the construction of one-step finite volume and discontinuous Galerkin schemes on unstructured meshes. *Journal of Computational Physics*, 227 (18):8209–8253, September 10 2008. ISSN 0021-9991. doi: 10.1016/j.jcp.2008.05.025.

Marco Ellero, Mar Serrano, and Pep Espanol. Incompressible smoothed particle hydrodynamics. *Journal of Computational Physics*, 226(2):1731–1752, October 1 2007. ISSN 0021-9991. doi: 10.1016/j.jcp.2007.06.019.

A. P. Engsig-Karup. *Unstructured nodal DG-FEM solution of high-order Boussinesq-type equations*. PhD thesis, 2006.

A. P. Engsig-Karup, H. B. Bingham, and O. Lindberg. An efficient flexible-order model for 3d nonlinear water waves. *Journal of Computational Physics*, 228:2100–2118, 2009.

A. P. Engsig-Karup, M. G. Madsen, and S. L. Glimberg. A massively parallel gpu-accelerated model for analysis of fully nonlinear free surface waves. *Interternational Journal of Numerical Methods in Fluids*, 2011. doi: 10.1002/fld.2675.

Allan P. Engsig-Karup, Jan S. Hesthaven, Harry B. Bingham, and T. Warburton. DG-FEM solution for nonlinear wave-structure interaction using Boussinesq-type equations. *Coastal Engineering*, 55(3):197–208, March 2008.

J. D. Fenton. The numerical solution of steady water wave problems. *Computer and Geosciences*, 14(3):357–368, 1988.

A. Ferrari, M. Dumbser, E. F. Toro, and A. Armanini. A new 3D parallel SPH scheme for free surface flows. *Computers & Fluids*, 38(6):1203–1217, 2009.

Joel H. Ferziger and Milovan Peric. *Computational Methods for Fluid Dynamics*. Springer-Verlag Berlin Heidelberg New York, 3 edition, 2002.

F. H. Harlow and J. E. Welch. Numerical Calculation of Time-Dependent Viscous Incompressible Flow of Fluid with Free Surface. *Physics of Fluids*, 8(12):2182–&, 1965.

C. W. Hirt and B. D. Nichols. Volume of Fluid (VOF) Method for the Dynamics of Free Boundaries. *Journal of Computational Physics*, 39(1):201–225, 1981. ISSN 0021-9991. doi: 10.1016/0021-9991(81)90145-5.

C. Huh and L. E. Scriven. Hydrodynamic Model of Steady Movement of a Solid/Liquid/Fluid Contact Line. *Journal of Colloid and Interface Science*, 35(1):85–&, 1971. ISSN 0021-9797. doi: 10.1016/0021-9797(71)90188-3.

S. R. Idelsohn, E. Onate, and F. Del Pin. The particle finite element method: a powerful tool to solve incompressible flows with free-surfaces and breaking waves. *International Journal for Numerical Methods in Engineering*, 61(7):964–989, October 21 2004. ISSN 0029-5981. doi: 10.1002/nme.1096.

O. Iliev and S. Tiwari. A generalized (meshfree) finite difference discretization for elliptic interface problems. In *Numerical Methods and Applications*, volume 2542 of *Lecture Notes in Computer Science*, pages 488–497, 2003. ISBN 3-540-00608-7.

A. Iske. *Multiresolution Methods in Scattered Data Modelling*. Springer-Verlag Berlin Heidelberg, 2004.

D. A. Kopriva. *Implementing Spectral Methods for Partial Differential Equations: Algorithms for Scientists and Engineers: Algorithms for Physicists, Mathematicians and Engineers*. Springer, 2009.

J. H. L. Kway, Y. S. Loh, and E. S. Chan. Laboratory study of deep-water breaking waves. *Ocean Engineering*, 25(8):657–676, AUG 1998. ISSN 0029-8018. doi: 10.1016/S0029-8018(97)00039-5.

Randall J. Leveque. *Finite Volume Methods for Hyperbolic Problems*. Cambridge University Press, 2002.

Vladimir D. Liseikin. *Grid Generation Methods*. Springer-Verlag Berlin Heidelberg, 1999.

T Liszka and J Orkisz. The Finite-Difference Method at Arbitrary Irregular Grids and its Application IN Applied Mechanics. *Computers & Structures*, 11(1-2):83–95, 1980. ISSN 0045-7949. doi: 10.1016/0045-7949(80)90149-2.

C. Lugni, M. Brocchini, and O. M. Faltinsen. Wave impact loads: the role of the flip-through. *Physics of Fluids*, 18(12), December 2006. ISSN 1070-6631. doi: 10.1063/1.2399077.

PA Madsen, HB Bingham, and H Liu. A new Boussinesq method for fully nonlinear waves from shallow to deep water. *Journal of Fluid Mechanics*, 462:1–30, JUL 10 2002.

JC Martin and WJ Moyce. An experimental study of the collapse of liquid columns on a rigid horizontal plane. *Philos. Trans. Roy. Soc. London*, 244:312–324, 1952.

J. J. Monaghan. Simulating Free-Surface Flows with SPH. *Journal of Computational Physics*, 110(2):399–406, February 1994. ISSN 0021-9991. doi: 10.1006/jcph.1994.1034.

K. B. Nielsen and S. Mayer. Numerical prediction of green water incidents. *Ocean ENgineering*, 31(3-4):363–399, Feb-Mar 2004.

D. H. Peregrine. Water-wave impact on walls. *Annual Review of Fluid Mechanics*, 35: 23–43, 2003.

A. von Ritter. Die fortpflanzung der wasserwellen. *VDI Zeitschrift*, 36:947–54, 1892.

C. Shu, H. Ding, H. Q. Chen, and T. G. Wang. An upwind local RBF-DQ method for simulation of inviscid compressible flows. *Computer Methods in Applied Mechanics and Engineering*, 194(18-20):2001–2017, 2004.

C.W. Shu and S. Osher. Efficient Implementation of Essentially Non-oscillatory Shock-Capturing Schemes. *Journal of Computational Physics*, 77(2):439–471, August 1988. ISSN 0021-9991. doi: 10.1016/0021-9991(88)90177-5.

J. E. Sprittles and Y. D. Shikhmurzaev. Viscous flow in domains with corners: Numerical artifacts, their origin and removal. *Computer Methods in Applied Mechanics and Engineering*, 200(9-12):1087–1099, 2011. ISSN 0045-7825. doi: 10.1016/j.cma.2010.12.005.

B. Mutlu Sumer and Jørgen Fredsøe. *Hydrodynamics around cylindrical structures*. World Scientific Publishing Co. Pte. Ltd., 1997.

M. Sussman, P. Smereka, and S. Osher. A Level set Approach for Computing Solutions to Incompressible 2-phase Flow. *Journal of Computational Physics*, 114(1):146–159, September 1994. ISSN 0021-9991. doi: 10.1006/jcph.1994.1155.

Gabriel Taubin. A Signal Processing Approach to Fair Surface Design. In *Proceedings of the 22nd annual conference on Computer graphics and interactive techniques*, SIGGRAPH '95, pages 351–358, New York, NY, USA, 1995. ACM.

F. C. K. Ting and J. T. Kirby. Dynamics of surf-zone turbulence in a spilling breaker. *Coastal Engineering*, 27(3-4):131–160, JUL 1996. ISSN 0378-3839. doi: 10.1016/0378-3839(95)00037-2.

Sudarshan Tiwari and Joerg Kuhnert. Modeling of two-phase flows with surface tension by finite pointset method (FPM). *Journal of Computational and Applied Mathematics*, 203(2):376–386, June 15 2007.

E. F. Toro. *Riemann Solvers and Numerical Methods for Fluid Dynamics, A Practical Introduction*. Springer, 2 edition, 1999.

JP Vila. On particle weighted methods and smooth particle hydrodynamics. *Mathematical Models & Methods In Applied Sciences*, 9(2):161–209, MAR 1999. ISSN 0218-2025.

Holger Wendland. *Scattered Data Approximation*. Cambridge University Press, 2005.

Z. Q. Zhou, J. O. D. Kat, and B. Buchner. A nonlinear 3D approach to simulate green water dynamics on deck. *Seventh international conference on numerical ship hydrodynamics*, pages 1–4, 1999.

O. C. Zienkiewicz, R. L. Taylor, and J. Z. Zhu. *The Finite Element Method, Its Basis and Fundamentals*. Elsevier Butterworth-Heinemann, 6 edition, 2005.

P. J. Zwart, G. D. Raithby, and M. J. Raw. The integrated space-time finite volume method and its application to moving boundary problems. *Journal of Computational Physics*, 154(2):497–519, September 20 1999.